A study of four nonlinear systems with parametric forcing

A Thesis
Submitted for the Degree of
Doctor of Philosophy
in the Faculty of Engineering

By
Amol Marathe

Department of Mechanical Engineering
Indian Institute of Science
Bangalore - 560 012
India

August 2007

Dedicated to

my parents

Abstract

This thesis considers four nonlinear systems with parametric forcing.

The first problem involves an inverted pendulum with asymmetric elastic restraints subjected to harmonic vertical base excitation. On linearizing trigonometric terms the pendulum is governed by an asymmetric Mathieu equation. Solutions to this equation are scaleable. The stability regions in the parameter plane are studied numerically. Periodic solutions at the boundaries of stable regions in the parameter plane are found numerically and then their existence is proved theoretically.

The second problem involves use of the method of multiple scales to elucidate the dynamics associated with early and delayed ejection of ions from Paul traps. A slow flow equation is developed to approximate the solution of a weakly nonlinear Mathieu equation to describe ion dynamics in the neighborhood of the nominal stability boundary of ideal traps. Since the solution to the unperturbed equation involves linearly growing terms, some care in identification and elimination of secular terms is needed. Due to analytical difficulties, harmonic balance approximations are used within the formal implementation of the method.

The third problem involves the attenuation, caused by weak damping, of harmonic waves through a discrete, periodic structure with wave frequency nominally within the Propagation Zone. Adapting the transfer matrix method and using the harmonic balance for nonlinear terms, a four-dimensional map governing the dynamics is obtained. This map is analyzed by applying the method of multiple scales upto first order. The resulting slow evolution equations give the amplitude decay rate in the stucture.

The fourth problem involves the dynamic response of a strongly nonlinear single-degree-of-freedom oscillator under a constant amplitude, parametric, periodic, impulsive forcing, e.g., a pendulum with strongly nonlinear torsional spring that is periodically struck in the axial direction. Single-term harmonic balance gives an approximate, but explicit, 2-dimensional map governing the dynamics. The map exhibits many fixed points (both stable and unstable), higher period orbits, transverse intersections of stable and unstable manifolds of unstable fixed points, and chaos.

Acknowledgements

I thank my advisor Dr. Anindya Chatterjee who guided me throughout this work. His motivation, patience, direct involvement in the research topic and, above all, friendly nature helped me to complete this work. His sound expertise in the technical domain helped me at crucial points throughtout this work. I respect the freedom he gave to me in the research work to reach a higher maturity level. Apart from depth in technical matters, his atypical and unorthodox thinking style, special linguistic skills and clarity in expressing himself will have a long-lasting influence on me. His valuable suggestions regarding different aspects of life will be helpful throughout my life.

I am very much indebted to Prof. Menon and my collaborator, Dr. Rajanbabu in one of the works. Dr. Rajanbabu will remain a source of inspiration for me for the rest of my life. I would like to mention special thanks to Supercomputer Education and Research Centre for the computing facility.

I am ever indebted to my family without whose cooperation and sacrifices pursuing a Ph.D. programme would have been impossible.

Next I would like to thank members of the Dynamics Lab. Healthy discussions both technical as well as non-technical held during an innumerable visits to Tea Board have resulted in conceptual clarity, development of new ideas and fun as well. I thank all my lab members, Satwinder, Nandakumar, Pankaj, Pradipta, Sandip, Pradeep, Vamshi, Umesh,

Arjun and Navendu. I also thank Venkatesh, Rahul and Dhananjay for their help in the lab.

Apart from lab members, I enjoyed the company of Prashant, Pranav Patil, Pranav Joshi, Venkatesh, Vinay, Vinayak, Yogesh, Atul, Sameer, Pravin, Abhijeet Yadav, Abhijeet Sarkar and Ashok Pandey. Many among these gave me access to their own computational facility for the intense work involved in the research work. I thank them all.

Contents

List of Figures

List of Tables

Chapter 1

Introduction

This thesis is in the area of vibrations. A vibrating system can be either forced or unforced. Forced systems occur in many applications in engineering and physics. Forcing can be either external or parametric. A spring-mass system can be given a continuous sinusoidal forcing. This is an example of an externally forced system. The parameters of the system are the stiffness of the spring and the mass. If we consider a spring whose stiffness varies periodically with time, then the system is said to be *parametrically forced*. Such systems occur quite naturally in our day-to-day life, for example, a child playing on a swing changes the position of her legs to pump energy into the system and increases the amplitude of the swing. Other important examples are a gear-pair system with time-periodic stiffness and a vertically driven pendulum.

We study four systems in this thesis. All are nonlinear. The forcing considered is periodic. The systems are essentially simple and are modelled as 1-degree-of-freedom systems. Out of four systems, two are continuous and two are discrete. Both strong and weak nonlinearities are considered. An impulsive forcing is considered in one of the systems. Periodicity in the parameters is with respect to time as well as space, i.e., the independent variable is spatial in one of the systems. Damping is considered in one of the systems.

A famous example of a parametrically forced system is an inverted pendulum with the base excited harmonically. It is governed by the famous Mathieu equation. It is a linear ordinary differential equation with periodic coefficients and has been a subject of study for a hundred years [1, 2, 3, 4, 5]. Our first system is a strongly nonlinear version of this Mathieu equation. It governs the motion of an inverted pendulum with unequal elastic restraints. We call it an asymmetric Mathieu equation. The equation is strongly nonlinear. For small motions linearization is not possible. However its solutions are scaleable. Scaleability of solutions helps us to study their asymptotic stability. We numerically study the stability regions in the parameter plane. We find numerically and prove theoretically the existence of periodic solutions at stability boundaries. A more general type of this equation is also studied for stability regions in the parameter space. The results of this study have been published in [6].

The Mathieu equation also describes the motion of ions in an ideal Paul trap. The Paul trap mass spectrometer is an analytical instrument which carries out fragment analysis of unknown chemical compounds to elucidate their composition and structure [7]. The second problem of this thesis is in this area, and considers mass selective boundary ejection of ions from practical Paul traps. Boundary ejection of ions can be modelled by a weakly nonlinear version of Mathieu equation with parameter values corresponding to the stability boundary of the so called Mathieu stability plot. Method of multiple scales is used to develop a slow flow equation to approximate the solution. Because we look at the boundary ejection, the solution to the unperturbed equation involves linearly growing terms. Therefore some care in identification and elimination of secular terms is required. Also a heuristic method of harmonic balance is used due to analytical difficulties within the formal implementation of the method. This study was conducted in collaboration with Dr. Rajanbabu [7], and the results of this study have been published in [8].

Axial vibrations in a rod are often modelled using the 1-D wave equation,

$$\rho \partial_{tt} u = \partial_x (E \partial_x u),$$

where ρ is mass per unit length, E is Young's modulus, u is displacement at (x, t) and ∂_s denotes partial derivative with respect to s. E and ρ may vary with the spatial variable x. Here we look at the special case where E is constant, but ρ varies with x. Assuming a harmonic solution $u(x,t) = \sin(\omega\, t)\, U(x)$, we have

$$U'' + \frac{\rho \omega^2}{E} U = 0.$$

Now there is no time in the equation, but the correspondence with the previous equation is clear: x is now the independent (time-like) variable. Considering harmonic wave propagation at various frequencies, i.e., as parameter ω is varied, the system is parametrically forced. In particular, if we put $\rho = m\sum_{k=-\infty}^{\infty}\delta(x-k)$, where δ is a Dirac function, the system describes a discrete periodic structure infinitely extended in both positive and negative x-directions. With this motivation, our third system is a discrete, periodic structure with one period consisting a mass, spring and a damper. Powerful matrix-based approaches commonly used for studying linear periodic structures are not useful in studying nonlinear structures. The concept of attenuation constant that gives generally amplitude decay rate can be extended to weakly nonlinear conservative [9] as well as non-conservative structures. We consider attenuation of harmonic waves in non-conservative structures with frequency nominally within the Propagation Zone. Stiffness considered is linear. Both linear and weakly nonlinear damping are considered. A four dimensional map governing the dynamics is obtained using harmonic balance for the nonlinear terms. This map is then analysed by applying the method of multiple scales upto the first order. The resulting slow evolution equations give the amplitude decay rate in the structure. The results of this study have been published in [10].

Finally, we consider a nonlinear, parametrically forced oscillator governed by

$$\ddot{x} + x^3 = xF(t).$$

We consider a special form of the forcing

$$F(t) = P\sum_{n=1}^{\infty}\delta(t-nT)$$

with constant amplitude P. A pendulum with a strongly nonlinear torsion spring struck periodically in the axial direction is governed by the above equation. Assuming a 1-term harmonic balance approximation for the solution, an explicit 2-dimensional map is obtained. The map is studied for fixed points and their stability. Stable and unstable manifolds of different period-orbits of the unstable type are computed with the help of a free downloadable software. Transverse intersections of the stable and unstable manifolds confirm the presence of chaos in the system.

Finally some concluding discussion is presented at the end of the thesis.

Chapter 2

Asymmetric Mathieu equations

In this chapter, we study an inverted pendulum with asymmetric elastic restraints. This system is parametrically forced and strongly nonlinear. We establish, numerically as well as theoretically that there exist periodic solutions at the boundaries of stable regions in the parameter plane. Our theoretical results apply to more general asymmetric Mathieu and Hill's equations. The material of this chapter has been published in [6].

2.1 Introduction

Consider an inverted pendulum with asymmetric elastic restraints in which the pivot is given a vertical periodic oscillation, as shown schematically in Fig. 2.1. Spring stiffnesses on the left and right are taken as $\delta(1-\bar{a})$ and $\delta(1+\bar{a})$, respectively, with $0 \leq \bar{a} < 1$. The springs are horizontal and, when engaged, their endpoint compressions equal the horizontal displacement of the mass; they may alternatively be thought of as torsion springs at the pivot point. Gravity may be incorporated in the spring stiffnesses and is not explicitly accounted for. There is no damping.

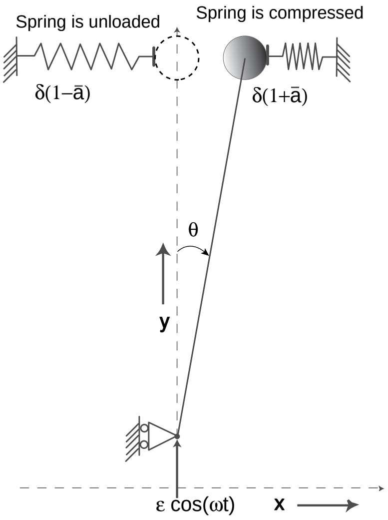

Figure 2.1: An asymmetrically supported inverted pendulum with base excitation.

Let the angular displacement of the pendulum be $\theta(t)$. Taking the length of the pendulum to be l and the origin of the co-ordinate system at some point on $\theta = 0$ line, the co-ordinates of the centre of mass of the pendulum are

$$x = l \sin\theta, \quad y = u(t) + l\cos\theta,$$

where $u(t)$ is the imposed displacement of the pivot. Differentiating,

$$\dot{x} = l\cos\theta\,\dot{\theta}, \quad \dot{y} = \dot{u} - l\sin\theta\,\dot{\theta}.$$

The system kinetic energy is

$$T = \frac{1}{2}\,m\left(\dot{x}^2 + \dot{y}^2\right),$$

where m is the mass. We take the potential energy to be of the form (recall that gravity is not explicitly included)

$$V = \frac{1}{2}\,\delta\,(1 + \operatorname{sgn}(\theta)\,\bar{a})l^2\theta^2,$$

which is correct for torsion springs (with suitable spring constants), and uses $\sin\theta \approx \theta$ for horizontal straight springs.

The equation of motion can now be routinely obtained using Lagrange's method. On linearizing trigonometric terms by sustituting $\cos\theta = 1$ and $\sin\theta = \theta$, and letting $l = 1$,

$m = 1$, we obtain

$$\ddot{\theta} - \ddot{u}\,\theta + \delta\,\left(1 + \mathrm{sgn}(\theta)\bar{a}\right)\theta = 0.$$

Assuming $u = \epsilon\cos(t)$, writing x in place of θ, and noting that

$$\mathrm{sgn}(x)\,x = |x|,$$

we obtain

$$\ddot{x} + (\delta + \epsilon\cos(t))x + \delta\bar{a}|x| = 0. \tag{2.1}$$

We call Eq. (2.1) an asymmetric Mathieu equation; setting $\bar{a} = 0$ gives the usual Mathieu equation [4, 5, 11]. We mention in passing that the dynamics of a gear-pair system involving backlash can be modeled by a similar equation [12]. In this paper we investigate some of the similarities and differences between the stability diagrams (in the δ-ϵ parameter plane) for the usual and asymmetric Mathieu equations. Our theoretical treatment allows parametric forcing of the $|x|$ term as well, which introduces two more free parameters as dicussed later.

As is well known, the usual Mathieu equation has alternating stable and unstable regions in the parameter plane. On the transition curves (boundaries of the stability regions), there are periodic solutions with period either 2π or 4π (2:1 subharmonic motion) [4, 5, 11]. How are these related to the stability regions, transition curves, and periodic solutions of the asymmetric Mathieu equation?

Equation (2.1) is a homogeneous second-order differential equation with real periodic coefficients. It is also essentially nonlinear: linearization near $x = 0$ is not possible. If $x_1(t)$ and $x_2(t)$ are two solutions, then $\alpha x_1(t) + \beta x_2(t)$ is not a solution in general. However solutions are *scaleable*, i.e., if $x(t)$ is a solution then $\alpha x(t)$ is also a solution for any real $\alpha > 0$. This scaleability will be important in the subsequent analysis.

2.2 Unforced system

The unforced system ($\epsilon = 0$) is

$$\ddot{x} + \delta x + \delta\bar{a}|x| = 0, \tag{2.2}$$

The asymmetric potential energy of this unforced system and the corresponding asymmetric spring force are shown in Fig. 2.2, left and right, respectively.

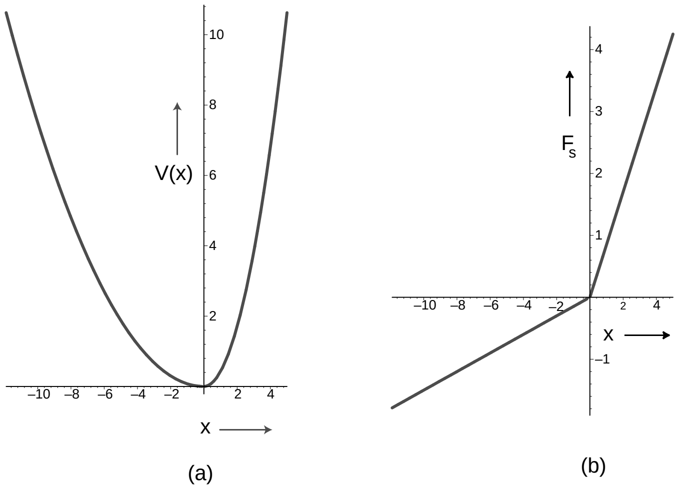

(a) (b)

Figure 2.2: $\delta = 0.5, \bar{a} = 0.7$. (a): potential energy. (b): restoring spring force.

All solutions of the unforced system are periodic, and have the same period. Each such periodic solution consists of two half-sinusoids, one for $x > 0$ and one for $x < 0$, with different amplitudes and time durations. The time period T and corresponding fundamental frequency ω are

$$T = \frac{\pi}{\sqrt{\delta(1+\bar{a})}} + \frac{\pi}{\sqrt{\delta(1-\bar{a})}} \text{ and } \omega = \frac{2\pi}{T}. \tag{2.3}$$

2.3 A Lyapunov-like exponent for scaleable systems

Since the fully nonlinear forced system seems analytically intractable, we resort to numerics. A few numerically obtained solutions for Eq. (2.1) are shown in Fig. 2.3. It is seen that solutions grow without bound (unstably) for some parameter values, but remain bounded for others. The unstable solutions grow exponentially, and we begin by characterizing their exponential growth rate.

A Lyapunov-like exponent is defined as

$$\sigma(\delta, \epsilon) = \lim_{N\to\infty} \frac{1}{N} \sum_{k=0}^{N} \ln(||X_k^{2\pi}||), \tag{2.4}$$

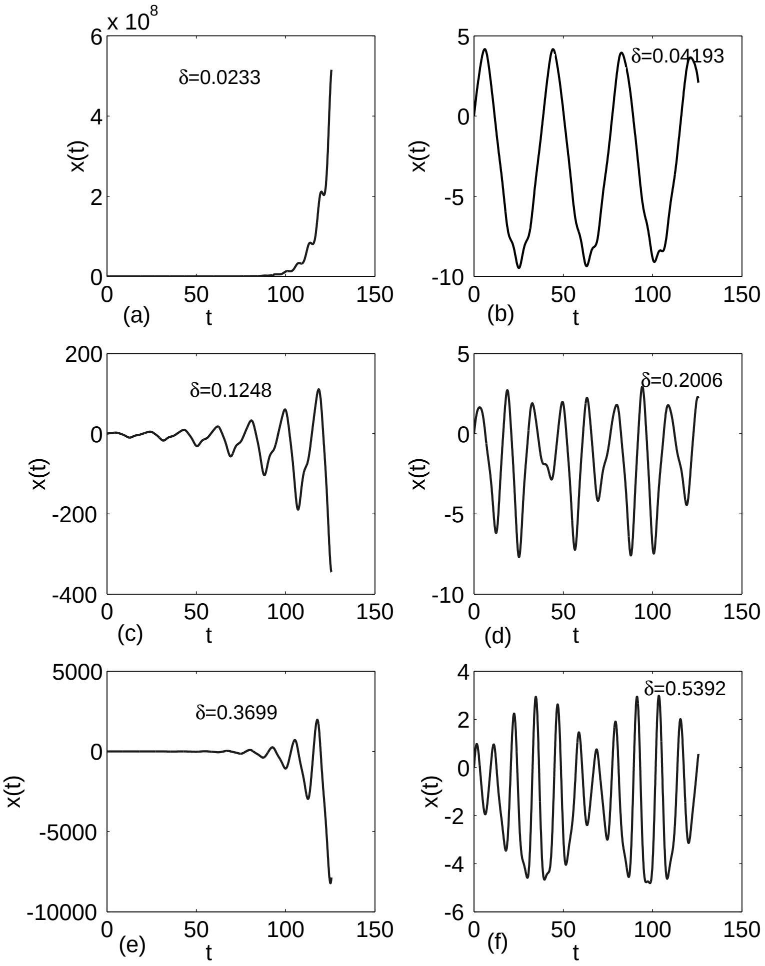

Figure 2.3: Time histories of solutions for $\epsilon = 0.2$ fixed and δ values as indicated. Cases a, c, e are unstable and b, d, f are stable.

where the state vector $X = \{x, \dot{x}\}^T$; $||.||$ denotes the Euclidean norm; the subscript k in $X_k^{2\pi}$ denotes the time in number of forcing periods; and a superscript, either 0 or 2π, denotes the start or end of a forcing period, respectively.

The above Lyapunov-like exponent is calculated as follows. We numerically integrate Eq. (2.1) over an interval of 2π with random intial conditions X_0^0 that satisfy $||X_0^0|| = 1$. At the end of this integration, we have the state $X_0^{2\pi}$. Initial conditions for the next cycle are then obtained by rescaling to unit norm:

$$X_1^0 = \frac{X_0^{2\pi}}{||X_0^{2\pi}||}.$$

Integration over another period of forcing then gives $X_1^{2\pi}$. The above steps are repeated N times, for some large N. We discard the first several states in the calculation to get rid of transients, and take the first retained state as X_0^0. N is taken large enough to obtain convergence, which in this case is relatively rapid presumably because solutions are not chaotic.

An exponent $\sigma = 0$ implies the corresponding δ-ϵ point is stable, while $\sigma > 0$ implies it is unstable. In numerics, $\sigma = 0$ is not exactly observed, and a nonzero numerical tolerance or threshold is set by the analyst.

2.4 Numerical stability diagram

We first present the results of a numerical stability analysis of the asymmetric Mathieu equation on the δ-ϵ parameter plane for the arbitrarily chosen value of $\bar{a} = 0.7$ (we will show some more results for $\bar{a} = 0.8$ later in this same section). In these calculations, numerical integration of ODEs was done using Matlab's built-in ODE solver "ODE45" with "event detection" so as to ensure that every zero-crossing of x coincides with a mesh point (or sampling instant) in the time-discretized solution.

Figure 2.4 shows the Lyapunov-like exponent on a 500 × 500 grid covering $\delta \in [-0.1, 1.3]$ and $\epsilon \in [0, 1]$, for $N = 600$. The calculation took several days, distributed among a few PCs. Figure 2.5 shows a closer and refined view of the boxed, bottom left, region of Fig. 2.4. Now $\delta \in [0, 0.45]$ and $\epsilon \in [0, 0.4]$, the grid is 450 × 400, and $N = 2400$.

The figures show several instability regions. Limitations in numerics and graphics limit the number of visible regions; however, it seems that there are infinitely many such regions, successively narrower and more weakly unstable, nested between a few large and strongly unstable regions. These large and strongly unstable regions have a one to one correspondence with regions of instability for the usual Mathieu equation, as may be seen from the following. Narrower and finer resonance regions are associated with smaller nu-

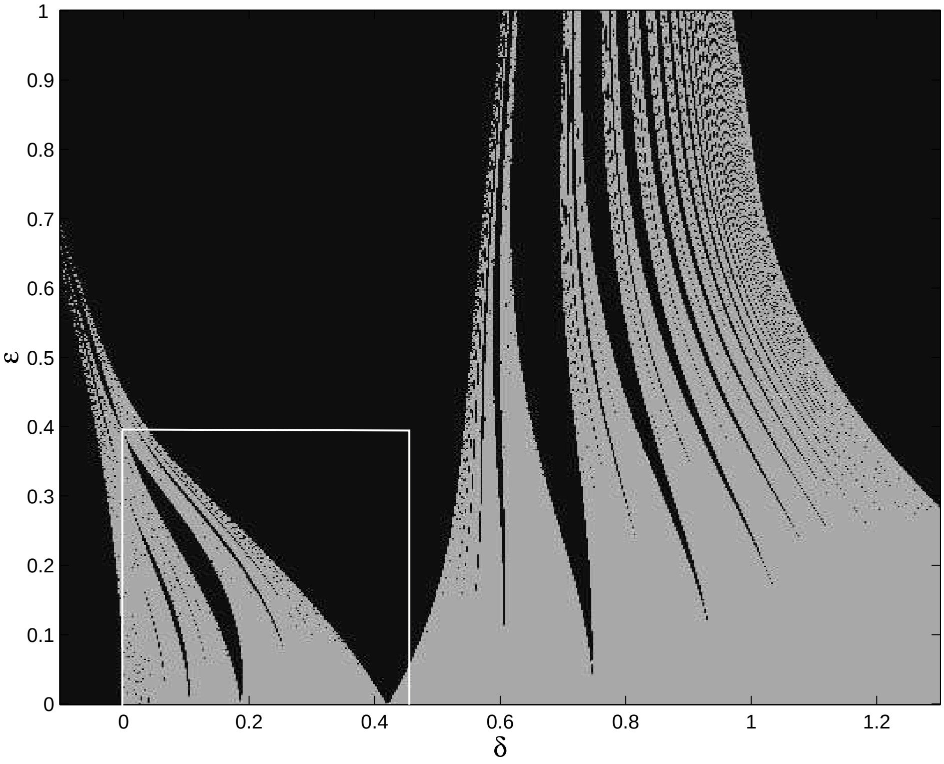

Figure 2.4: Stability diagram for $\bar{a} = 0.7$, $N = 600$. Gray=stable, black=unstable.

merical values of Lyapunov-like exponents: decreasing N or increasing the numerical value of the cutoff tolerance in the stability diagram will prevent us from detecting these regions.

For the usual or symmetric Mathieu equation ($\bar{a} = 0$), there are regions of instability emanating from the δ axis at $\delta_{sym} = 0, 0.25, 1, \cdots$. These correspond to simple rational relationships between the unforced time period, $2\pi/\sqrt{\delta_{sym}}$, and the forcing period, 2π.

For the asymmetric Mathieu equation with $\bar{a} = 0.7$ the time period of the unforced system is, from Eq. (2.3),

$$1.2964 \times \frac{2\pi}{\sqrt{\delta_{asym}}}.$$

For the same rational relationships to hold so that the same resonances may occur, we require this time period to bear the same ratio to 2π as in the symmetric case.

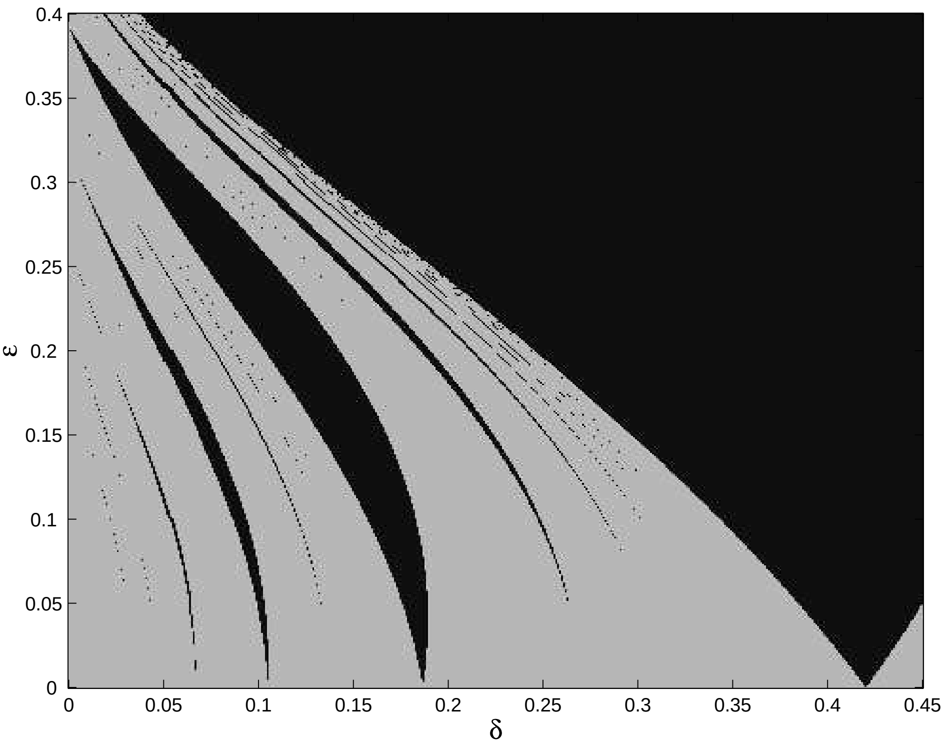

Figure 2.5: Zoomed portion of Fig. 2.4; $\bar{a} = 0.7$, $N = 2400$. Gray=stable, black=unstable.

This gives

$$1.2964 \times \frac{2\pi}{\sqrt{\delta_{asym}}} = \frac{2\pi}{\sqrt{\delta_{sym}}},$$

or

$$\delta_{asym} = 1.2964^2\, \delta_{sym} = 1.6805\, \delta_{sym}.$$

Thus, we expect corresponding instability regions for the $\bar{a} = 0.7$ case to emanate from the δ axis at $\delta = 0, 0.4201, 1.6805, \cdots$. This is supported by the numerical results.

The asymmetric and symmetric Mathieu equations are identical on the ϵ-axis (with $\delta = 0$),

$$\ddot{x} + \epsilon\cos(t)x = 0.$$

Therefore stability intervals on the ϵ-axis for both equations (for any $\bar{a}$) are the same. So all the new instability regions of the asymmetric equation must have zero widths on the ϵ-axis. This is observed in the numerics. Similarly, the widths of the corresponding strong instability regions that occur for both the asymmetric as well as symmetric equations coincide on the ϵ-axis; this is outside the region covered by the numerical results, and cannot be seen in the figure.

We now consider other possible resonances. Let r be a simple rational number, such as (say) 2.5, 3 or 4. Consider a situation where the ratio between the unforced time period and the forcing period is r, i.e.,

$$1.2964 \times \frac{2\pi}{\sqrt{\delta}} = 2\pi r, \tag{2.5}$$

or

$$\delta = \frac{1.2964^2}{r^2} = \frac{1.6805}{r^2}.$$

The δ values corresponding to $r = 2.5$, 3 and 4 are then 0.2689, 0.1867 and 0.1050 respectively. There are, in fact, instability regions corresponding to these values on the δ axis, as may be seen with a little faith from Fig. 2.5, or more convincingly from Fig. 2.7 in the next section.

The qualitative results obtained above are not special for $\bar{a} = 0.7$. Figure 2.6 shows the Lyapunov-like exponent for $\bar{a} = 0.8$ on a 500×500 grid covering $\delta \in [-0.1, 1.5]$ and $\epsilon \in [0, 1]$, for $N = 600$. There is agreement with the results for $\bar{a} = 0.7$.

From the numerical results of this section, it seems likely that all the narrow instability regions seen in Fig. 2.5 do in fact continue all the way to the δ axis. This is verified numerically in the next section, and supported further with theory later in the paper.

2.5 Periodic solutions on stability boundaries

As is well known, for the usual or symmetric Mathieu equation, there are periodic solutions of period either 2π or 4π on each stability boundary on the parameter plane. Are there periodic solutions (of possibly other periods) for each stability boundary for the asymmetric Mathieu equation? In this section, we investigate this question numerically. In particular, we seek curves on the δ-ϵ parameter plane where periodic solutions exist; and anticipate that these curves will start from the δ axis at the points from which instability regions emanate (as discussed above).

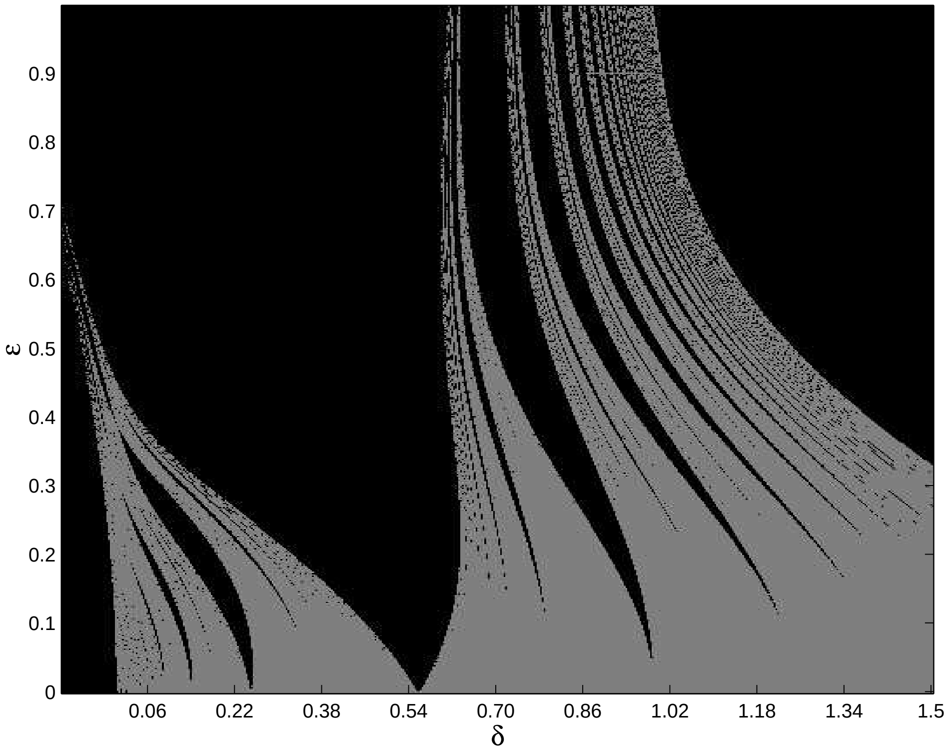

Figure 2.6: Stability diagram for $\bar{a} = 0.8$, $N = 600$. Gray=stable, black=unstable.

We present here results obtained for $\delta = 0.4201$, 0.2689, 0.1867 and 0.1050. The corresponding time periods expected, and obtained, are 4π, 10π, 6π and 8π, respectively (note: 10π corresponds to $r = 2.5$ and not 5 in Eq. (2.5)). From each of these points on the δ axis, two curves are found to emanate. These curves were obtained using a numerical arc-length based continuation method which is described in the Appendix A. Results, shown using white lines on the stability diagram, are given in Fig. 2.7. The picture, presented here for $\epsilon \geq 0$, is symmetric about the δ axis.

It is clear that, at least for the instability regions considered, stability boundaries correspond to the existence of periodic solutions, even for the unstable regions that are absent for the symmetric Mathieu equation. It seems likely that there are also periodic solutions at all other stability boundaries. In section 7, we show theoretically that this is in fact the case.

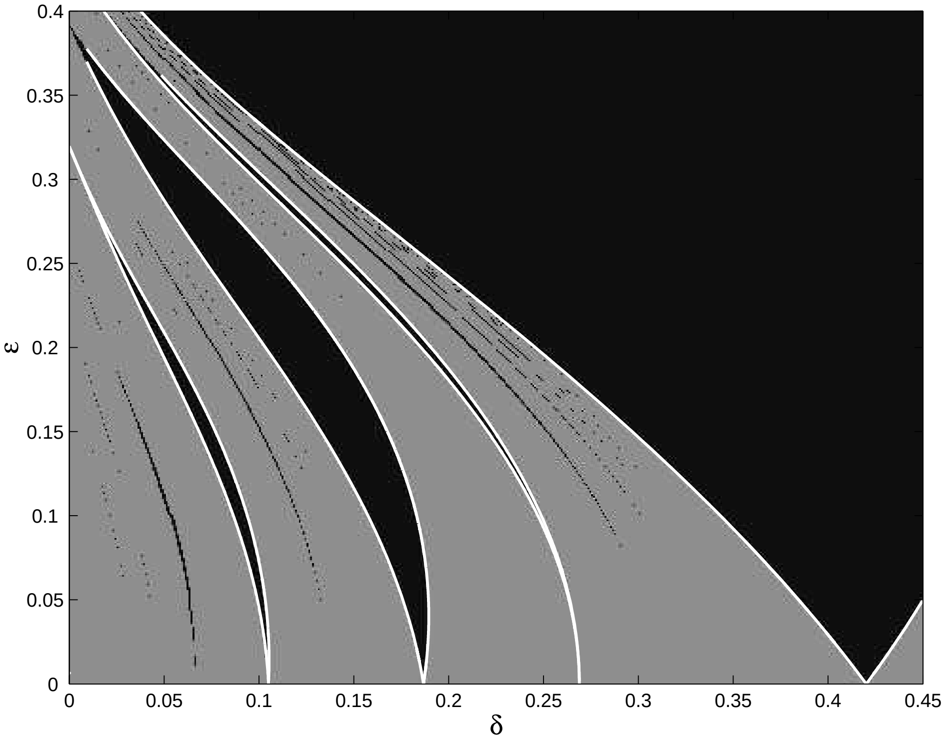

Figure 2.7: 4π, 6π, 8π and 10π period solutions on the stability boundaries in the δ-ϵ parameter plane for the asymmetric Mathieu equation with $\bar{a} = 0.7$.

A few points regarding the numerical search for periodic solutions are now presented.

Since solutions are scaleable, we may assume that the initial conditions at $t = 0$ satisfy either $x_0 = \pm 1$, or $\dot{x}_0 = \pm 1$, or even $x_0^2 + \dot{x}_0^2 = 1$. It turns out that for the periodic solutions plotted here (Fig. 2.7), the solution branch to the left of each instability region has $\dot{x}_0 = 0$ and $x_0 = 1$; while for the solution branch on the right side of each region, $x_0 = 0$ and $\dot{x}_0 = 1$. The numerical strategy, however, assumes one of these (x_0 or $\dot{x}_0$) to be nonzero (equal to ± 1), and lets the numerical routine discover that the other is zero (if in fact it is).

Numerically, we proceed as follows. Starting at $t = 0$ with some values of δ and ϵ (along with, say, $\bar{a} = 0.7$ fixed and $x_0 = 1$), we numerically integrate forward in time to time T (for suitable T, which is an even multiple of π that we know in advance as indicated above), and check that the final state is identical to the initial state. We then iteratively look for a nearby point on the δ-ϵ plane where these conditions are satisfied again. This well known procedure, called arc-length based continuation, is described for completeness in the appendix.

Note that these periodic solution branches can (at least potentially) be computed in a small fraction of the time needed to generate, say, Fig. 2.5. Thus, as for the symmetric Mathieu equation, finding periodic solutions is an efficient way of computing the stability transition curves for the asymmetric Mathieu equation.

2.6 Theoretical considerations

The asymmetric Mathieu Eq. (2.1) can be rewritten as

$$\dot{\mathbf{x}} = \mathbf{f}(\mathbf{x}, \mathbf{t}) \tag{2.6}$$

with

$$\mathbf{x} = \left\{ \begin{array}{c} x \\ \\ y \end{array} \right\}$$

and

$$\mathbf{f} = \left\{ \begin{array}{c} y \\ \\ -(\delta + \epsilon\,\cos(t))\,x - \delta\,\bar{a}\,|x| \end{array} \right\}$$

Formally, we observe that Eq. (2.6) is divergence free, i.e., $\nabla.\mathbf{f} = \mathbf{0}$. This means areas are preserved in the $(x, \dot{x})$ plane.

Let $x = R\cos(\phi)$ and $y = R\sin(\phi)$. Consider a Poincaré map that takes $\mathbf{x}$ from the start of a forcing period to the start of the next (i.e., through $t = 2\pi$). Let (R_0, ϕ_0) be an initial point. The Poincaré map sends $(R_0, \phi_0) \longmapsto (R_1, \phi_1)$ with

$$R_1 = \bar{f}(R_0, \phi_0),$$

$$\phi_1 = \bar{g}(R_0, \phi_0),$$

for some as yet unknown continuous functions $\bar{f}$ and $\bar{g}$. Since solutions to Eq. (2.1) are scaleable, we can write

$$\bar{f}(R_0, \phi_0) = R_0 \bar{f}(1, \phi_0) = R_0 f(\phi_0).$$

Similarly, scaleability requires

$$\bar{g}(R_0, \phi_0) = g(\phi_0).$$

Thus, the point (R_0, ϕ_0) gets mapped to $(R_0 f(\phi_0), g(\phi_0))$.

The system is reversible in time. Zero initial conditions lead to zero solutions for all time. These two together imply that nonzero solutions do not become zero within finite time. In turn, this means

$$f(\phi_0) \neq 0.$$

We may, without loss of generality, assume $f > 0$.

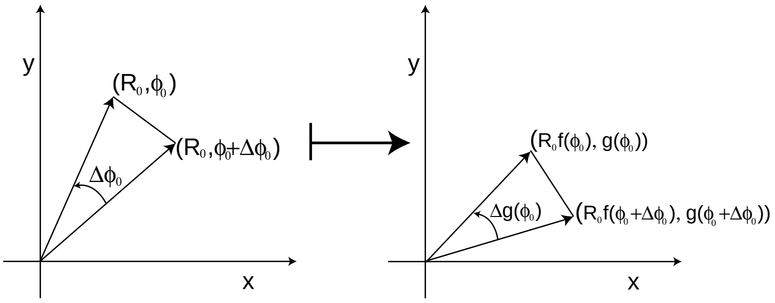

Figure 2.8: Area preservation of the flow.

Consider two nearby initial conditions (R_0, ϕ_0) and $(R_0, \phi_0 + \Delta\phi_0)$, as sketched in Fig. 2.8. The Poincaré map sends these initial conditions to $(R_0 f(\phi_0), g(\phi_0))$ and $(R_0 f(\phi_0 + \Delta\phi_0), g(\phi_0 + \Delta\phi_0))$, as sketched in Fig. 2.8.

If we think of the entire triangle as composed of initial conditions, then the triangle gets mapped to a triangle because solutions are scaleable (the edges remain straight lines).

Since f and g are continuous, we write

$$f(\phi_0 + \Delta\phi_0) = f(\phi_0) + \Delta f, \text{ and } g(\phi_0 + \Delta\phi_0) = g(\phi_0) + \Delta g,$$

where the Δ symbol is now taken to denote “small.”

Area preservation now gives,

$$\frac{|\Delta g(\phi_0)|}{\Delta\phi_0} = \frac{1}{f(\phi_0)^2},$$

where we have ignored small quantities of second order.

We now come to an important point. No matter what finite values we assign to the parameters δ and ϵ, the functions f and g depend continuously on them as well as on ϕ_0. So, if we now change any combination of δ, ϵ and/or ϕ_0 in any way that we like, $f(\phi_0)$ always remains finite and nonzero. This means $\Delta g(\phi_0)$ is always nonzero as well, because $\Delta\phi_0$ is nonzero and positive by choice; it *never* changes sign. It is possible to conclude from a consideration of the case $\delta = \epsilon = 0$ and $\phi_0 = \pi/2$, i.e.,

$$\ddot{x} = 0,$$

that $\Delta g > 0$. From here, by continuous changes in parameters and initial conditions, we can arrive at the point of interest to conclude that the absolute value sign may be removed, and so

$$\frac{\Delta g(\phi_0)}{\Delta\phi_0} = \frac{1}{f(\phi_0)^2},$$

which in the limit shows that g is differentiable and satisfies

$$g'(\phi_0) = \frac{1}{f^2(\phi_0)}. \tag{2.7}$$

It follows that $g'(\phi_0) > 0$ for all ϕ_0.

We observe from Eq. (2.7) that if any solution settles down to some stable point ϕ^*, then $g(\phi^*) = \phi^*$ and $g'(\phi^*) < 1$ (the condition for stability of fixed points of iterated scalar maps). This in turn implies that $f(\phi^*) > 1$. Thus any solution that settles exponentially to some ϕ^* must grow exponentially in magnitude.

What happens if, instead of a fixed point, g has a k-cycle, i.e., the k^{th} iterate of some ϕ^* equals itself, or $g^k(\phi^*) = \phi^*$? Let $g(\phi^*) = \phi_1$, $g(\phi_1) = \phi_2$, and so on. Then $\phi_k = \phi^*$ for a k-cycle.

If, in addition, the k-cycle is exponentially stable, i.e.,

$$g'(\phi^*) \cdot g'(\phi_1) \cdot g'(\phi_2) \cdots g'(\phi_{k-1}) < 1, \tag{2.8}$$

then it follows that

$$f(\phi^*) \cdot f(\phi_1) \cdot f(\phi_2) \cdots f(\phi_{k-1}) > 1,$$

and the solution grows exponentially in magnitude (the Lyapunov-like exponent is positive).

Consider, now, a gradual change in parameters that causes this unstable point in parameter space to approach a stability boundary. The k-cycle (corresponding to ϕ^*) depends on parameters, and changes gradually as well; it is structurally stable as long as inequality (2.8) holds. Thus, loss of stability can only occur when

$$g'(\phi^*) \cdot g'(\phi_1) \cdot g'(\phi_2) \cdots g'(\phi_{k-1}) = 1,$$

at which point we also have

$$f(\phi^*) \cdot f(\phi_1) \cdot f(\phi_2) \cdots f(\phi_{k-1}) = 1.$$

In other words, an unstable solution (i.e., a growing solution with a positive value of the Lyapunov-like exponent used in this paper; but also a solution where ϕ^* corresponds to a stable k-cycle of the iterated function g) can only lose instability (or gain stability; or reach a stability margin) by deforming continuously into a periodic solution as parameters are slowly changed so as to reach a point on a stability boundary.

Conclusion 1: A stable k-cycle in the iterated function g implies instability in the system solution. From the corresponding (unstable) point on the parameter plane, moving towards a stable point requires appearance of a periodic solution on the stability boundary.

What we wish to prove, however, is more general. We wish to prove that *every* stability boundary corresponds to the existence of a periodic solution. We will do this by showing that every unstable point in the parameter plane corresponds to the existence of a stable k-cycle in the iterated function g. Conclusion 1 above will then be applicable, and the desired result will be established.

Accordingly, we now assume that the solution is unstable, i.e., for some parameter values δ and ϵ, and referring to Eq. (2.4),

$$\sigma = \lim_{N\to\infty} \frac{1}{N} \sum_{k=0}^{N} \ln(||X_k^{2\pi}||) > 0. \tag{2.9}$$

This is equivalent to

$$E(\ln(f(g^n(\phi_0)))) > 0, \tag{2.10}$$

where E represents expected value, and n is sufficiently large that initial transients are not important and the final steady state behavior of the iterates of g, whether periodic or not, is obtained. From Eq. (2.7), we have

$$E(\ln(g')) = -2E(\ln(f)),$$

i.e.,

$$E(\ln(g'(g^n(\phi)))) = -2E(\ln(f(g^n(\phi)))).$$

Therefore

$$E(\ln(g'(g^n(\phi)))) < 0.$$

Let

$$E(\ln(g'(g^n(\phi)))) = -a, \tag{2.11}$$

for some strictly positive number a. Moreover, since we assume the system has reached steady state behavior, we can also define the variance of $\ln g'$ as

$$\operatorname{var}(\ln(g'(g^n(\phi)))) = b^2, \tag{2.12}$$

for some $b > 0$.

Let $\phi_p = g^p(\phi_0)$ for $p > 1$. Since ϕ is an angle, we can look at its values modulo 2π.

The dynamics of the system generates a sequence $\phi_0, \phi_1, \phi_2, \phi_3 \cdots$, which is now bounded (because we look at the values modulo 2π). Every bounded sequence has a convergent subsequence [13]. Let the subsequence be $\phi_{c_1}, \phi_{c_2}, \phi_{c_3}, \cdots$, where $c_i > c_j$ if $i > j$. Let the subsequence converge to ϕ^*. Then, for any given $\varepsilon > 0$, there exists a finite M such that for all $n > M$, $\phi_{c_n} - \phi^* < \varepsilon$. We choose two points from the subsequence, not necessarily consecutive, say $\phi_{c_{n_1}}, \phi_{c_{n_2}}$ with $n_2 > n_1 > M$.

Now consider the function

$$h(\phi) = g^{c_{n_2} - c_{n_1}}(\phi) - \phi. \tag{2.13}$$

Then, applying the chain rule of differentiation,

$$h'(\phi) = g'(g^{c_{n_2} - c_{n_1} - 1}(\phi))g'(g^{c_{n_2} - c_{n_1} - 2}(\phi)) \cdots g'(g(\phi))g'(\phi) - 1. \tag{2.14}$$

Considering $h'(\phi_m)$ for some $m > M$ in the subsequence $c_1, c_2, \cdots$, we have

$$h'(\phi_m) = g'(\phi_{c_{n_2}-c_{n_1}+m-1})g'(\phi_{c_{n_2}-c_{n_1}+m-2}) \cdots g'(\phi_{m+1})g'(\phi_m) - 1.$$

Considering the logarithm of the first term on the right hand side, we have (calling it, say, Z)

$$Z = \sum_{i=0}^{c_{n_2}-c_{n_1}-1} \ln g'(\phi_{m+i}).$$

For c_{n_2} sufficiently larger than c_{n_1} (and we are free to choose it so), the central limit theorem applies; in particular, the expected value of Z is $-(c_{n_2} - c_{n_1})a$ (see Eq. (2.11)), and its standard deviation is $b\sqrt{c_{n_2} - c_{n_1}}$ (see Eq. (2.12)), which is much smaller. Thus, Z is strictly negative, and can be as large as we wish to make it: its exponential is a positive number which can be as small as we like, independent of ε. It follows that

$$h'(\phi_m) = g'(\phi_{c_{n_2}-c_{n_1}+m-1})g'(\phi_{c_{n_2}-c_{n_1}+m-2}) \cdots g'(\phi_{m+1})g'(\phi_m) - 1$$

lies between -1 and 0. In particular, it can be bounded away from 0 by a nonzero amount, such as 1/2, independent of ε.

Now consider Eq. (2.13)

$$|h(\phi_m)| = \left|\phi_{m+c_{n_2}-c_{n_1}} - \phi_m\right| < 2\varepsilon.$$

Thus, $h(\phi_m)$ is small; and $h'(\phi_m)$ is nonzero. By the implicit function theorem, h has a zero close to ϕ_m, say at $\tilde{\phi}$. This zero corresponds to a stable k-cycle of the iterated function g.

Conclusion 2: An unstable solution of the system implies the existence of a stable k-cycle of the iterated function g.

By Conclusion 1 above, every point on a stability boundary in the parameter plane (or parameter space, if we introduce more parameters) corresponds to the existence of a periodic solution. However, unlike the usual or linear Mathieu (or Hill) equation, the period need not be solely 2π or 4π, but could be a higher multiple of 2π.

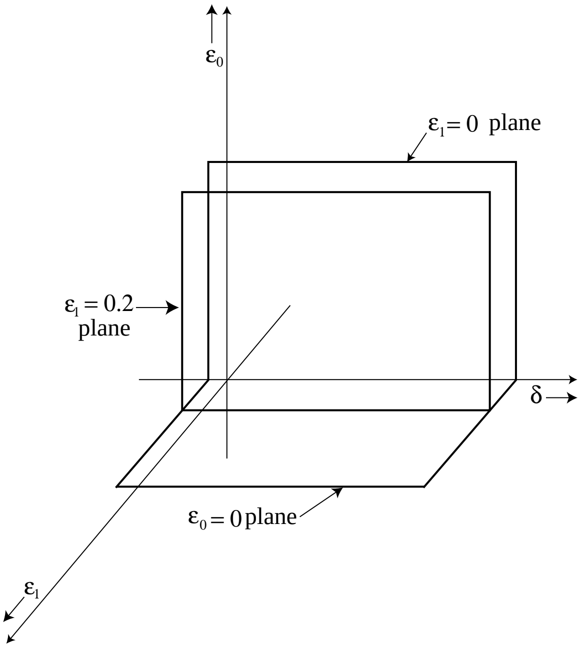

Figure 2.9: Parameter planes in the $(\delta, \epsilon_0, \epsilon_1)$ space where numerical stability results are presented.

2.7 General asymmetric Mathieu equations

More generally, our foregoing results apply to

$$\ddot{x} + (\delta + \epsilon_0 \cos(t))x + \bar{a}(\delta + \epsilon_1 \cos(t + \psi))|x| = 0, \tag{2.15}$$

where ϵ_1 and ψ are additional free parameters (compare with Eq. (2.1)).

The theoretical results presented above actually hold for the general asymmetric Hill's equation

$$\ddot{x} + p_1(t)x + p_2(t)|x| = 0, \tag{2.16}$$

with $p_1(t+T) = p_1(t)$ and $p_2(t+T) = p_2(t)$ $\forall\, t$ and for some $T > 0$ (T can be taken as 2π upon scaling time suitably). We are not presently aware of actual physical systems governed by such equations, except for the restricted case we began this paper with.

A few numerically generated stability diagrams for Eq. (2.15) are now presented. We restrict ourselves to $\bar{a} = 0.7$ as before along with $\psi = \pi/4$.

A sketch of a subset of the full parameter space is shown in Fig. 2.9. Figure 2.10 shows the stability diagram in the parameter plane $\epsilon_0 = 0$, and Fig. 2.11 shows the stability diagrams on portions of the two orthogonal planes $\epsilon_1 = 0$, and $\epsilon_0 = 0$ respectively.

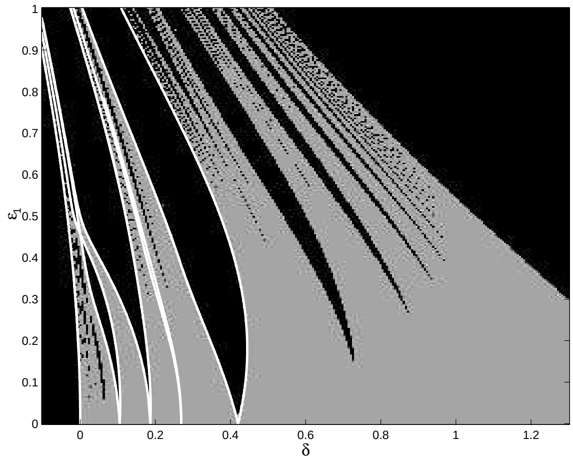

Figure 2.10: Stability diagram for Eq. (2.15) with $\epsilon_0 = 0$, $\psi = \pi/4$, $\bar{a} = 0.7$; and $N = 600$. Gray = stable, black = unstable, white = periodic solution.

Figure 2.12 shows the stability diagram on $\epsilon_1 = 0.2$ plane and Fig. 2.13 shows the stability diagrams on planes $\epsilon_1 = 0.2$, and $\epsilon_0 = 0$ respectively. Numerical resolution limits the degree of detail that can be trusted in the figures. With more computation time, any of these figures could be regenerated with higher precision and resolution. However, our key point in producing these figures is to emphasize that the white lines, representing numerically obtained periodic solutions, were in fact computed accurate to 9 decimal places. Moreover, we did find periodic solutions on *every* stability boundary that we examined, verifying the theoretical results obtained above.

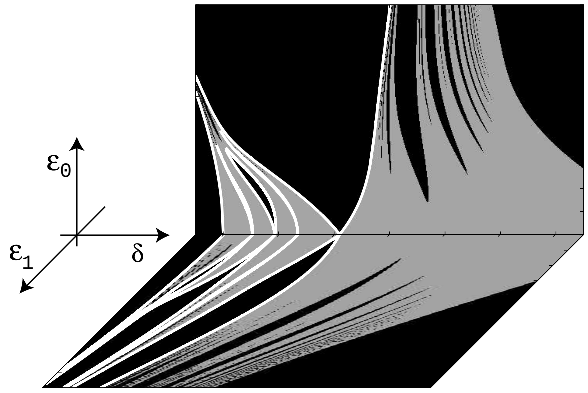

Figure 2.11: Stability diagram for Eq. (2.15) with $\psi = \pi/4$, $\bar{a} = 0.7$, and $N = 600$, on two different parameter planes. Figure 2.10 is included but now is horizontal.

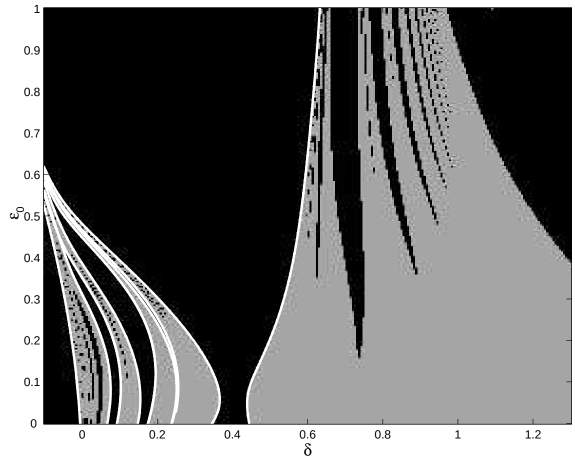

Figure 2.12: Stability diagram for Eq. (2.15) with $\epsilon_1 = 0.2$, $\psi = \pi/4$, $\bar{a} = 0.7$; and $N = 600$. Gray = stable, black = unstable, white = periodic solution.

2.8 Concluding remarks

We have numerically and theoretically studied asymmetric Mathieu equations, which are strongly nonlinear but conservative, and have scaleable solutions (if $x(t)$ is a solution, then

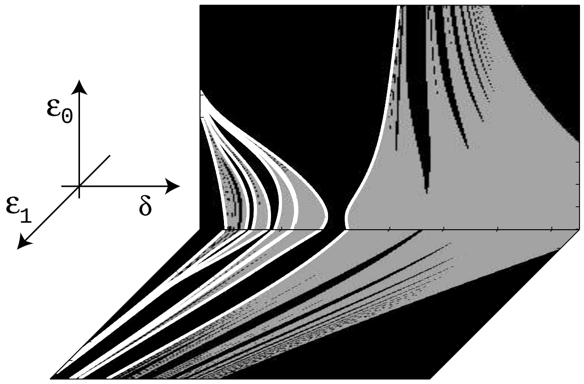

Figure 2.13: Stability diagram on the planes $\epsilon_1 = 0.2$ and $\epsilon_0 = 0$; again, $\bar{a} = 0.7$ and $\psi = \pi/4$, and $N = 600$.

so is $\alpha x(t)$ with $\alpha > 0$). We have found that there are infinitely many more instabilities for this system than for the usual Mathieu equation. There are periodic solutions on every stability boundary in the parameter space. The periods of these solutions are not confined to either 2π or 4π; higher multiples of 2π occur. Our theoretical results are also applicable to asymmetric Hill's equations.

Several questions seem interesting and relevant which we have been unable to answer here. For Eq. (2.1), are there in fact infinitely many instability regions of strictly nonzero width emanating from any finite interval on the δ axis? How do the widths of these regions, say for small ϵ and for an $m : n$ resonance, depend on m, n and ϵ? Given an arbitrary point (δ, ϵ) with $\epsilon > 0$, does every open set in the parameter plane that contains this point also contain an unstable point? Given some small damping, how much of which instability regions will survive? We hope that future work may shed some light on these issues.

Chapter 3

Multiple scales analysis of early and delayed boundary ejection in Paul traps

In this chapter, we study dynamics associated with early and delayed ejection observed in Paul traps operated in mass selective ejection mode. In particular, we study differences in the dynamics arising from higher order field superpositions of small magnitudes. The method of multiple scales is used to derive an approximate analytical expression which captures the slow variation in amplitude of ion motion near the stability boundary. The material of this chapter has been published in [8].

The work in this chapter was done in collaboration with Dr. Rajanbabu [7]. The perturbation expansion and analysis was mostly carried out by me, while the mass spectrometric interpretation and relevance was the contribution of Dr. Rajanbabu.

3.1 Introduction

Paul trap mass spectrometers consist of a three electrode mass analyzer with two end cap electrodes and a central ring electrode, all having hyperboloid geometry [14]. Ions of analyte gas, formed *in situ* by electron impact ionization, are trapped within the cavity by a trapping field formed by dc and rf potentials applied between the ring and end cap electrodes [14, 15]. The motion of ions within an *ideal* trap is governed by two uncoupled, linear Mathieu equations [3, 14] given by

$$\frac{d^2u}{d\tau^2} + (a_u + 2q_u \cos 2\tau)u = 0, \tag{3.1}$$

where u represents either the r (radial) or z (axial) direction of motion, and $\tau = \Omega t/2$, where in turn Ω is the angular frequency of the rf drive applied to the central ring electrode, and t is time. In Eq. (3.1), a_u and q_u are Mathieu parameters which determine ion stability within the trap.

In mass selective ejection experiments, the trap is operated along the $a_z = 0$ axis (by setting dc potential to zero) [16] of the Mathieu stability plot [15] and ions are destabilized from the trap by ramping rf amplitude to cause the ion's q_z value to cross the stability boundary at or near $q_z^* = 0.908046$. In practical traps it is known that small field inhomogeneities, which arise due to geometric imperfections and experimental constraints, cause ions to get ejected at smaller or larger q_z values (compared to $q_z^* = 0.908046$) resulting in the observation of early or delayed ejection, respectively. Wells *et al.* (1999) showed that these mass shifts arise on account of the interplay of two primary factors which include (1) presence of nonlinear fields (caused by holes in the end caps as well as truncation of the electrodes) within the trap cavity which tends to delay ion ejection and (2) elastic and inelastic collisions of the ions with the bath gas which tend to shorten this delay. Franzen and coworkers ([17, 18, 19, 20]), in a series of numerical studies, showed that positive octopole and dodecapole superpositions cause ions to come out early (at $q_z < q_z^*$) and the presence of negative octopole and dodecapole superpositions or hexapole and decapole superpositions of either sign cause delayed ejection of ions (at $q_z > q_z^*$).

The main problem in studying ion behavior in the neighborhood of the Mathieu stability boundary is that it is not possible to derive a closed form solution for ion motion when field inhomogeneities are present. Sudakov [21] has presented an insightful analysis of the slow variation in amplitude of the ion motion, which he calls the "beat" envelope, near the stability boundary. He showed that in case of positive octopole superposition, there exists an effective potential well in the stable region. The width and depth of this well decreases as q_z approaches the stability boundary. In case of hexapole and negative octopole superpositions, the existence of a double well potential in the unstable region of the Mathieu stability plot causes delayed ejection of ions from the trap.

In this paper we present a detailed and systematic analytical study of ion ejection near the nominal stability boundary ($q_z^* = 0.908046$) for practical Paul traps. We go beyond the work of Sudakov [21] in three ways. First, we adopt a formal perturbation method, the method of multiple scales (MMS), which has enabled us to proceed up to the fourth order (Appendix B). This may be useful when the weights of multipole superpositions are relatively larger. However, we use only the second order slow flow for obtaining the phase portraits in this paper, since we have assumed weak multipole superpositions. Secondly, we have incorporated higher order multipoles (hexapole, octopole, decapole and dodecapole superpositions). Finally, we use phase portraits to provide an alternative view of slow modulation dynamics as the ions approach the stability boundary, to understand early and delayed ejection of ions. Our results match Sudakov [21] up to second order, except for an apparent error in one of his terms, which we have corrected and verified.

As a technical matter, we mention that the application of the MMS at the stability boundary involves somewhat greater complications than the application of the MMS, or the related method of averaging [22], to resonant points inside the nominal stability region because in the latter case the unperturbed equation has two linearly independent *periodic* solutions.

3.2 Equation of motion

In the literature, the potential distribution inside a trap with field inhomogeneities in terms of spherical coordinates (ρ, θ, φ) is given by [17, 23]

$$\phi(\rho, \theta, \varphi) = \phi_0 \sum_{n=-\infty}^{\infty} A_n \frac{\rho^n}{r_0^n} P_n(\cos\theta), \tag{3.2}$$

where P_n is the Legendre polynomial of order n, A_n is the dimensionless weight factor for the n^{th} multipole term, ρ is the radial position and r_0 is chosen to be the radius of the central ring electrode in our study. ϕ_0 is given by

$$\phi_0 = U + V\cos\Omega t, \tag{3.3}$$

where U is the applied dc potential, and V and Ω are the amplitude and angular frequency, respectively, of the applied rf. In this study we consider higher order multipoles (hexapole, octopole, decapole and dodecapole) corresponding to A_3, A_4, A_5 and A_6, respectively, in Eq. (3.2). We use the notation and sign convention of Beaty [23] for representing the higher order multipoles. Since our focus is on the axial (z) instability, we set $r \equiv 0$. Following the procedure adopted by Sevugarajan and Menon [24] and Abraham *et al.* [25], the uncoupled equation of motion of trapped ions in the axial (z) direction in an experimental trap reduces to a nonlinear Mathieu equation,

$$\frac{d^2x}{d\tau^2} + (a_z + 2q_z\cos 2\tau)\left(x + \frac{3h}{2}x^2 + 2fx^3 + \frac{5d}{2}x^4 + 3k\,x^5\right) = 0, \tag{3.4}$$

where x is the axial position of the ion normalized with respect to r_0, $\tau = \Omega t/2$, $h(= A_3/A_2)$, $f(= A_4/A_2)$, $d(= A_5/A_2)$ and $k(= A_6/A_2)$ are the proportion of hexapole, octopole, decapole and dodecapole nonlinearity, respectively, to the quadrupole superposition, A_2. Also, a_z and q_z are Mathieu parameters for the nonlinear trap and are given by

$$a_z = -\frac{8eA_2U}{mr_0^2\Omega^2}; \qquad q_z = -\frac{4eA_2V}{mr_0^2\Omega^2}, \tag{3.5}$$

where e/m is the charge to mass ratio of the ion.

In mass selective ejection experiments, where only the rf voltage is applied, the equation of motion takes the form

$$\frac{d^2x}{d\tau^2} + 2q_z\cos 2\tau\left(x + \frac{3h}{2}x^2 + 2fx^3 + \frac{5d}{2}x^4 + 3k\,x^5\right) = 0. \tag{3.6}$$

Ion destabilization occurs at the stability boundary (corresponding to $\beta_z = 1$) in the Mathieu stability plot [26]. In our discussion the q_z value at the nominal point of destabilization in *ideal* traps will be referred to as q_z^*, which happens to be 0.908046, as shown below.

In the method of multiple scales adopted here, we need to order the nonlinearities. The following ordering scheme has been adopted,

$$h = \frac{2\sqrt{\epsilon}\,\bar{h}}{3}, \quad f = \frac{\epsilon\bar{f}}{2}, \quad d = \frac{2\sqrt{\epsilon}\,\bar{d}}{5}, \quad k = \frac{\epsilon\bar{k}}{3}, \tag{3.7}$$

where $\bar{h}$, $\bar{f}$, $\bar{d}$, $\bar{k}$ and ϵ will determine the strengths of the nonlinearities. Note that all even superpositions have been ordered as ϵ and odd superpositions as $\sqrt{\epsilon}$. Moreover, $\bar{h}$, $\bar{f}$, $\bar{d}$ and $\bar{k}$ are of $\mathcal{O}(1)$, with the "smallness" of these terms governed by $0 < \epsilon \ll 1$. Further, to study the dynamics near q_z^*, we introduce a detuning parameter Δ and write

$$q_z = q_z^* + \epsilon\Delta. \tag{3.8}$$

Thus by assigning negative and positive values to Δ, we can study the dynamics associated with early and delayed ejection, respectively.

Substituting Eqs. (3.7) and (3.8) into Eq. (3.6), the governing equation of our system takes the form

$$\frac{d^2x}{d\tau^2} + 2(q_z^* + \epsilon\Delta)\cos 2\tau\left(x + \sqrt{\epsilon}\,\bar{h}x^2 + \epsilon\bar{f}x^3 + \sqrt{\epsilon}\,\bar{d}x^4 + \epsilon\bar{k}x^5\right) = 0. \tag{3.9}$$

3.3 Analysis using multiple scales

In the method of multiple scales [27, 28, 29, 30], we assume that the solution to the original equation can be represented as a function of multiple time scales. Here, we choose $T_0 = \tau$, $T_1 = \sqrt{\epsilon}\tau$, $T_2 = \epsilon\tau$, $\cdots$. T_0 is the fast (usual) time and T_1, T_2, $\cdots$ are the *slow* times. This particular choice is justified in Appendix C. The solution $x(\tau)$ to Eq. (3.9) is sought in the form

$$x(\tau) = X(T_0, T_1, T_2, \cdots). \tag{3.10}$$

Further, X is expanded as

$$\begin{aligned} X(T_0, T_1, T_2, \cdots) &= X_0(T_0, T_1, T_2, \cdots) + \sqrt{\epsilon}\,X_1(T_0, T_1, T_2, \cdots) \\ &\quad + \epsilon\,X_2(T_0, T_1, T_2, \cdots) + \epsilon\,\sqrt{\epsilon}\,X_3(T_0, T_1, T_2, \cdots) + \mathcal{O}(\epsilon^2). \end{aligned} \tag{3.11}$$

The derivatives with respect to τ are

$$\frac{d(.)}{d\tau} = \frac{\partial(.)}{\partial T_0} + \sqrt{\epsilon}\frac{\partial(.)}{\partial T_1} + \epsilon\frac{\partial(.)}{\partial T_2} + \mathcal{O}(\epsilon\sqrt{\epsilon}), \tag{3.12}$$

$$\frac{d^2(.)}{d\tau^2} = \frac{\partial^2(.)}{\partial T_0^2} + 2\sqrt{\epsilon}\frac{\partial^2(.)}{\partial T_0 \partial T_1} + \epsilon\left(\frac{\partial^2(.)}{\partial T_1^2} + 2\frac{\partial^2(.)}{\partial T_0 \partial T_2}\right) + \mathcal{O}(\epsilon\sqrt{\epsilon}). \tag{3.13}$$

Substituting Eqs. (3.11) through (3.13) in Eq. (3.9), expanding and collecting terms using a symbolic algebra package (MAPLE), we obtain

$$\begin{aligned}\frac{\partial^2 X_0}{\partial T_0^2} + 2q_z^* \cos(2T_0)X_0 + \sqrt{\epsilon}\left[\frac{\partial^2 X_1}{\partial T_0^2} + 2q_z^* \cos(2T_0)\Big(X_1 + \bar{h}X_0^2 + \bar{d}X_0^4\Big) + 2\frac{\partial^2 X_0}{\partial T_0 \partial T_1}\right] \\ +\epsilon\left[\frac{\partial^2 X_2}{\partial T_0^2} + \frac{\partial^2 X_0}{\partial T_1^2} + 2\frac{\partial^2 X_0}{\partial T_0 \partial T_2} + 2\frac{\partial^2 X_1}{\partial T_0 \partial T_1} + 2\cos(2T_0)\Big(q_z^* X_2 + 2q_z^*\bar{h}X_0X_1 + q_z^*\bar{f}X_0^3\right. \\ \left. +2q_z^*\bar{d}X_0^3X_1 + q_z^*\bar{k}X_0^5 + \Delta X_0\Big)\right] + \mathcal{O}(\epsilon\sqrt{\epsilon}) = 0 \quad (3.14)\end{aligned}$$

As is usual for the MMS, we will solve the above sequentially for different orders (powers of ϵ). Indeterminacy in the solution at each stage, as usual, will be eliminated by insisting on a bounded solution at the next stage (a process called removal of secular terms). However, the form of the secular terms, and our process of identifying them, is somewhat unusual and described in detail below. Note that, for our higher order calculations, we retained more terms in the above expansion, these are not presented here for the sake of brevity.

3.3.1 Solution at $\mathcal{O}(1)$

From Eq. (3.14) at $\mathcal{O}(1)$, we have the linear Mathieu equation

$$\frac{\partial^2 X_0}{\partial T_0^2} + 2\,q_z^* \cos(2T_0)X_0 = 0. \quad (3.15)$$

Since this equation corresponds to the ion motion at the boundary ($q_z = q_z^*$), the solution consists of a 2π-periodic function and a linearly growing function [4].

Let the periodic function be ξ_1. It can be written as a cosine series given by

$$\xi_1 = \sum_{k=0}^{M} a_k \cos\Big((2k+1)\,T_0\Big), \quad (3.16)$$

where $M = \infty$ for the exact solution, but we will truncate the series at a suitably large value of M. In our computation, we set $M = 12$.

To obtain (or rather, verify) the numerical value of q_z^*, we substitute the truncated cosine series into Eq. (3.15). Collecting the coefficients of the harmonics retained in the approximation (Eq. (3.16)) and equating them to zero, we get $M + 1$ simultaneous linear equations in unknown a_k's. For nontrivial solutions to exist, the determinant of the coefficient matrix, which is a polynomial in q_z^*, must be zero. When this equation is solved, the smallest root gives $q_z^* = 0.908046$. In what follows, we take[1] $q_z^* = 0.908046$.

In order to obtain the a_k's (and thus ξ_1), we substitute $q_z^* = 0.908046$ into the $M+1$ linear equations obtained earlier. Since the $M+1$ equations are linearly dependent, we choose $a_0 = 1$ for convenience, drop the equation corresponding to the coefficient of $\cos(T_0)$, and use the remaining M equations to find the remaining a_k's.

The linearly growing part of the solution of Eq. (3.15) has the form $\xi_2 + T_0\,\xi_1$ [4], where ξ_2 is 2π-periodic. When this form is inserted into Eq. (3.15), we get the following differential equation for ξ_2 as

$$\ddot{\xi}_2 + 2\,q_z^*\,\cos(2T_0)\,\xi_2 = -2\,\dot{\xi}_1. \tag{3.17}$$

ξ_2 can be approximated by a truncated Fourier series as

$$\xi_2 = \sum_{k=0}^{M} b_k \sin\Big((2k+1)\,T_0\Big), \tag{3.18}$$

where, again, we use $M = 12$. Substituting this into the differential equation for ξ_2 and collecting terms, we get $M+1$ linear simultaneous equations which can be directly solved to obtain the b_k's. We tabulate the a_k's and b_k's obtained in our computations in Table 3.1. The a_k's and b_k's progressively decrease in magnitude and their numerical values for $k > 6$ are not presented here, although $M = 12$ and many digits of precision were used in our MAPLE calculation. It is clear that choosing $M = 12$ is more than enough for practical purposes.

The general solution to Eq. (3.15) can then be written as

$$X_0 = A(T_1, T_2)\,\xi_1(T_0) + B(T_1, T_2)\Big(\xi_2(T_0) + T_0\,\xi_1(T_0)\Big), \tag{3.19}$$

where A and B are arbitrary functions of T_1 and T_2.

We now set $B \equiv 0$ which eliminates the rapidly growing part in Eq. (3.19). This may initially seem somewhat arbitrary. Note, however, that by choosing $B \equiv 0$, we can

---

[1] More digits were retained in our calculations using MAPLE. For verification by interested readers, $q_z^* = 0.9080463337...$

Table 3.1: Values of a_k's and b_k's.

k	a_k	b_k
0	$1.00000000\cdots$	$-1.13521939\cdots$
1	$0.10126539\cdots$	$-0.18286643\cdots$
2	$0.00368062\cdots$	$-0.00812047\cdots$
3	$0.00006822\cdots$	$-0.00017002\cdots$
4	$0.00000076\cdots$	$-0.00000208\cdots$
5	$0.57401517 \times 10^{-8}$	$-0.16624533 \times 10^{-7}$
6	$0.30842821 \times 10^{-10}$	$-0.94071713 \times 10^{-10}$

obtain *one* solution and numerics will show that the solution so obtained is useful. For a similar example of setting the coefficient of a rapidly increasing term to zero and relevant discussion, see Chatterjee and Chatterjee [31]. Thus the solution to the $\mathcal{O}(1)$ equation is taken as

$$X_0 = A(T_1, T_2)\,\xi_1(T_0). \tag{3.20}$$

It may be noted that ξ_2 does not appear in X_0 in Eq. (3.20). However, ξ_2 will be required in the subsequent analysis.

3.3.2 Solution at $\mathcal{O}(\sqrt{\epsilon})$

Before we go to $\mathcal{O}(\sqrt{\epsilon})$, consider

$$\ddot{x} + P(t)\dot{x} + Q(t)x = R(t), \tag{3.21}$$

where $P(t), Q(t), R(t)$ are bounded, periodic functions with period T. Assume that the complementary solution to Eq. (3.21) is a linear combination of h_1 and $h_2 + \alpha\, t\, h_1$ where h_1 and h_2 are T-periodic and α is some nonzero constant. Das and Chatterjee [32] show that secular terms in the solution to Eq. (3.21) do not grow in amplitude faster than t^2. Moreover, under arbitrary but periodic forcing, secular terms in the particular solution are a linear combination of $t\,(2h_2 + \alpha\, t\, h_1)$ and $t\, h_1$. We will use these results below.

We now return to Eq. (3.14) at $\mathcal{O}(\sqrt{\epsilon})$, and we have

$$\frac{\partial^2 X_1}{\partial T_0^2} + 2\, q_z^* \cos(2T_0) X_1 = -2\, \frac{\partial^2 X_0}{\partial T_0 \partial T_1} - 2\, q_z^* \cos(2T_0)\left(\bar{h} X_0^2 + \bar{d} X_0^4\right). \tag{3.22}$$

We note the similarity between Eq. (3.22) and Eq. (3.21) by identifying

$$x \equiv X_1,\; P(t) \equiv 0,\; Q(t) \equiv 2q_z^* \cos(2T_0),\; R(t) \equiv -2\, \frac{\partial^2 X_0}{\partial T_0 \partial T_1} - 2\, q_z^* \cos(2T_0)\left(\bar{h} X_0^2 + \bar{d} X_0^4\right).$$

The complementary solution to Eq. (3.22) is a linear combination of ξ_1 and $\xi_2 + T_0\, \xi_1$ where ξ_1 and ξ_2 are given by Eqs. (3.16) and (3.18) and are 2π-periodic. Therefore, secular terms in the particular solution are a linear combination of $T_0\,(2\xi_2 + T_0\,\xi_1)$ ($\alpha = 1$ in our case) and $T_0\,\xi_1$. The general solution to Eq. (3.22) can be written as [32]

$$X_1 = c_1\xi_1 + c_2(\xi_2 + T_0\xi_1) + c_3 T_0\,\xi_1 + c_4 T_0\,(2\xi_2 + T_0\,\xi_1) + \Psi(T_0), \tag{3.23}$$

where c_1 through c_4 are constants and Ψ is 2π-periodic in T_0. Moreover, c_1 and c_2 are arbitrary, being part of the complementary solution. One linearly growing part of the particular solution can be nullified by a linearly growing part of the complementary solution (by choosing $c_2 = -c_3$). Although c_2 is thereby fixed, c_1 is still arbitrary. We now choose c_1 such that it nullifies the coefficient of $\cos(T_0)$ in $\Psi(T_0)$. By these arguments and simplifications,

$$X_1 = c_4 T_0\,(2\,\xi_2 + T_0\,\xi_1) + \Psi(T_0), \tag{3.24}$$

where $\Psi(T_0)$ is 2π-periodic and has no $\cos(T_0)$ term. That is,

$$X_1 = C_{2N+1} + \sum_{k=2}^{N} C_k \cos(kT_0) + \sum_{k=1}^{N} C_{k+N} \sin(kT_0) + C_{2N+2}\, T_0\,(2\xi_2 + T_0\xi_1), \tag{3.25}$$

where N is some positive integer (here we have taken $N = 12$) and C_k's are coefficients to be determined. Note that $\cos(T_0)$ has been left out above.

Since ξ_1 and ξ_2 are approximate and the periodic part of X_1 is also approximate, the form of X_1 satisfies Eq. (3.22) only approximately. Therefore, after substituting Eq. (3.25) into Eq. (3.22), the left hand side will not be exactly equal to the right hand side. Bringing all terms to the left hand side, we obtain a nonzero residual. The unknown C_k's are determined by carrying out the Galerkin projection procedure used in a related context by Das and Chatterjee [32]. In this procedure the residual is separately multiplied by each basis function in the assumed form of the general solution (right hand side of Eq. (3.25)), namely

$$1,\ T_0\,(2\xi_2+T_0\xi_1),\ \sin(T_0),\ \sin(2T_0),\ \cos(2T_0),\cdots,$$

and then each such product is integrated over one period (from 0 to 2π). Setting the integrals thus obtained to zero, we obtain $2N+1$ linear equations in the unknown coefficients C_k's. We solve for these coefficients and substitute them in Eq. (3.25) to obtain X_1.

A key point is that coefficient C_{2N+2} must be set to zero to avoid the secular terms and this, as is used in the MMS, enables us to obtain the slow flow. From MAPLE we obtain, at $\mathcal{O}(\sqrt{\epsilon})$:

$$C_{2N+2}=0.12873832\times 10^{-9}\,\bar{h}\,A^2-0.30186541\times 10^{-7}\,\bar{d}\,A^4-0.39256924\times 10^{-9}\,\frac{\partial A}{\partial T_1}. \quad (3.26)$$

We note that the numerical coefficients are very small. We need to determine if they are actually numerically corrupted versions of exactly zero, i.e., if they should be set to zero. Noting that, from the Galerkin procedure, we have simultaneously obtained

$$C_2=-0.67189535\,\bar{d}\,A^4-0.60163836\,\bar{h}\,A^2, \quad (3.27)$$

and

$$C_4=0.0045506\,\bar{d}\,A^4-0.006558\,\bar{h}\,A^2, \quad (3.28)$$

which involve much larger numerical coefficients, we conclude that C_{2N+2} is actually zero. Thus, we take $C_{2N+2}=0$, and obtain no useful information at this order. We must proceed to a higher order calculation.

There are some technical issues in doing this, regarding the *asymptotic* validity of the method, but good approximations will nevertheless be obtained. The technical issues related to asymptotic validity are identical to those discussed in Nandakumar and Chatterjee [33] for averaging, and are not discussed here. The solution X_1 is given in Appendix D.

3.3.3 Solution at $\mathcal{O}(\epsilon)$

We now proceed to $\mathcal{O}(\epsilon)$ which will provide useful information about the evolution of the amplitude A of the solution. From Eq. (3.14), at $\mathcal{O}(\epsilon)$, we have

$$\begin{aligned}\frac{\partial^2 X_2}{\partial T_0^2} + 2\, q_z^* \cos(2T_0) X_2 \;=\; & -\frac{\partial^2 X_0}{\partial T_1^2} - 2\,\frac{\partial^2 X_0}{\partial T_0 \partial T_2} - 2\,\frac{\partial^2 X_1}{\partial T_0 \partial T_1} \\ & -2\,\cos(2T_0) X_0 - 2\,\cos(2T_0)\, q_z^* \Bigg(2\bar{h}\, X_0 X_1 + \bar{f}\, X_0^3 \\ & +2 q_z^* \bar{d} X_0^3 X_1 + q_z^* \bar{k} X_0^5\Bigg). \qquad (3.29)\end{aligned}$$

Equation (3.29) also fits the form of Eq. (3.21). As was done for X_1 at $\mathcal{O}(\sqrt{\epsilon})$, here we take

$$X_2 = D_{2N+1} + \sum_{k=2}^{N} D_k \cos(kT_0) + \sum_{k=1}^{N} D_{k+N} \sin(kT_0) + D_{2N+2}\, T_0\, (2\xi_2 + T_0 \xi_1), \qquad (3.30)$$

where $N = 12$ as earlier, and D_k's are coefficients to be determined. We follow the Galerkin projection procedure again (as described earlier) to solve for the unknown D_k's. Setting D_{2N+2} equal to zero, we obtain

$$\begin{aligned}& -1.9438\, \bar{h}^2 A^3 + 0.44483\, \bar{f} A^3 - 4.7213\, \bar{d}^2 A^7 + 0.48561\, \bar{k} A^5 \\ & \qquad -6.4286\, \bar{h}\bar{d}\, A^5 + 0.43865\, \Delta\, A - 0.50000\, \frac{\partial^2 A}{\partial {T_1}^2} = 0. \qquad (3.31)\end{aligned}$$

From Eq. (3.13), we have

$$\ddot{A} = \frac{d^2 A}{d\tau^2} = \frac{\partial^2 A}{\partial T_0^2} + 2\sqrt{\epsilon}\frac{\partial^2 A}{\partial T_0 \partial T_1} + \epsilon \left(\frac{\partial^2 A}{\partial T_1^2} + 2\frac{\partial^2 A}{\partial T_0 \partial T_2}\right) + \mathcal{O}(\epsilon\sqrt{\epsilon}). \qquad (3.32)$$

Since amplitude A is not a function of the fast variable T_0, we have

$$\ddot{A} = \epsilon\, \frac{\partial^2 A}{\partial T_1^2} + \mathcal{O}(\epsilon\sqrt{\epsilon}), \qquad (3.33)$$

giving the required slow flow as

$$\begin{aligned}\ddot{A} \;=\; & \epsilon \Bigg(0.8773\, \Delta A - 3.8877\, \bar{h}^2 A^3 + 0.8897\, \bar{f}\, A^3 - 12.8564\, \bar{h}\, \bar{d}\, A^5 \\ & +0.97122\, \bar{k}\, A^5 - 9.4429\, \bar{d}^2 A^7\Bigg) + \mathcal{O}(\epsilon\sqrt{\epsilon}). \qquad (3.34)\end{aligned}$$

Note that, after setting $D_{2N+2} = 0$, we also have X_2. The solution X_2 is provided in Appendix D and is needed for higher order calculations.

Equation (3.34) is the second order slow flow for ion motion in the presence of hexapole, octopole, decapole and dodecapole superpositions. The presence of ϵ and Δ in the equation enables us to visualize ion dynamics at different values of detuning from q_z^*. In order to compare these results with the beat envelope equations of Sudakov [21] (where separate equations were presented for hexapole and octopole superpositions), we plot the time trajectories predicted by these equations. To do this we transform the coefficients of Eq. (3.34) to the form of the beat envelope equations. Details of this comparative study are presented in Appendix E, where agreement is observed with Sudakov's results except for one erroneous numerical coefficient which we correct here.

Using this systematic approach we have actually carried out calculations up to the fourth order, and the final fourth order slow flow equation is given, for completeness, in Appendix B. This equation may be of use in the presence of somewhat larger weights of multipole superpositions. However, in the present study, we will use only the second order slow flow (Eq. (3.34)) for generating relevant phase portraits.

3.3.4 Numerical verification

We next check the correctness of the slow flow we have obtained. We do this by first integrating Eq. (3.9) numerically, using a standard routine ODE45 from MATLAB, with some initial conditions. Numerical tolerances of 10^{-8} are specified for the integration routine.

Figures 3.1, 3.2 and 3.3 show comparisons between numerically obtained solutions of Eq. (3.9) and amplitude obtained by solving the slow flow (Eq. (3.34)). In these plots we have selected $\epsilon = 0.001$, and the initial conditions for integration of Eq. (3.9) were taken as $x(0) = 0.01$ and $\dot{x}(0) = 0$. We obtain the corresponding initial conditions for the slow flow (Eq. (3.34)) by a method described in Appendix F. The values of parameters used are given in the respective figure captions. For the purpose of comparison of the two equations for a specific nonlinearity, the weights of the other superpositions are set to zero in both Eqs. (3.9) and (3.34).

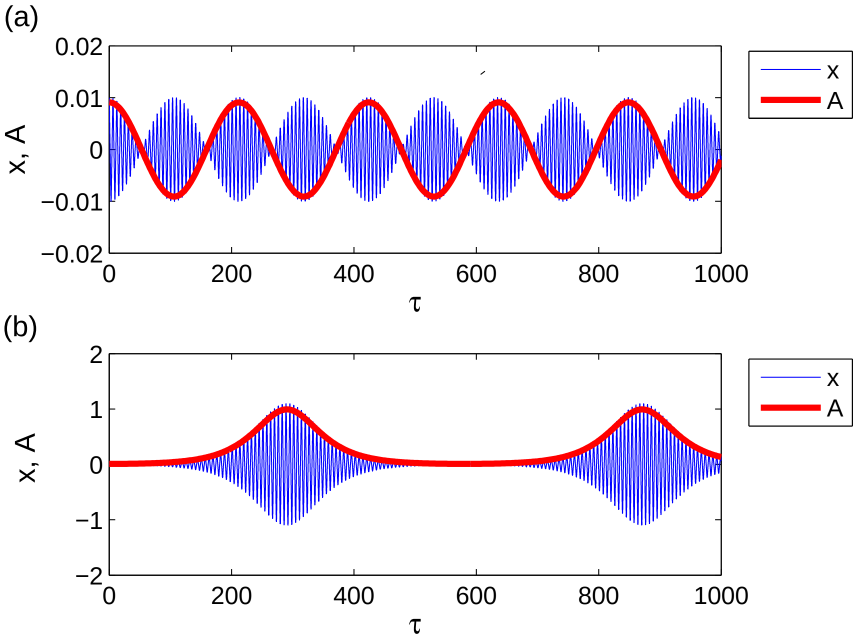

Figure 3.1: Comparison of amplitude (A) determined by solving the slow flow with the original Mathieu equation (x) for positive and negative octopole. In both plots, $\epsilon = 0.001$, $x(0) = 0.01$, $\dot{x}(0) = 0$, $A(0) = 0.0091$, $\dot{A}(0) = 0$ and $\bar{h} = \bar{d} = \bar{k} = 0$. Further, we use for (a) $\bar{f} = 1$, $\Delta = -1$; and for (b) $\bar{f} = -1$, $\Delta = 1$.

Figure 3.1(a) presents the results for positive octopole and Fig. 3.1(b) for negative octopole. From the figure, a good match can be seen between the full numerical solution and MMS approximation. Figures 3.2(a) and 3.2(b) show results for hexapole and decapole superpositions where the effect of nonlinearity is sign independent. Figure 3.3(a) shows the comparison for positive dodecapole while Fig. 3.3(b) is for negative dodecapole. From these plots, it can be observed that the slow flow adequately represents the slow temporal variation in amplitude of the system in the neighborhood of the stability boundary.

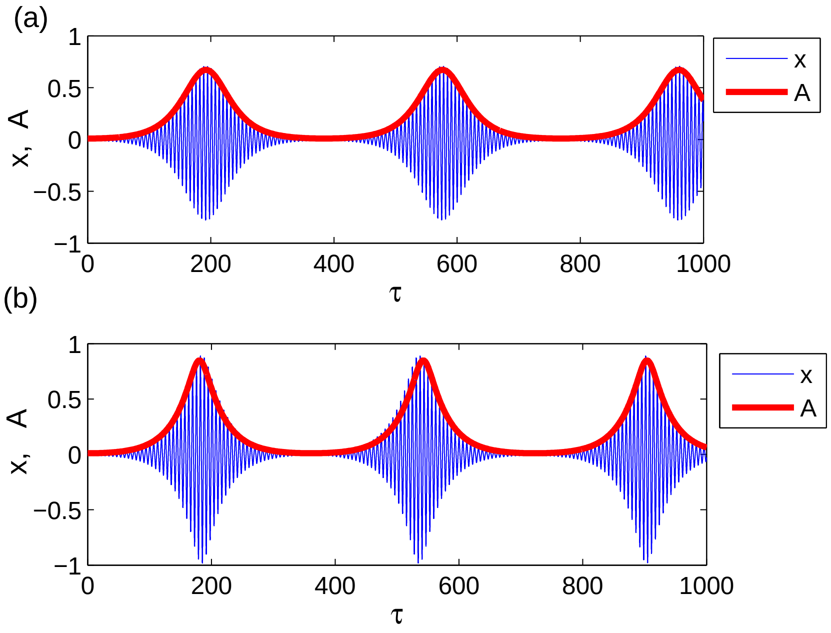

Figure 3.2: Comparison of amplitude (A) determined by solving the slow flow with the original Mathieu equation (x) for hexapole and decapole. In both plots, $\epsilon = 0.001$, $\Delta = 1$, $x(0) = 0.01$, $\dot{x}(0) = 0$ and $\bar{f} = \bar{k} = 0$. Further, we use for (a) $\bar{h} = 1$, $\bar{d} = 0$, $A(0) = 0.0091$, $\dot{A}(0) = 0$; and for (b) $\bar{d} = 1$, $\bar{h} = 0$, $A(0) = 0.0101$, $\dot{A}(0) = 0$.

3.4 Results and discussion

Equation (3.34) is the second order slow flow which describes variation in amplitude of ion motion in the presence of hexapole, octopole, decapole and dodecapole multipole superpositions. While the octopole ($\bar{f}$) and decapole ($\bar{k}$) appear as linear terms, the hexapole ($\bar{h}$) and decapole ($\bar{d}$) appear independently as quadratic terms as well as in combination in one of the terms. This last observation, namely that of $\bar{h}$ and $\bar{d}$ appearing as a combination, has two interesting consequences. First, the sign of the hexapole will affect dynamics only if decapole superposition is *also* present. Second, for the sign of hexapole superposition to affect ion dynamics its sign change must be independent of decapole superposition. These consequences are also borne out by the fourth order slow flow which includes a larger number of terms (see Appendix B and the caveats therein).

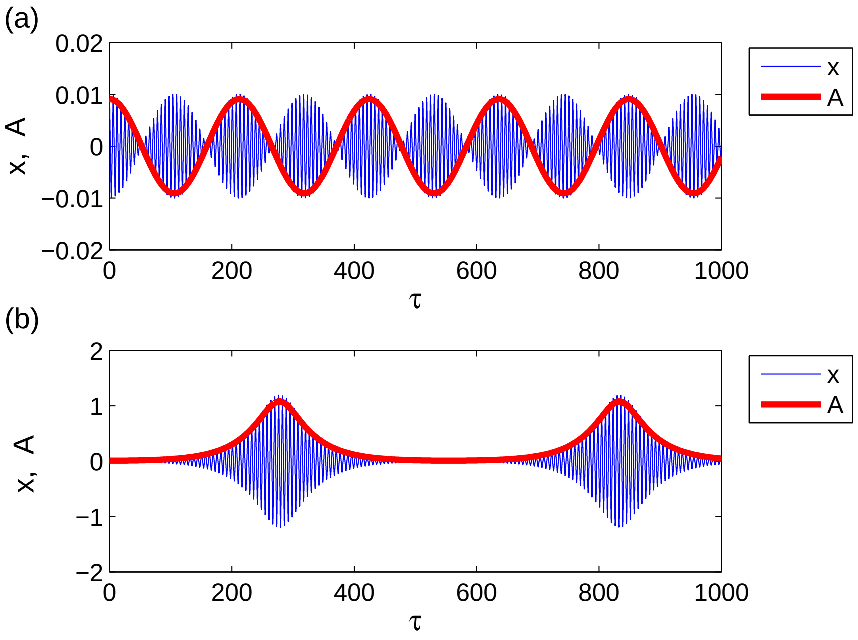

Figure 3.3: Comparison of amplitude (A) determined by solving the slow flow with the original Mathieu equation (x) for positive and negative dodecapole. In both plots, $\epsilon = 0.001$, $x(0) = 0.01$, $\dot{x}(0) = 0$, $A(0) = 0.0091$, $\dot{A}(0) = 0$ and $\bar{h} = \bar{f} = \bar{d} = 0$. Further, we use for (a) $\bar{k} = 1$, $\Delta = -1$; and for (b) $\bar{k} = -1$, $\Delta = 1$.

We now return to our original problem of understanding ion dynamics in the presence of field inhomogeneities. The nonlinearities considered here are hexapole, octopole, decapole and dodecapole. This study will rely on interpreting numerically generated phase portraits, obtained from the slow flow (Eq. (3.34)), at different values of Δ. In the phase portraits presented, we have varied Δ from -2 to $+8$, and the corresponding q_z values are presented in Table 3.2 for ready reference. These q_z values are calculated by substituting $q_z^* = 0.908046$ and $\epsilon = 0.001$ in Eq. (3.8). All the phase portraits are generated keeping the value of ϵ at 0.001. The slow flow equations are integrated repeatedly for a large number of initial conditions and the phase portraits are obtained by plotting the derivative of the amplitude ($\dot{A}$) on the y-axis and amplitude (A) on the x-axis.

Table 3.2: q_z at different values of Δ, for $\epsilon = 0.001$.

Δ	q_z
-2.0	0.9060463
-1.0	0.9070463
-0.5	0.9075463
-0.1	0.9079463
-0.001	0.9080453
0.25	0.9082963
0.6	0.9086463
1.0	0.9090463
2.0	0.9100463
8.0	0.9160463

3.4.1 Positive octopole

We set $\bar{h} = \bar{d} = \bar{k} = 0$ in Eq. (3.34) to study the effect of octopole superpositions. The right hand side of Eq. (3.34) is a cubic polynomial in amplitude, A. The roots of this polynomial are

$$(-0.9940\sqrt{-\Delta/\bar{f}},\ 0),\quad (0,0)\ \text{ and }\ (0.9940\sqrt{-\Delta/\bar{f}},\ 0).$$

These, if real, are also the fixed points of the slow flow. Since $\bar{f}$ is positive, for positive values of Δ, there exists only one fixed point at $(0,0)$ and this is a saddle, indicating that the ion is unstable. For negative Δ values, however, there are three fixed points. For instance, for $f = 0.01$ (i.e., $\bar{f} = 20$ for $\epsilon = 0.001$) and $\Delta = -2$, these fixed points occur at $A = 0$, $A = \pm 0.3143$. The two nonzero fixed points are now saddles and consequently ions will be stable only near the origin (a center) where the solution is bounded. As we vary Δ from -2 towards 0 (that is, towards the stability boundary), the non-zero fixed points move towards each other. This can be observed from the Figs. 3.4(a) to 3.4(d) which show the phase portraits generated by numerically integrating Eq. (3.34). For $\Delta = -0.5, -0.1, -0.001$, the nonzero fixed points are ± 0.1572, ± 0.0703, ± 0.00703, respectively.

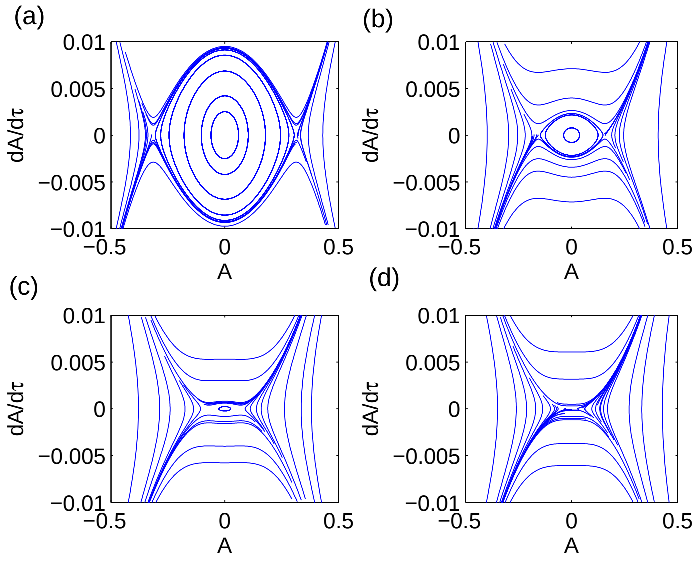

Figure 3.4: Phase portrait for 1% octopole ($f = 0.01$, $\bar{f} = 20$, $\epsilon = 0.001$) for Δ values of (a) -2, (b) -0.5, (c) -0.1 and (d) -0.001.

From Figs. 3.4(a) through 3.4(d), it can also be observed that the area of the region around the center where the solution is bounded diminishes as Δ is varied from -2 to -0.001, and ions with initial conditions which would earlier have been stable now are unstable and escape to infinity. For Δ values very close to 0, but less than 0, the area in the phase space where the solution is bounded is so small that all ions with significant energies escape. The phase portraits present qualitatively a similar picture as Sudakov's [21] observation that for positive octopole there is a potential well within the stable region and the width and depth of this well decreases as q_z approaches the boundary. In the context of our study, the central region in the phase portrait (with closed curves) corresponds to the potential well discussed by Sudakov [21].

3.4.2 Negative octopole

We now consider the ion dynamics in the neighborhood of the stability boundary with 1% negative octopole nonlinearity. Since $\bar{f}$ is negative, for negative values of Δ, Eq. (3.34)

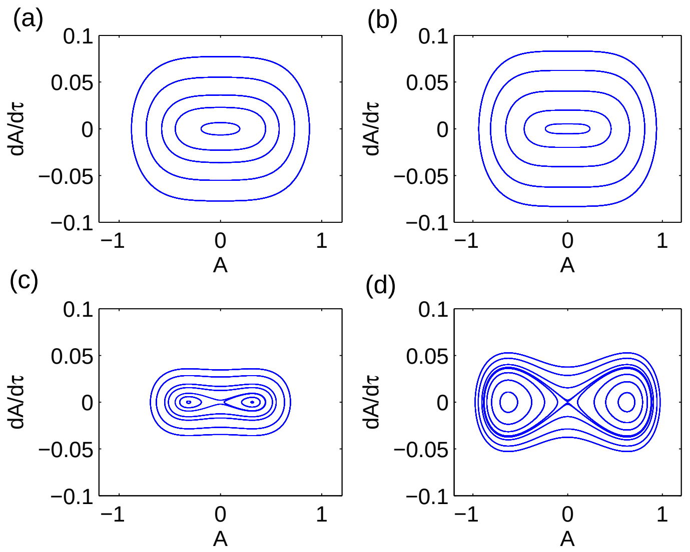

Figure 3.5: Phase portrait for −1% octopole ($f = 0.01$, $\bar{f} = 20$, $\epsilon = 0.001$) for Δ values of (a) −1, (b) 0, (c) 2 and (d) 8.

will have only one fixed point. This will be a center and hence ions will be stable. For positive values of Δ (i.e., beyond the nominal stability boundary), there exist 3 fixed points consisting of a saddle and two centers (one on each side of the saddle). Centers for $\Delta = 2$ are at $A = \pm 0.3143$ and for $\Delta = 8$ are at $A = \pm 0.6287$. As Δ is increased to values greater than 0, these centers move away from each other.

Figures 3.5(a) through 3.5(d) show the phase portraits generated by numerically integrating Eq. (3.34) for Δ values corresponding to −1, 0, 2 and 8, respectively, for 1% negative octopole nonlinearity. Referring to Figs. 3.5(a) and 3.5(b), there exists only one fixed point and this is a center. All ions which were originally located at the trap center will continue to execute stable oscillations and will not escape from the trap. When the q_z value of the ion is increased beyond q_z^* (where Δ is positive), the phase portrait qualitatively changes its nature. As can be seen from Figs. 3.5(c) and 3.5(d), the origin which was earlier a center now becomes a saddle and two new centers are created. Thus an ion will have a choice of oscillating in a path (in averaged or slow phase space) that encircle either one of the centers, or both centers. For very small positive values of Δ, ion amplitude does not exceed the trap boundary and ions are therefore confined within the trap cavity. Increasing the detuning parameter Δ increases the maximum amplitude that an ion oscillation encircling a center can have. Eventually, for large enough Δ, ion motion amplitudes exceed the trap dimensions, and so the ions get ejected (also see numerical simulation of this phenomenon in Sudakov [21]). Thus, in the presence of negative octopole superposition, ion oscillations continue to be inherently stable well beyond q_z^* and ions escape from the trap only when amplitudes reach the trap boundary.

Here too, our results are supported by Sudakov's [21] observation of a double well potential function for negative octopole superposition. The regions around the two centers (with closed curves) on either side of the saddle, observed for positive values of Δ, correspond to the double well potential shown in that study.

3.4.3 Hexapole

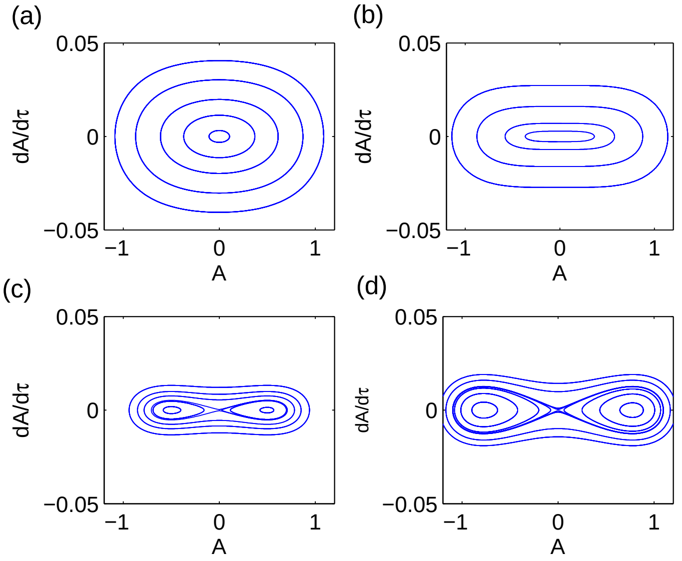

Figure 3.6: Phase portrait for 1% hexapole ($h = 0.01$, $\bar{h} = 0.47$, $\epsilon = 0.001$) for Δ values of (a) -1, (b) 0, (c) 0.25 and (d) 0.6.

The effect of hexapole superposition can be studied by setting $\bar{f} = \bar{d} = \bar{k} = 0$ in

Eq. (3.34). It is observed that the hexapole nonlinearity parameter $\bar{h}$ appears in squared form which implies that the sign of hexapole nonlinearity will not affect the slow flow. The roots of the polynomial obtained by equating the right hand side of Eq. (3.34) to zero are

$$(-0.4750\sqrt{\Delta/\bar{h}^2}\,,0),\quad (0,0)\ \text{ and }\ (0.4750\sqrt{\Delta/\bar{h}^2}\,,0).$$

For negative values of Δ there will be only one fixed point at (0, 0) and this will be a center. When Δ takes positive values, similar to the case of negative octopole nonlinearity, two centers and a saddle will appear. Figures 3.6(a) through 3.6(d) show the phase portraits for 1% positive hexapole superposition (i.e., $\bar{h} = 0.47$ for $\epsilon = 0.001$) for Δ values -1, 0, 0.25 and 0.6, respectively. As can be seen from these figures, we get the same qualitative behavior as we obtained in case of the negative octopole nonlinearity, for both negative and positive values of Δ. This observation can also be understood from Eq. (3.34) where the qualitative behavior of the slow flow for the hexapole nonlinearity (in the absence of all others) will become similar to the slow flow for the *negative* octopole nonlinearity (in the absence of all others).

3.4.4 Decapole

To study the effect of decapole superposition we set $\bar{h} = \bar{f} = \bar{k} = 0$ in Eq. (3.34). The slow flow equation reduces to

$$0.8773\,\Delta A - 9.4429\,\bar{d}^2 A^7 = 0. \tag{3.35}$$

Figures 3.7(a) to 3.7(d) show the phase portraits for 1% decapole superposition (i.e., $\bar{d} = 0.79$ for $\epsilon = 0.001$). The phase portraits are qualitatively similar to the phase portraits obtained for hexapole superposition. As in the case of hexapole, delayed ejection is suggested by these phase portraits. The fixed point of the system when Δ is negative is (0,0). In this case the system exhibits stable oscillations. For positive values of Δ there will be three fixed points. For $\Delta = 0.25$ these are $(-0.5778, 0)$, $(0, 0)$ and $(0.5778, 0)$. From the phase portraits it can be observed that origin of the A-$\dot{A}$ plane is a saddle and the nonzero fixed points are centers. As Δ is increased to 2, the two nonzero fixed points move further apart to $(\pm 0.7857, 0)$. Ions are ejected from the trap when their amplitudes reach the trap boundary.

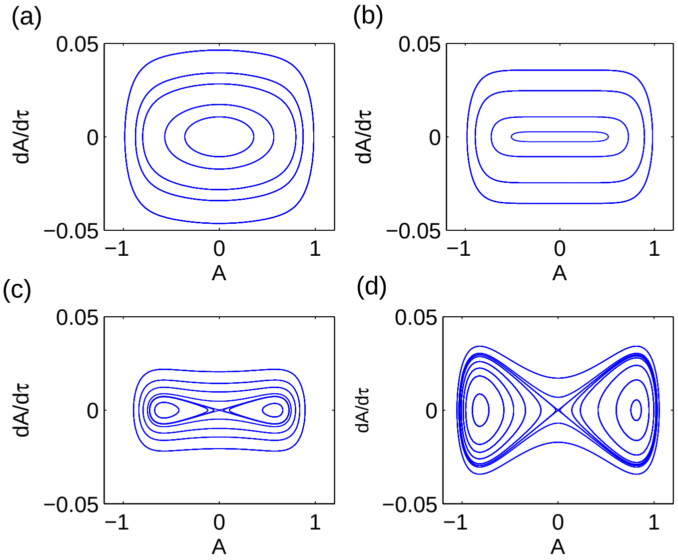

Figure 3.7: Phase portrait for 1% decapole ($d = 0.01$, $\bar{d} = 0.79$, $\epsilon = 0.001$) for Δ values (a) -1, (b) 0, (c) 0.25 and (d) 2.

3.4.5 Dodecapole

The influence of dodecapole nonlinearity may be investigated by setting $\bar{h} = \bar{f} = \bar{d} = 0$ in Eq. (3.34). The slow flow reduces to

$$0.8773\,\Delta A - 0.9712\,\bar{k}A^5 = 0. \tag{3.36}$$

The system represented by this equation has three fixed points when Δ is negative and $\bar{k}$ is positive. The phase portraits for 1% dodecapole superposition (i.e., $\bar{k} = 30$ for $\epsilon = 0.001$) are shown in Figs. 3.8(a) to 3.8(d). When $\Delta = -0.5$ the fixed points are $(-0.3503, 0)$, $(0, 0)$ and $(0.3503, 0)$. The two nonzero fixed points are saddles and the origin is a center. As Δ is increased (that is, when q_z approaches q_z^*) the two nonzero fixed points move closer to the origin. From Fig. 3.8(d) corresponding to $\Delta = -0.001$, the center is almost gone and almost all initial conditions lead to unbounded solutions (ejection).

When $\bar{k}$ is negative there exists only one fixed point at (0,0) for negative values of Δ. From Fig. 3.9(a), which is plotted for -1% dodecapole superposition at $\Delta = -1$, it

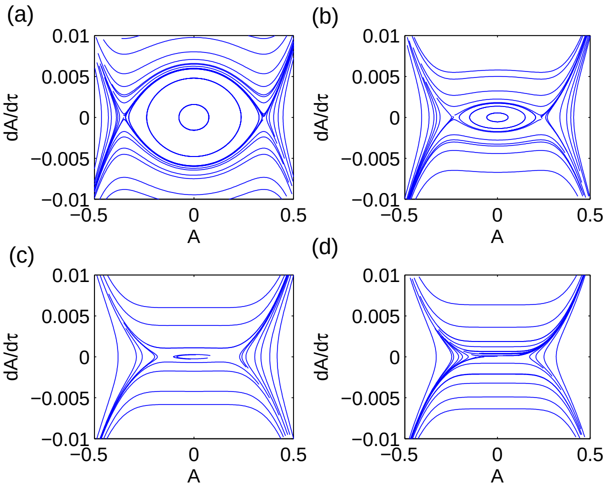

Figure 3.8: Phase portrait for 1% dodecapole ($k = 0.01$, $\bar{k} = 30$, $\epsilon = 0.001$) for Δ values of (a) -0.5, (b) -0.1, (c) -0.01 and (d) -0.001.

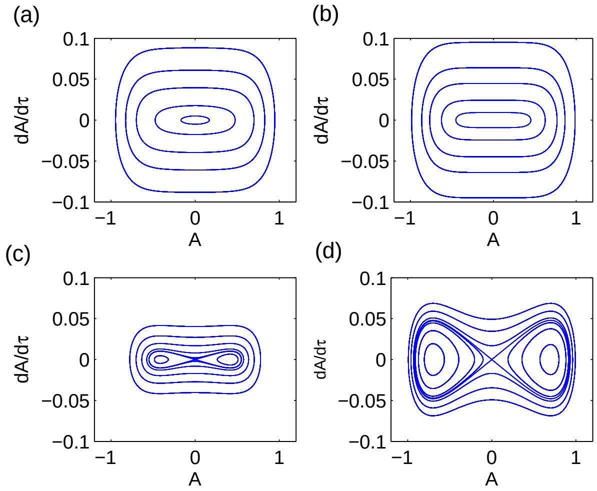

Figure 3.9: Phase portrait for -1% dodecapole ($k = 0.01$, $\bar{k} = 30$, $\epsilon = 0.001$) for Δ values of (a) -1, (b) 0, (c) 1 and (d) 8.

can be seen that the system exhibits stable oscillations. However, for positive values of Δ there are three fixed points. Figures 3.9(c) and 3.9(d) corresponding to $\Delta = 1$ and $\Delta = 8$, respectively, show that the nonzero fixed points are centers and the origin is a saddle. Ions are ejected from the trap when the ion oscillation amplitude reaches the trap boundary.

3.5 Concluding remarks

The motivation of this chapter was to understand the dynamics associated with early and delayed ejection of ions in practical Paul traps operated in the mass selective ejection mode. The studies reported in this chapter will be of use in understanding dynamics at the stability boundary in all traps where the nonlinear Mathieu equation determines ion stability.

The equation of motion of ions in the axial direction of the trap with hexapole, octopole, decapole and dodecapole superpositions was studied using the method of multiple scales. The ordering scheme used has allowed a systematic inclusion of higher order multipoles. Details of the analysis has been provided and our results are compared with those of Sudakov [21]. Although a fourth order slow flow equation has been computed and reported for potential future use in traps with larger weights of multipole superpositions, in our present study we have used the second order slow flow (Eq. (3.34)) for generating our phase portraits. Phase portraits generated by numerical integration of the slow flow have been used to predict the qualitative behavior of ion motion near the stability boundary in the presence of nonlinearities. The presence of positive even multipoles was seen to cause early ejection and negative even multipoles to cause delayed ejection of ions. Independently present odd multipoles of either sign have the same effect as negative even multipoles i.e. delayed ejection.

Chapter 4

Wave attenuation in nonlinear periodic structures

This chapter studies the attenuation, caused by weak damping, of harmonic waves through a discrete, periodic structure with frequency nominally within the Propagation Zone (i.e., propagation occurs in the absence of the damping). Adapting the transfer matrix method and using harmonic balance for the nonlinear terms, a four dimensional linear/nonlinear map governing the dynamics is obtained. We analyse this map by applying the method of multiple scales upto first order. The resulting slow evolution equations give the amplitude decay rate in the structure. The approximations are validated by comparing with other analytical solutions for the linear case and full numerics for the nonlinear case. The material of this chapter was published in [10].

4.1 Introduction

Periodic structures occur often in nature and engineering. Atomic lattices of pure crystals are examples found in nature. Multistoreyed buildings, elevated guideways for high speed transportation vehicles, multispan bridges, bladed disk assemblies in turbines, and stiffened shells in aircraft and ships provide examples in engineering.

The problem of wave propagation in periodic structures has received significant attention over the last four decades (see, e.g., [34]). The vast majority of papers on this topic have dealt with linear structures. There exists a large body of work on linear periodic structures. A beginning reader is referred to Mead's excellent review [34] and references therein. Significant contributions may also be found in, e.g., [35, 36, 37, 38, 39] (the list is incomplete, but representative). In this paper, we study wave propagation in nonlinear periodic structures using harmonic balance and multiple scales.

The main issues in the linear case can be outlined in the context of the structure sketched in Fig. 4.1. Assume zero damping and linear stiffness. If one end of a semi-infinite periodic structure is excited at a frequency ω then, lack of dissipation notwithstanding, a steady wave may fail to propagate with undiminished amplitude. Bands of frequencies in which waves do propagate with undiminished amplitude are called *propagation zones* (PZ). Bands where the amplitude diminishes are called *attenuation zones* (AZ). The number of distinct PZs equals the number of degrees of freedom of one period of the structure [34]. The *propagation constant* for a wave at a given frequency is the logarithm of the ratio of complex amplitudes of vibrations of successive elements. The real part of the propagation constant is called the attenuation constant and the imaginary part is called the phase constant. Zero attenuation corresponds to PZs while nonzero attenuation corresponds to AZs. Though propagation constants are most meaningful for linear structures (damped or undamped), a useful interpretation is possible in the case of propagating waves in weakly nonlinear but conservative periodic structures [9].

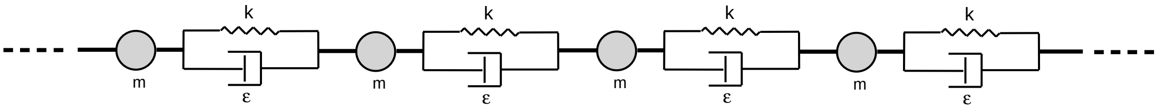

Figure 4.1: A periodic structure

The literature on harmonic wave propagation through weakly nonlinear periodic structures, in comparison to linear structures, is meagre. A likely reason is that the powerful and popular matrix based approaches in the frequency domain used for linear periodic structures run into trouble in the presence of nonlinearities. Recently, Mallik and

Chakraborty have studied *conservative* weakly nonlinear periodic structures [9]. They used single-frequency harmonic balance to describe the nonlinear behavior of a single period of the structure in the frequency domain, and developed a simple, amplitude-dependent, perturbation expansion of the propagation constant to elucidate several aspects of wave propagation phenomena in the presence of weak, conservative nonlinearities. However, they did not address damping (linear or nonlinear).

In this paper, we consider a weakly nonlinear, *damped* periodic structure. Using Mallik and Chakraborty's idea of harmonic balance in the periodic structures context, we obtain a weakly nonlinear map (as opposed to simply a transfer matrix) that approximately governs the wave propagation in such a structure. The propagation zones of the undamped structure now become zones of weak attenuation. We then use the method of multiple scales (MMS) for maps to study the weak attenuation in our structure. Note that the MMS for maps is not new [28, 40, 41]; its use for wave propagation in periodic structures is new, however. Our approach can also be used for other small perturbations to linear periodic structures within propagation zones, including conservative nonlinearities.

4.2 Weakly damped periodic structures

We will study the cases of linear and nonlinear damping along similar lines.

4.2.1 Linear damping

Consider the nth element E_n of a periodic structure consisting, for greatest simplicity, of a mass m, a linear spring of stiffness k, and a weak damper of coefficient ϵ (see Fig. (4.2)). We assume $0 < \epsilon \ll 1$. Successive elements interact through displacement and force at connecting points, as indicated. For linear damping, the damping force is $\epsilon(\dot{X}_n - \dot{X}_{n+1})$. Applying force and momentum balance on the nth element, and assuming a harmonic solution, we write

$$X_n = X_{n,c}\,\cos(\omega\, t) + X_{n,s}\,\sin(\omega\, t), \tag{4.1a}$$

$$F_n = F_{n,c}\,\cos(\omega\, t) + F_{n,s}\,\sin(\omega\, t). \tag{4.1b}$$

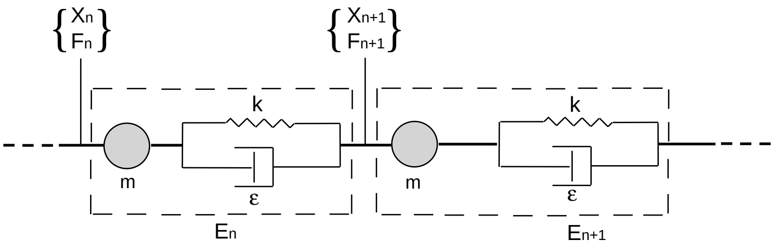

Figure 4.2: Successive elements of the periodic structure.

The governing equations can be written in the following matrix form.

$$\begin{Bmatrix} X_{n+1,c} \\ X_{n+1,s} \\ F_{n+1,c} \\ F_{n+1,s} \end{Bmatrix} = \begin{bmatrix} 1-\dfrac{m\omega^2 k}{\epsilon^2\omega^2+k^2} & \dfrac{m\omega^3\epsilon}{\epsilon^2\omega^2+k^2} & -\dfrac{k}{\epsilon^2\omega^2+k^2} & \dfrac{\epsilon\,\omega}{\epsilon^2\omega^2+k^2} \\ -\dfrac{m\omega^3\epsilon}{\epsilon^2\omega^2+k^2} & 1-\dfrac{m\omega^2 k}{\epsilon^2\omega^2+k^2} & -\dfrac{\epsilon\,\omega}{\epsilon^2\omega^2+k^2} & -\dfrac{k}{\epsilon^2\omega^2+k^2} \\ m\omega^2 & 0 & 1 & 0 \\ 0 & m\omega^2 & 0 & 1 \end{bmatrix} \begin{Bmatrix} X_{n,c} \\ X_{n,s} \\ F_{n,c} \\ F_{n,s} \end{Bmatrix} \tag{4.2}$$

The above equation is of the form

$$\mathbf{q}_{n+1} = \mathbf{T}\mathbf{q}_n. \tag{4.3}$$

By definition, an eigenvalue σ of matrix $\mathbf{T}$ and the associated propagation constant μ are related by

$$\sigma = e^{-\mu}. \tag{4.4}$$

Numerical results showing μ versus ω will be presented later (see Fig. 4.4). First, we develop a small ϵ approximation that will work for the nonlinear case as well.

Eq. (4.2) can also be written as

$$\begin{Bmatrix} X_{n+1,c} \\ X_{n+1,s} \\ F_{n+1,c} \\ F_{n+1,s} \end{Bmatrix} = \begin{bmatrix} 1-\dfrac{m\omega^2}{k} & 0 & -\dfrac{1}{k} & 0 \\ 0 & 1-\dfrac{m\omega^2}{k} & 0 & -\dfrac{1}{k} \\ m\omega^2 & 0 & 1 & 0 \\ 0 & m\omega^2 & 0 & 1 \end{bmatrix} \begin{Bmatrix} X_{n,c} \\ X_{n,s} \\ F_{n,c} \\ F_{n,s} \end{Bmatrix}$$

$$+\epsilon\,\frac{\omega}{k}\left\{\begin{array}{c}\dfrac{m\omega^2X_{n,s}+F_{n,s}}{k}\\ -\dfrac{m\omega^2X_{n,c}+F_{n,c}}{k}\\ 0\\ 0\end{array}\right\}+\mathcal{O}(\epsilon^2). \tag{4.5}$$

Neglecting $\mathcal{O}(\epsilon^2)$ terms, Eq. (4.5) is of the form

$$\mathbf{q}_{n+1} \;=\; \mathbf{B}\mathbf{q}_n+\epsilon\,\mathbf{L}(\mathbf{q}_n). \tag{4.6}$$

4.2.2 Nonlinear damping

We now take the damping force to be $\epsilon(\dot{X}_n-\dot{X}_{n+1})^3$ (cubic nonlinearity). Using Eqs. (4.1), but now in a one-term harmonic balance approximation, we obtain the governing equations in the form

$$\mathbf{q}_{n+1} \;=\; \mathbf{B}\mathbf{q}_n+\epsilon\,\mathbf{N}(\mathbf{q}_n), \tag{4.7}$$

with $\mathbf{B}$ and $\mathbf{q}_n$ the same as in the linear damping case, and with $\mathbf{N}(\mathbf{q}_n)$ given by

$$\mathbf{N}(\mathbf{q}_n) \;=\; \frac{3}{4}(\frac{\omega}{k})^3\left\{(m\omega^2X_{n,c}+F_{n,c})^2+(m\omega^2X_{n,s}+F_{n,s})^2\right\}\left\{\begin{array}{c}\dfrac{m\omega^2X_{n,s}+F_{n,s}}{k}\\ -\dfrac{m\omega^2X_{n,c}+F_{n,c}}{k}\\ 0\\ 0\end{array}\right\}. \tag{4.8}$$

4.3 Method of multiple scales

A method of multiple scales for two-dimensional maps has been presented in, e.g., [28, 40, 41]. For completeness, we briefly present the method for the system

$$\mathbf{q}_{n+1} \;=\; \mathbf{A}\mathbf{q}_n+\epsilon\,\mathbf{N}(\mathbf{q}_n) \tag{4.9}$$

with $0 < \epsilon \ll 1$ and

$$\mathbf{q}_n = \left\{ \begin{array}{c} q_{n,1} \\ \\ q_{n,2} \end{array} \right\}.$$

The method, as used here, assumes that $\mathbf{A}$ has a pair of strictly complex conjugate eigenvalues of unit magnitude. Although Eqs. (4.6) and (4.7) are 4-dimensional maps, the method of analysis is similar.

For our 2-dimensional map, we take

$$\mathbf{A} = \left[\begin{array}{cc} \frac{1}{\sqrt{2}} & \frac{1}{\sqrt{2}} \\ \\ -\frac{1}{\sqrt{2}} & \frac{1}{\sqrt{2}} \end{array} \right], \quad \text{and } \mathbf{N}(\mathbf{q}_n) = \left({q_{n,1}}^2 + {q_{n,2}}^2\right) \left\{ \begin{array}{c} -q_{n,1} - q_{n,2} \\ \\ 2\, q_{n,1} \end{array} \right\}. \tag{4.10}$$

The eigenvalues σ, $\bar{\sigma}$ of $\mathbf{A}$ are

$$\sigma = \frac{1+i}{\sqrt{2}}, \; \bar{\sigma} = \frac{1-i}{\sqrt{2}}.$$

The right eigenvectors ($\mathbf{u}$, $\bar{\mathbf{u}}$) and left eigenvectors ($\boldsymbol{\xi}$, $\bar{\boldsymbol{\xi}}$) correspondng to the eigenvalues σ, $\bar{\sigma}$ are

$$\mathbf{u} = \left\{ \begin{array}{c} u_1 \\ \\ u_2 \end{array} \right\} = \left\{ \begin{array}{c} \frac{1}{\sqrt{2}} \\ \\ \frac{i}{\sqrt{2}} \end{array} \right\}, \; \bar{\mathbf{u}} = \left\{ \begin{array}{c} \bar{u}_1 \\ \\ \bar{u}_2 \end{array} \right\} = \left\{ \begin{array}{c} \frac{1}{\sqrt{2}} \\ \\ -\frac{i}{\sqrt{2}} \end{array} \right\}, \tag{4.11a}$$

$$\boldsymbol{\xi} = \left\{ \begin{array}{cc} \xi_1 & \xi_2 \end{array} \right\} = \left\{ \begin{array}{cc} \frac{1}{\sqrt{2}} & \frac{i}{\sqrt{2}} \end{array} \right\}, \; \bar{\boldsymbol{\xi}} = \left\{ \begin{array}{cc} \bar{\xi}_1 & \bar{\xi}_2 \end{array} \right\} = \left\{ \begin{array}{cc} \frac{1}{\sqrt{2}} & -\frac{i}{\sqrt{2}} \end{array} \right\}. \tag{4.11b}$$

We assume that the solution to Eq. (4.9) depends upon two independent scales, n (fast) and $s = \epsilon n$ (slow). We assume further that the solution can be expanded as [40]:

$$\mathbf{q}_n = \mathbf{Q}(n,s) = \mathbf{Q}_0(n,s) + \epsilon\, \mathbf{Q}_1(n,s) + \mathcal{O}(\epsilon^2) \tag{4.12}$$

$$\mathbf{q}_{n+1} = \mathbf{Q}(n+1, s+\epsilon) = \mathbf{Q}_0(n+1, s+\epsilon) + \epsilon\, \mathbf{Q}_1(n+1, s+\epsilon) + \mathcal{O}(\epsilon^2) \tag{4.13}$$

We also assume that the $\mathbf{Q}$s in Eqs. (4.12) and (4.13) vary smoothly with s. Then (as in [28])

$$\begin{aligned} \mathbf{q}_{n+1} &= \mathbf{Q}(n+1, s+\epsilon) \\ &= \mathbf{Q}_0(n+1, s) + \epsilon\, \left[\mathbf{Q}_1(n+1, s) + \partial_s \mathbf{Q}_0(n+1, s)\right] + \mathcal{O}(\epsilon^2), \end{aligned} \tag{4.14}$$

where ∂_s denotes a partial derivative with respect to s. Substituting Eqs. (4.12) and (4.14) into Eq. (4.9), we obtain

$$\mathbf{Q}_0(n+1, s) + \epsilon \left[\mathbf{Q}_1(n+1, s) + \partial_s \mathbf{Q}_0(n+1, s)\right] =$$

$$\mathbf{A}\mathbf{Q}_0(n,s)+\epsilon\mathbf{A}\mathbf{Q}_1(n,s)+\mathbf{N}(\mathbf{Q}_0(n,s))+\mathcal{O}(\epsilon^2). \tag{4.15}$$

At $\mathcal{O}(1)$:

$$\mathbf{Q}_0(n+1,s) \;=\; \mathbf{A}\,\mathbf{Q}_0(n,s). \tag{4.16}$$

The general solution to Eq. (4.16), for arbitrary n, is

$$\mathbf{Q}_0(n,s) \;=\; \alpha(s)\,\sigma^n\,\mathbf{u}+\bar{\alpha}(s)\,\bar{\sigma}^n\,\bar{\mathbf{u}}, \tag{4.17}$$

where $\alpha(s)$ and $\bar{\alpha}(s)$ are arbitrary, differentiable functions of s. It follows that

$$\partial_s\mathbf{Q}_0(n+1,s) \;=\; \partial_s\alpha\;\sigma^{n+1}\,\mathbf{u}+\partial_s\bar{\alpha}\;\bar{\sigma}^{n+1}\,\bar{\mathbf{u}} \tag{4.18}$$

Using Eq. (4.17), $\mathbf{N}(\mathbf{Q}_0(n,s))$ in Eq. (4.15) will now be written, for arbitrary n, as

$$\mathbf{N}(\mathbf{Q}_0(n,s)) \;=\; \sum_{k=-M}^{M}\mathbf{c}_k\sigma^{k\,n} \tag{4.19}$$

for some finite integer M and appropriate vectors $\mathbf{c}_k$, each independent of σ and $\bar{\sigma}$. With Eqs. (4.18) and (4.19), we then get at $\mathcal{O}(\epsilon)$:

$$\begin{aligned}\mathbf{Q}_1(n+1,s)-\mathbf{A}\mathbf{Q}_1(n,s)=(-\partial_s\alpha\,\sigma\mathbf{u}+\mathbf{c}_1)\sigma^n+(-\partial_s\bar{\alpha}\,\bar{\sigma}\bar{\mathbf{u}}+\mathbf{c}_{-1})\bar{\sigma}^n&\\ +\text{ other powers},&\end{aligned} \tag{4.20}$$

where the ‘other powers’ do not cause resonances and associated secular terms. For the example considered,

$$\mathbf{c_1}=\alpha(s)^2\bar{\alpha}(s)\begin{Bmatrix}-3(\bar{u}_1u_1^2+\bar{u}_2u_2^2)-2(\bar{u}_1+\bar{u}_2)u_1u_2-(u_1^2\bar{u}_2+u_2^2\bar{u}_1)\\ 3u_1^2\bar{u}_1+2u_1u_2\bar{u}_2+\bar{u}_1u_2^2\end{Bmatrix} \tag{4.21}$$

and

$$\mathbf{c_{-1}}=\bar{\mathbf{c}}_\mathbf{1}.$$

To remove the secular terms (which process lies at the heart of the multiple scales method), the coefficient vectors of σ^n and $\bar{\sigma}^n$ should be orthogonal to the left eigenvectors of $\mathbf{A}$ corresponding to the eigenvalues σ and $\bar{\sigma}$ respectively; these two conditions may also be looked upon as solvability conditions that yield the slow evolution sought here. These conditions are

$$-\partial_s\alpha\;\sigma\;\boldsymbol{\xi}\mathbf{u}+\boldsymbol{\xi}\mathbf{c}_1=0, \tag{4.22a}$$

$$-\partial_s \bar{\alpha}\, \bar{\sigma}\, \bar{\boldsymbol{\xi}} \bar{\mathbf{u}} + \bar{\boldsymbol{\xi}} \mathbf{c}_{-1} = 0. \tag{4.22b}$$

From Eqs. (4.11a), (4.21) and (4.22), we obtain

$$\partial_s \alpha = -(2+i)\sqrt{2}\, \bar{\alpha}(s)\, \alpha^2(s), \tag{4.23a}$$

$$\partial_s \bar{\alpha} = -(2-i)\sqrt{2}\, \alpha(s)\, \bar{\alpha}^2(s) \tag{4.23b}$$

Approximating

$$\partial_s \alpha \approx \frac{\alpha(s+\epsilon) - \alpha(s)}{\epsilon} = \frac{\alpha_{n+1} - \alpha_n}{\epsilon},$$

we can convert Eq. (4.23a) into the map:

$$\alpha_{n+1} = \alpha_n - \epsilon(2+i)\sqrt{2}\, \bar{\alpha}_n\, \alpha_n^2. \tag{4.24}$$

For comparison, the oscillatory first component $q_{n,1}$ as obtained from direct numerical solution of the full map with $\epsilon = 0.03$ is plotted in Fig. 4.3. In this case, the initial condition was randomly chosen to be $\mathbf{q_0} = \begin{Bmatrix} 0.8318 \\ 0.5028 \end{Bmatrix}$. The solution for Eq. (4.24) was computed with the corresponding initial condition $\alpha_0 = 0.1648 - 0.6673i$. Note that the amplitude of $q_{n,1}$ is

$$R = \sqrt{2}\, |\alpha_n|. \tag{4.25}$$

The match between R and $q_{n,1}$ is excellent (see Fig. 4.3).

4.4 MMS for the linearly damped periodic structure

Consider Eq. (4.5), written as

$$\mathbf{q}_{n+1} = \mathbf{B}\mathbf{q}_n + \epsilon\, \mathbf{L}(\mathbf{q}_n) \tag{4.26}$$

with $\mathbf{q}_n = \begin{Bmatrix} X_{n,c} & X_{n,s} & F_{n,c} & F_{n,s} \end{Bmatrix}^T$, where T denotes transpose. Here $\mathbf{B}$ is a 4×4 matrix having eigenvalues σ and $\bar{\sigma}$ with multiplicity two each. Taking the parameter values $k = 1$ and $m = 1$, we get

$$\sigma = 1 - \frac{1}{2}\omega^2 + \frac{1}{2}\sqrt{-4\,\omega^2 + \omega^4}.$$

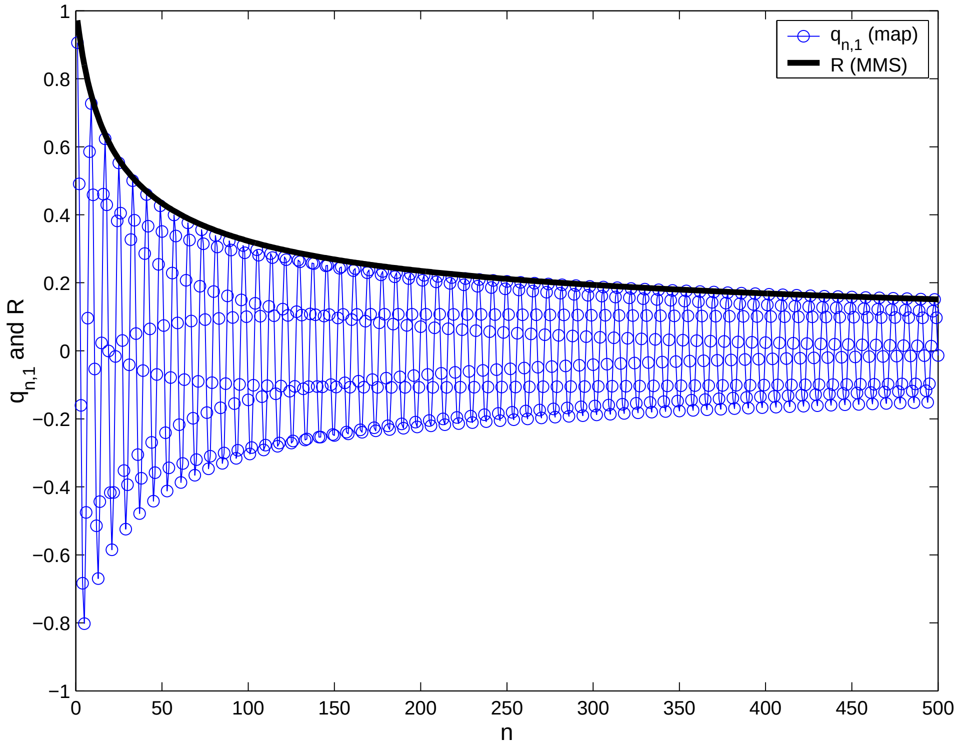

Figure 4.3: Comparison between the numerical solution of Eq. (4.9) and the amplitude obtained by the MMS, Eq. (4.25) for $\epsilon = 0.03$.

The frequency range considered is $0 < \omega < 2$, for which the eigenvalues are strictly complex with unit magnitude. The right eigenvectors are now **u**, **v** with

$$\mathbf{u} = \frac{\omega}{2\sqrt{1+\omega^2}} \left\{ \begin{array}{c} \dfrac{\sqrt{4-\omega^2}}{\omega} i - 1 \\ 0 \\ 2 \\ 0 \end{array} \right\}, \tag{4.27a}$$

$$\mathbf{v} = \frac{\omega}{2\sqrt{1+\omega^2}} \left\{ \begin{array}{c} 0 \\ \\ \dfrac{\sqrt{4-\omega^2}}{\omega} i - 1 \\ \\ 0 \\ \\ 2 \end{array} \right\} \tag{4.27b}$$

and their complex conjugates $\bar{\mathbf{u}}$ and $\bar{\mathbf{v}}$. Similarly, the left eigenvectors are $\boldsymbol{\xi}$, $\boldsymbol{\eta}$ with

$$\boldsymbol{\xi} = \frac{\omega}{2\sqrt{1+\omega^2}} \left\{ \begin{array}{cccc} -\dfrac{i\omega}{2\sqrt{4-\omega^2}} & 0 & \dfrac{\omega}{\sqrt{4-\omega^2}} + i & 0 \end{array} \right\}, \tag{4.28a}$$

$$\boldsymbol{\eta} = \frac{\omega}{2\sqrt{1+\omega^2}} \left\{ \begin{array}{cccc} 0 & -\dfrac{i\omega}{2\sqrt{4-\omega^2}} & 0 & \dfrac{\omega}{\sqrt{4-\omega^2}} + i \end{array} \right\} \tag{4.28b}$$

and their complex conjugates $\bar{\boldsymbol{\xi}}$, $\bar{\boldsymbol{\eta}}$.

As before, we assume

$$\mathbf{q}_n = \mathbf{Q}(n,s) = \mathbf{Q}_0(n,s) + \epsilon\,\mathbf{Q}_1(n,s) + \mathcal{O}(\epsilon^2), \tag{4.29}$$

$$\mathbf{q}_{n+1} = \mathbf{Q}(n+1,s+\epsilon) = \mathbf{Q}_0(n+1,s+\epsilon) + \epsilon\,\mathbf{Q}_1(n+1,s+\epsilon) + \mathcal{O}(\epsilon^2). \tag{4.30}$$

Substituting Eqs. (4.29) and (4.30) into Eq. (4.26) and collecting terms at $\mathcal{O}(1)$ gives

$$\mathbf{Q}_0(n+1,s) = \mathbf{B}\,\mathbf{Q}_0(n,s), \tag{4.31}$$

the solution to which is

$$\mathbf{Q}_0(n,s) = (\alpha(s)\mathbf{u} + \gamma(s)\mathbf{v})\,\sigma^n + (\bar{\alpha}(s)\bar{\mathbf{u}} + \bar{\gamma}(s)\bar{\mathbf{v}})\,\bar{\sigma}^n, \tag{4.32}$$

where $\alpha(s)$, $\gamma(s)$ are arbitrary, differentiable functions of s. Using Eq. (4.32), $\mathbf{L}(\mathbf{Q}_0(n,s))$ can be written as (see Eq. (4.19); here $M = 1$)

$$\mathbf{L}(\mathbf{Q}_0(n,s)) = \mathbf{c}_1\sigma^n + \mathbf{c}_{-1}\bar{\sigma}^n, \tag{4.33}$$

$$\mathbf{c}_1 = \left\{ \begin{array}{c} -\omega^3\,(\alpha(s)u_2 + \gamma(s)v_2) - \omega\,\left(\alpha(s)u_4 + \gamma(s)v_4\right) \\ \\ \omega^3\,(\alpha(s)u_1 + \gamma(s)v_1) + \omega\,\left(\alpha(s)u_3 + \gamma(s)v_3\right) \\ \\ 0 \\ \\ 0 \end{array} \right\}, \text{ and } \mathbf{c}_{-1} = \bar{\mathbf{c}}_1, \tag{4.34}$$

where u_i's and v_i's are components of $\mathbf{u}$ and $\mathbf{v}$ given by Eqs. (4.27). Eliminating the secular terms,

$$\boldsymbol{\xi}(-\partial_s\alpha\,\sigma\mathbf{u} - \partial_s\gamma\,\sigma\mathbf{v} + \mathbf{c}_1) = 0, \tag{4.35a}$$

$$\boldsymbol{\eta}(-\partial_s\alpha\,\sigma\mathbf{u} - \partial_s\gamma\,\sigma\mathbf{v} + \mathbf{c}_1) = 0, \tag{4.35b}$$

$$\bar{\boldsymbol{\xi}}(-\partial_s\bar{\alpha}\,\bar{\sigma}\bar{\mathbf{u}} - \partial_s\bar{\gamma}\,\bar{\sigma}\bar{\mathbf{v}} + \mathbf{c}_{-1}) = 0, \tag{4.35c}$$

$$\bar{\boldsymbol{\eta}}(-\partial_s\bar{\alpha}\,\bar{\sigma}\bar{\mathbf{u}} - \partial_s\bar{\gamma}\,\bar{\sigma}\bar{\mathbf{v}} + \mathbf{c}_{-1}) = 0, \tag{4.35d}$$

from which the slow evolution obtained is

$$\partial_s\alpha = \frac{i\omega^2}{\sqrt{4-\omega^2}}\gamma(s), \tag{4.36a}$$

$$\partial_s\bar{\alpha} = -\frac{i\omega^2}{\sqrt{4-\omega^2}}\bar{\gamma}(s), \tag{4.36b}$$

$$\partial_s\gamma = -\frac{i\omega^2}{\sqrt{4-\omega^2}}\alpha(s), \tag{4.36c}$$

$$\partial_s\bar{\gamma} = \frac{i\omega^2}{\sqrt{4-\omega^2}}\bar{\alpha}(s). \tag{4.36d}$$

Now let

$$\alpha(s) = a(s) + i\,b(s) \tag{4.37a}$$

$$\gamma(s) = c(s) + i\,d(s) \tag{4.37b}$$

with a, b, c, d real functions of s. Then,

$$\partial_s\alpha = \partial_s a + i\partial_s b,$$

$$\partial_s\gamma = \partial_s c + i\partial_s d.$$

Substituting Eqs. (4.37) into Eqs. (4.36) for $0 < \omega < 2$, we obtain

$$\partial_s a = -\frac{\omega^2}{\sqrt{4-\omega^2}}d(s), \tag{4.38a}$$

$$\partial_s b = \frac{\omega^2}{\sqrt{4-\omega^2}}c(s), \tag{4.38b}$$

$$\partial_s c = \frac{\omega^2}{\sqrt{4-\omega^2}}b(s), \tag{4.38c}$$

$$\partial_s d = -\frac{\omega^2}{\sqrt{4-\omega^2}}a(s). \tag{4.38d}$$

Eqs. (4.38) have a four dimensional phase space. Starting from random initial conditions, trajectories are observed to go to infinity as $s \to \pm\infty$. The growing solution for $s \to -\infty$ represents a decaying wave as $s \to \infty$, and vice versa. We expect two 2-dimensional invariant subspaces, one containing solutions growing as $s \to +\infty$ (unstable subspace) and the other containing solutions growing as $s \to -\infty$ (stable subspace).

The invariant subspaces can be obtained as follows. Putting $d = -a$ and $c = b$ in Eqs. (4.38), we obtain

$$\partial_s a = \frac{\omega^2}{\sqrt{4-\omega^2}} a(s), \tag{4.39a}$$

$$\partial_s b = \frac{\omega^2}{\sqrt{4-\omega^2}} b(s), \tag{4.39b}$$

which shows exponential growth as $s \to +\infty$. This gives the unstable subspace. Similarly putting $d = a$ and $c = -b$, we obtain

$$\partial_s a = -\frac{\omega^2}{\sqrt{4-\omega^2}} a(s), \tag{4.40a}$$

$$\partial_s b = -\frac{\omega^2}{\sqrt{4-\omega^2}} b(s), \tag{4.40b}$$

which shows exponential growth as $s \to -\infty$. This gives the stable subspace.

For any arbitrary solution not necessarily restricted to the invariant subspace, the amplitude is given by

$$R(s) \;=\; \sqrt{X_{n,c}^2 + X_{n,s}^2} = 2|\alpha(s)u_1 + \gamma(s)v_1|. \tag{4.41}$$

From Eqs. (4.27),

$$u_1 = \frac{\sqrt{4-\omega^2}\; i - \omega}{2\sqrt{1+\omega^2}}, \qquad v_1 = 0.$$

This gives

$$R(s) = 2|u_1|\sqrt{a^2(s) + b^2(s)}. \tag{4.42}$$

In particular, restricting attention to the stable subspace,

$$\partial_s R \;=\; -\frac{\omega^2}{\sqrt{4-\omega^2}} R(s), \tag{4.43}$$

which gives

$$R = e^{-\epsilon \frac{\omega^2}{\sqrt{4-\omega^2}} n} R_0, \tag{4.44}$$

for some initial amplitude R_0. The attenuation constant is given by

$$Re(\mu) = \frac{\omega^2}{\sqrt{4-\omega^2}} \epsilon, \quad \text{for } 0 < \omega < 2. \tag{4.45}$$

The attenuation constant obtained from Eq. (4.4) is compared with that obtained from the above equation in Fig. 4.4. The match is excellent for ω not very close to 2.

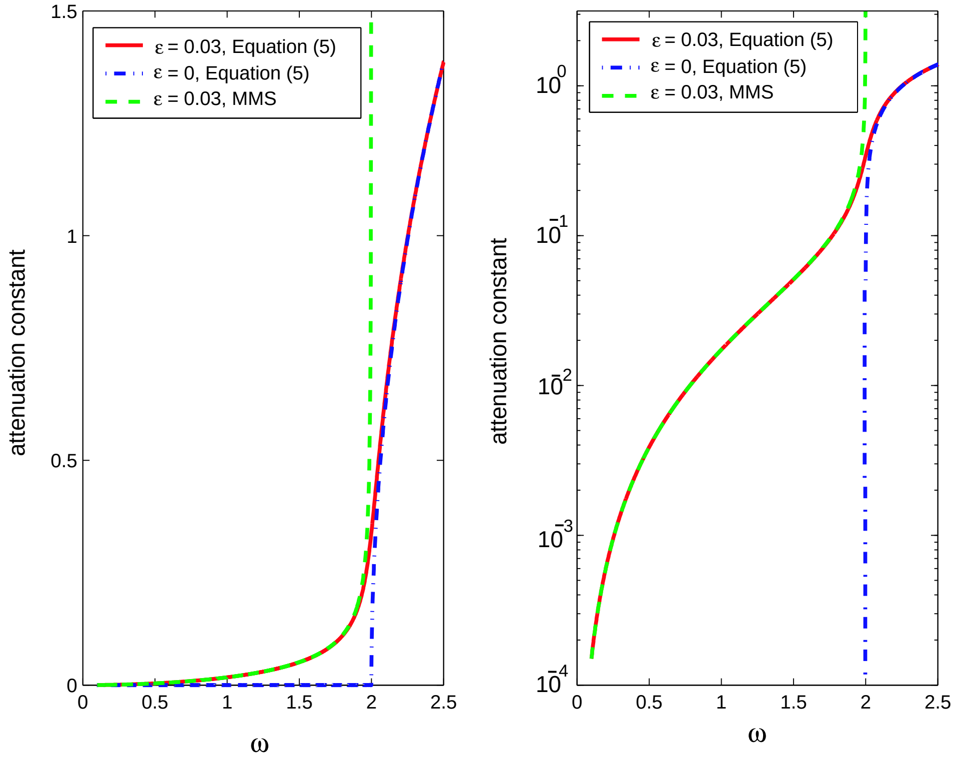

Figure 4.4: For the linear structure without damping, the propagation zone (PZ) is $0 < \omega < 2$. With linear damping ($\epsilon = 0.03$), the attenuation constants obtained by Eq. (4.4) and by multiple scales (Eq. (4.45)) match well.

4.5 MMS for the nonlinearly damped periodic structure

We now consider the weakly and nonlinearly damped periodic structure given by Eq. (4.7)

$$\mathbf{q}_{n+1} = \mathbf{B}\,\mathbf{q}_n + \epsilon\,\mathbf{N}(\mathbf{q}_n).$$

Applying the MMS as described above, we obtain the following expressions for the slow evolution:

$$\partial_s \alpha = i\,C(\omega)(3\,\gamma^2\bar{\gamma} + 2\,\alpha\bar{\alpha}\gamma + \alpha^2\bar{\gamma}), \tag{4.46a}$$

$$\partial_s \bar{\alpha} = -i\,C(\omega)(3\,\gamma\bar{\gamma}^2 + 2\,\alpha\bar{\alpha}\bar{\gamma} + \bar{\alpha}^2\gamma), \tag{4.46b}$$

$$\partial_s \gamma = -i\,C(\omega)(3\,\alpha^2\bar{\alpha} + 2\,\alpha\bar{\gamma}\gamma + \gamma^2\bar{\alpha}), \tag{4.46c}$$

$$\partial_s \bar{\gamma} = i\,C(\omega)(3\,\alpha\bar{\alpha}^2 + 2\,\bar{\alpha}\bar{\gamma}\gamma + \bar{\gamma}^2\alpha), \tag{4.46d}$$

where $C(\omega)$, a positive real number for $0 < \omega < 2$ (see Fig. 4.5), is given by

$$C(\omega) = -\frac{3}{4}\,i\frac{\omega^5}{(\omega^4 - 3\omega^2 - 4)}\,\frac{(\omega^4 - 4\omega^2 + i\omega\sqrt{4-\omega^2}(2-\omega^2))}{(\omega^2 - i\omega\sqrt{4-\omega^2} - 2)}. \tag{4.47}$$

Again putting

$$\alpha(s) = a(s) + i\,b(s)$$

$$\gamma(s) = c(s) + i\,d(s)$$

in Eqs. (4.46), we obtain

$$\partial_s a = -C(\omega)\,\left(3d(\frac{a^2}{3} + b^2 + c^2 + d^2) + 2abc\right), \tag{4.48a}$$

$$\partial_s b = C(\omega)\,\left(3c(a^2 + \frac{b^2}{3} + c^2 + d^2) + 2abd\right), \tag{4.48b}$$

$$\partial_s c = C(\omega)\,\left(3b(a^2 + b^2 + \frac{c^2}{3} + d^2) + 2acd\right), \tag{4.48c}$$

$$\partial_s d = -C(\omega)\,\left(3a(a^2 + b^2 + c^2 + \frac{d^2}{3}) + 2bcd\right). \tag{4.48d}$$

Eqs. (4.48) have a 4-dimensional phase space. As for the linearly damped case, stable and unstable invariant manifolds can be easily found for this case as well (details omitted).

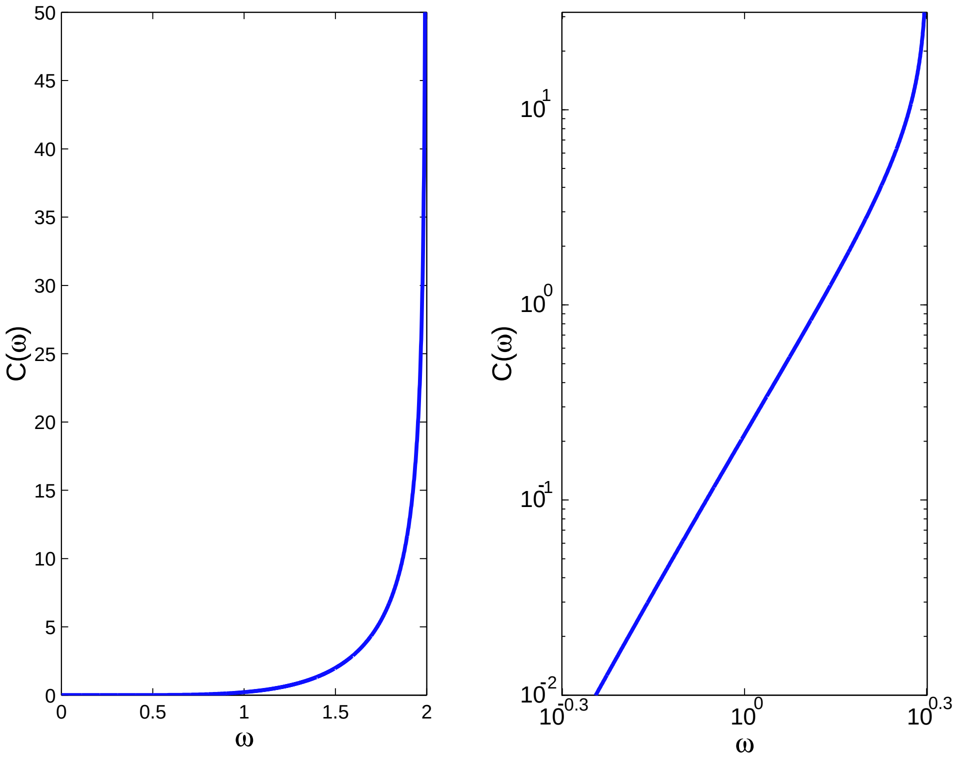

Figure 4.5: $C(\omega)$ for $0 < \omega < 2$.

For numerical simulation, as shown in Fig. 4.6, an N-mass periodic structure with fixed-free end conditions is used. The first mass is excited sinusoidally. The equations of motion are as follows. For the first mass,

$$m\ddot{X}_1 = k\left(X_2 - 2\,X_1\right) + \epsilon\left(\dot{X}_2 - \dot{X}_1\right)^r + F\sin\left(\omega\,t\right), \tag{4.49a}$$

where $r = 1$ for linear damping and $r = 3$ for nonlinear (cubic) damping. For $n = 2$ to $N-1$,

$$m\ddot{X}_n = k\left(X_{n+1} + X_{n-1} - 2\,X_n\right) + \epsilon\left\{\left(\dot{X}_{n+1} - \dot{X}_n\right)^r - \left(\dot{X}_n - \dot{X}_{n-1}\right)^r\right\}. \tag{4.49b}$$

For the last mass,

$$m\ddot{X}_N = k\left(X_{N-1} - X_N\right) - \epsilon\left(\dot{X}_N - \dot{X}_{N-1}\right)^r. \tag{4.49c}$$

Parameter values used in the simulation are $\omega = \dfrac{4}{5}$, $\epsilon = 0.01$, $k = 1$ and $m = 1$. We use $F = 2$ for $N = 1000$ and $F = 5$ for $N = 300$.

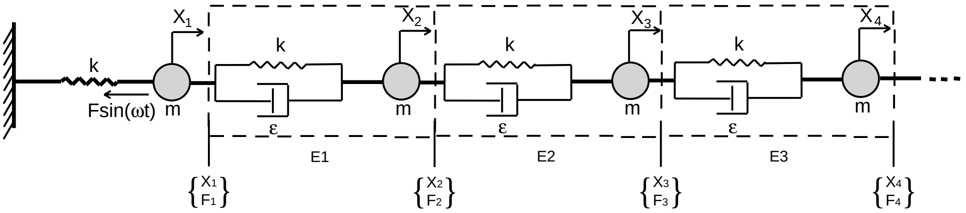

Figure 4.6: Periodic structure with the fixed-free end conditions and the first mass excited.

4.5.1 Linear damping

Eqs. (4.49) can be cast in the following matrix form

$$\mathbf{M}\ddot{\mathbf{X}} + \mathbf{C}\dot{\mathbf{X}} + \mathbf{K}\mathbf{X} = \mathbf{u}\sin(\omega t), \tag{4.50}$$

where $\mathbf{X} = \{X_1\ X_2\ \cdots\ X_N\}^T$, $\mathbf{u} = \{F\ 0\ \cdots\ 0\}^T$, $\mathbf{M}, \mathbf{C}, \mathbf{K}$ are the mass matrix, the damping matrix and the stiffness matrix respectively. After transients die out, the solution $\mathbf{X}$ oscillates with the forcing frequency ω. Assuming $\mathbf{X} = \mathbf{a}\sin(\omega t) + \mathbf{b}\cos(\omega t)$, we solve for $\mathbf{a}$ and $\mathbf{b}$ in terms of $\mathbf{M}$, $\mathbf{C}$, $\mathbf{K}$, $\mathbf{u}$ and ω. Figure 4.7 shows the positions of masses in the steady state solution at time $t = \dfrac{\pi}{2\omega}$. Displacements and velocities of the first two masses in the steady state are

$$X_1 = 1.3611,\ X_2 = -0.153,\ \dot{X}_1 = 1.177,\ \dot{X}_2 = 1.591.$$

Substituting the above in the RHS of Eq. (4.1a) and at $\omega t = \dfrac{\pi}{2}$, we get

$$X_{1,c} = -1.4712,\ X_{1,s} = 1.3611,\ X_{2,c} = -1.9887,\ X_{2,s} = -0.153.$$

As seen from Fig. 4.6, we have

$$F_1 = k(X_2 - X_1) + \epsilon(\dot{X}_2 - \dot{X}_1). \tag{4.51}$$

Using Eqs. (4.1), we get

$$\begin{aligned} F_{1,c} &= k(X_{2,c} - X_{1,c}) + \epsilon\,\omega(X_{2,s} - X_{1,s}), \\ F_{1,s} &= k(X_{2,s} - X_{1,s}) + \epsilon\,\omega(X_{2,c} - X_{1,c}) \end{aligned}$$

and substituting numerical values from the above, we get

$$F_{1,c} = -0.5296,\ F_{1,s} = -1.5099.$$

Now we rewrite Eq. (4.32) for $n = 1$ in the following manner.

$$\left\{\begin{array}{c} X_{1,c} \\ \\ X_{1,s} \\ \\ F_{1,c} \\ \\ F_{1,s} \end{array}\right\} = (a_1 + ib_1)\left\{\begin{array}{c} u_1 \\ \\ u_2 \\ \\ u_3 \\ \\ u_4 \end{array}\right\}\sigma + (c_1 + id_1)\left\{\begin{array}{c} v_1 \\ \\ v_2 \\ \\ v_3 \\ \\ v_4 \end{array}\right\}\sigma + c.c.,$$

where *c.c.* denotes complex conjugate of the two terms written. Vectors $\mathbf{u}$ and $\mathbf{v}$ are given by Eqs. (4.27). Solving above equation for a_1, b_1, c_1, d_1, we get

$$a_1 = 0.601,\ b_1 = 1.1355,\ c_1 = -1.1323,\ d_1 = 0.5981.$$

For the MMS results, recall Eqs. (4.38). Writing

$$\partial_s a \approx \frac{a(s+\epsilon) - a(s)}{\epsilon} = \frac{a_{n+1} - a_n}{\epsilon},$$

$$\partial_s b \approx \frac{b(s+\epsilon) - b(s)}{\epsilon} = \frac{b_{n+1} - b_n}{\epsilon}$$

and likewise for $\partial_s c$ and $\partial_s d$, we convert Eqs. (4.38) into the map

$$\left\{\begin{array}{c} a_{n+1} \\ \\ b_{n+1} \\ \\ c_{n+1} \\ \\ d_{n+1} \end{array}\right\} = \left\{\begin{array}{c} a_n \\ \\ b_n \\ \\ c_n \\ \\ d_n \end{array}\right\} - \epsilon\,\frac{\omega^2}{\sqrt{4-\omega^2}}\left\{\begin{array}{c} d_n \\ \\ c_n \\ \\ b_n \\ \\ a_n \end{array}\right\}. \tag{4.52}$$

We solve Eq. (4.52) with the above obtained initial condition. The amplitude is given by (see Eq. (4.42))

$$R = 2\,|u_1|\sqrt{a_n^2 + b_n^2}.$$

The match as seen from Fig. 4.7 is excellent.

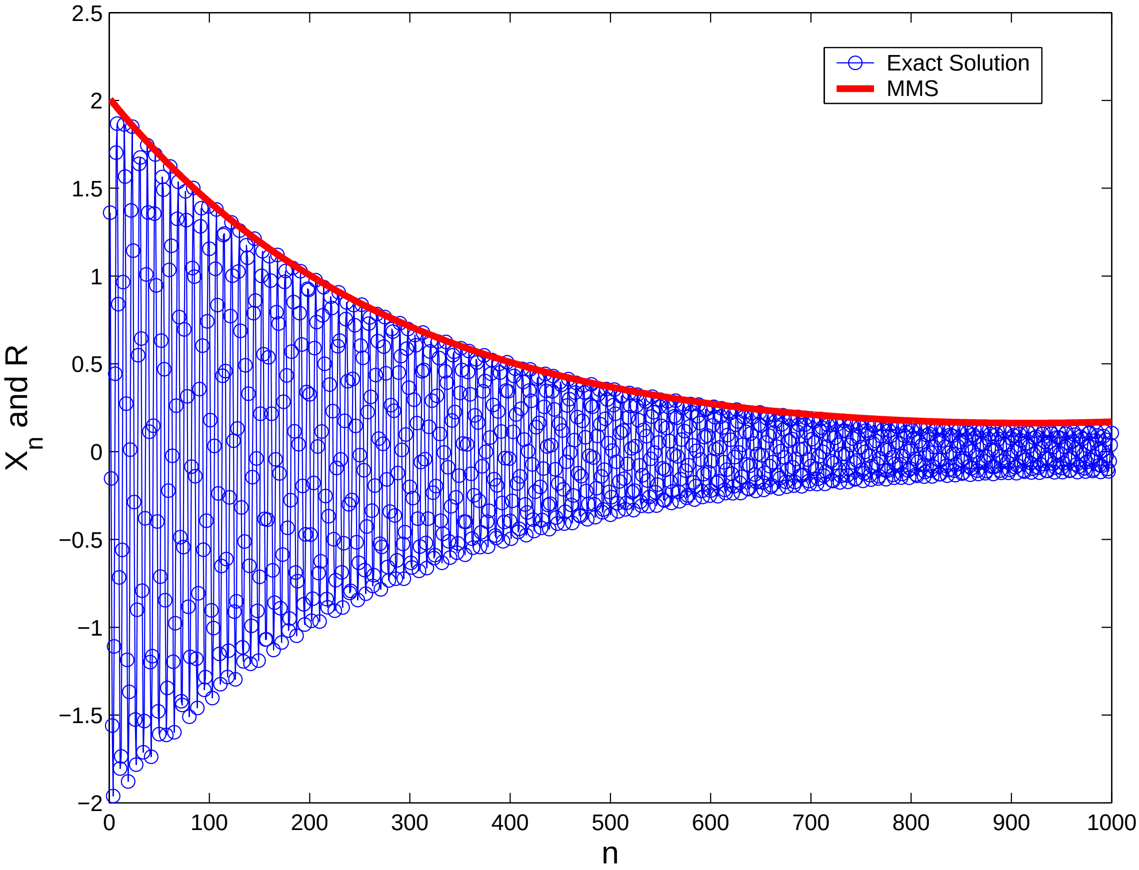

Figure 4.7: Linear Damping: $N = 1000,\ \epsilon = 0.01,\ F = 2$ and $\omega = \frac{4}{5}$

4.5.2 Nonlinear damping

For the nonlinear structure ($r = 3$), a closed form solution for the steady state response is not sought here. Eqs. (4.49) are first integrated numerically using MATLAB's ODE solver (ode45) for some fixed and large number of forcing cycles (here, 5000). This gets rid of initial transients to a large extent, though not completely. The end conditions obtained are used as an initial guess for iterative numerical refinement as follows.

Given an initial guess for the steady state, we integrate for one forcing cycle with high numerical accuracy (in Matlab, the error tolerances were set at 10^{-13}). The difference between the end condition obtained and the initial guess is to be iteratively taken towards zero. The best known iterative technique is the Newton-Raphson method in which, to seek a zero of $\mathbf{g}(\mathbf{q})$, we let

$$\mathbf{q}_{k+1} = \mathbf{q}_k - [D\mathbf{g}]^{-1}_{\mathbf{q}_k}\, \mathbf{g}(\mathbf{q}_k),$$

where $[D\mathbf{g}]_{\mathbf{q}_k}$ is the Jacobian of $\mathbf{g}$ evaluated at $\mathbf{q}_k$. For arbitrary N-dimensional vector functions of N-dimensional vectors, the Jacobian can be numerically approximated using finite differences, and requires $N+1$ function evaluations (expensive for large N). To speed things up, we can repeatedly use $[D\mathbf{g}]_{\mathbf{q}_0}$ in place of finding $[D\mathbf{g}]_{\mathbf{q}_k}$ each time. The method will still work if the initial guess is good enough; and though a few more iterations may be needed, the total number of function evaluations needed can be much smaller if N is large.

The steady state solutions obtained using the above method are plotted in Fig. 4.8 for $N = 1000$ and in Fig. 4.9 for $N = 300$. In Fig. 4.8, the match is not nearly as good as in the linear damping case; but it is quite good for Fig. 4.9. This will be discussed below.

To generate the above numerical comparison, we initially proceed exactly as for the linear case. Eq. (4.48), after converting into a map, gives

$$\begin{Bmatrix} a_{n+1} \\ b_{n+1} \\ c_{n+1} \\ d_{n+1} \end{Bmatrix} = \begin{Bmatrix} a_n \\ b_n \\ c_n \\ d_n \end{Bmatrix} - 4\,\epsilon\, C(\omega) \begin{Bmatrix} 3\,d_n \left(\frac{1}{3}\,{a_n}^2 + {b_n}^2 + {c_n}^2 + {d_n}^2\right) + 2\,a_n b_n c_n \\ -3\,c_n \left({a_n}^2 + \frac{1}{3}\,{b_n}^2 + {c_n}^2 + {d_n}^2\right) + 2\,a_n b_n d_n \\ 3\,b_n \left({a_n}^2 + {b_n}^2 + \frac{1}{3}\,{c_n}^2 + {d_n}^2\right) + 2\,a_n c_n d_n \\ 3\,a_n \left({a_n}^2 + {b_n}^2 + {c_n}^2 + \frac{1}{3}\,{d_n}^2\right) + 2\,b_n c_n d_n \end{Bmatrix}. \quad (4.53)$$

It remains to iteratively evaluate the map starting from some suitable initial conditions.

We recall that in the MMS, we expand the unknown as

$$\mathbf{q} = \mathbf{Q}_0 + \epsilon \mathbf{Q}_1 + \cdots\,,$$

and the MMS then gives the evolution of $\mathbf{Q}_0$. The initial conditions for $\mathbf{Q}_0$ can differ by $\mathcal{O}(\epsilon)$ from those for $\mathbf{q}$. Keeping this in mind, we used a small, ad hoc, optimization procedure to seek initial conditions for $\mathbf{Q}_0$ that tried to simultaneously keep two things small: (1) the difference between the assumed initial conditions for $\mathbf{Q}_0$ and the numerically obtained initial conditions for $\mathbf{q}$ (see discussion of the linearly damped case), and (2) the difference between the computed final state of $\mathbf{Q}_0$ for the last mass, and the numerically obtained corresponding state $\mathbf{q}$ (this was not done for the linearly damped case).

Note that the details of the optimization procedure and the objective function used[1] are not important for the theory. This is because the MMS tries to find a slow evolution equation whose solutions stay close to the actual solution over n-scales of $\mathcal{O}(1/\epsilon)$, but which do not necessarily match initial conditions.

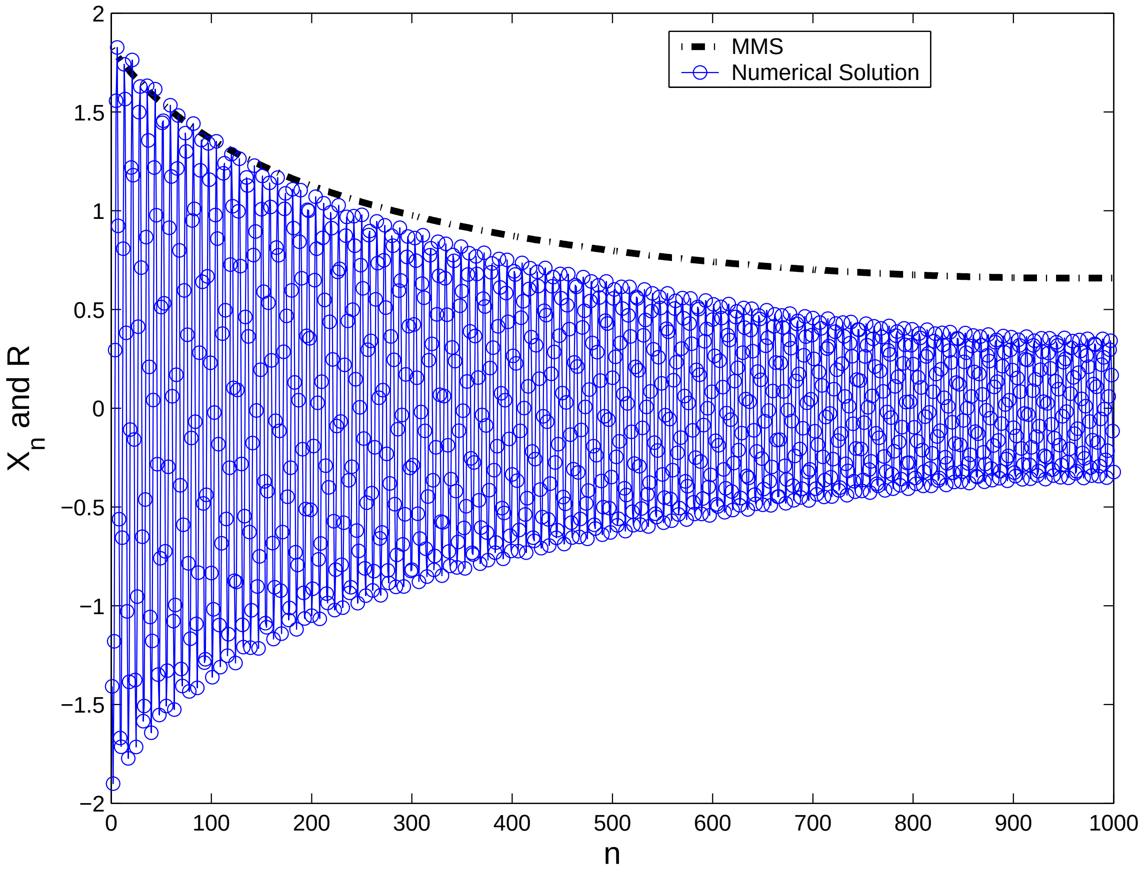

Figure 4.8: Nonlinear Damping: $N = 1000,\ \epsilon = 0.01,\ F = 2$, and $\omega = \frac{4}{5}$

The initial guesses provided by the above procedure, and used to generate the figures, are

$$a_1 = 1.7690,\ b_1 = 2.7321,\ c_1 = -2.5855,\ d_1 = 1.8218$$

for $N = 300$ and

$$a_1 = -1.2164,\ b_1 = 0.3697,\ c_1 = -0.1679,\ d_1 = -1.2442$$

---

[1] We used a weighted sum of the two difference magnitudes (norms).

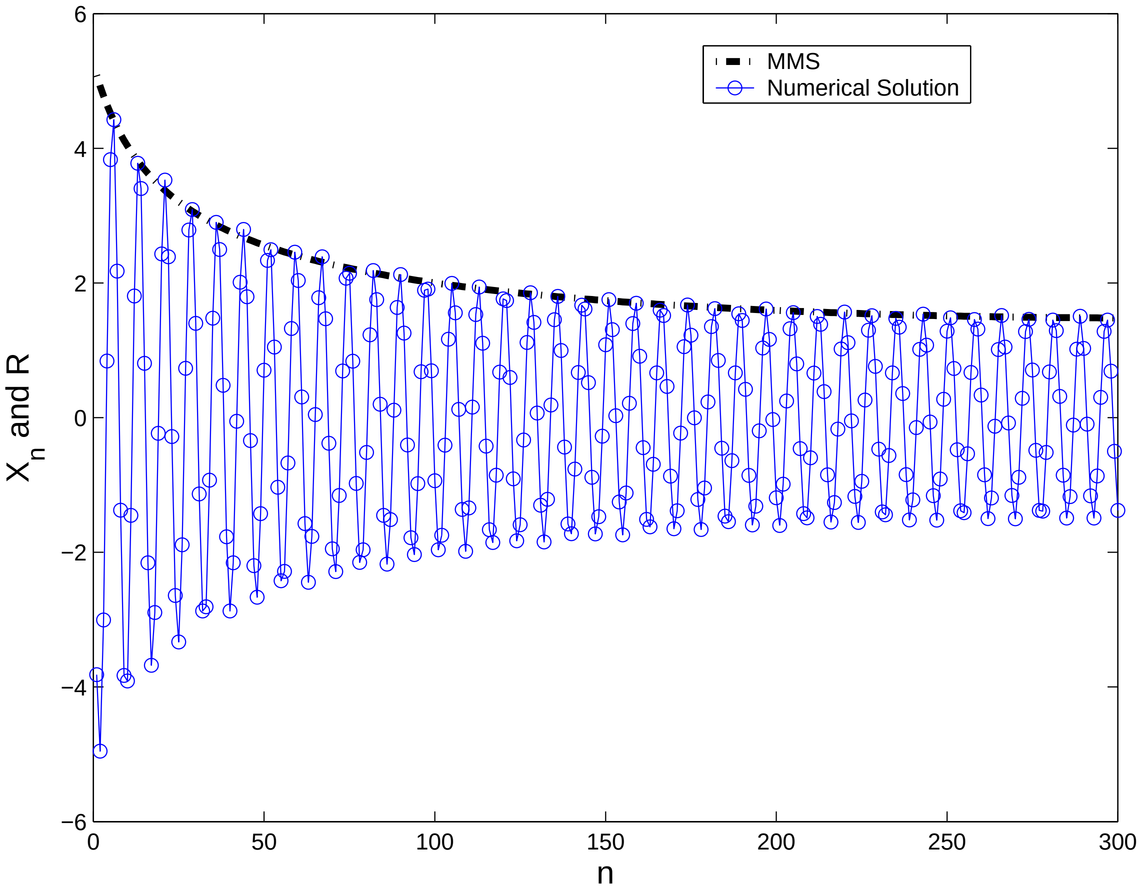

Figure 4.9: Nonlinear Damping: $N = 300,\ \epsilon = 0.01,\ F = 5$, and $\omega = \frac{4}{5}$

for $N = 1000$.

The above results show that for the nonlinear damping case, the MMS does not accurately predict the attenuation over very large numbers of periods of the structure. This should not, however, be viewed as a failure of the method. The basic theorems on the MMS guarantee validity over time scales (or, more appropriately here, n-scales) of $\mathcal{O}(1/\epsilon)$. Occasionally, as was observed for the linearly damped case, good agreement is obtained over much longer time scales. However, noting that we used $\epsilon = 0.01$, we expect good agreement over a few hundred periods of the structure but are not surprised if agreement becomes poor over a thousand periods.

4.6 Conclusions

We have studied harmonic wave attenuation in periodic structures with weak damping (both linear and nonlinear). The damping strength was governed by a small parameter ϵ. The problem was studied using maps which were slightly perturbed versions of simpler maps which had a pair of pure imaginary eigenvalues. These maps were analyzed using the method of multiple scales (MMS), which has so far not been used for such problems. Good agreement between the MMS approximation and full numerics was observed for both cases, when the number of periods of the structure was $\mathcal{O}(1/\epsilon)$. For the linear damping case, agreement was in fact good for even greater numbers of periods; this is consistent with the fact that the estimate of the attenuation constant, which can be analytically obtained for the linearly damped case, was also very good.

Chapter 5

A strongly nonlinear parametrically kicked oscillator

In this thesis, until now, we have studied three systems that are parametrically forced. In all the three, the parameters vary in a continuous fashion with the independent variable. In this chapter, we look at a system where the parameter varies in a discontinuous fashion. Here, we study the dynamic response of a strongly nonlinear (cubic nonlinearity) single-degree-of-freedom oscillator under a constant amplitude, parametric, periodic, impulsive forcing: for example, a pendulum with a strongly nonlinear torsion spring, that is periodically struck in the axial direction. We assume a 1-term harmonic balance oscillation between successive kicks. Requiring the displacement to be continuous and using a finite jump, proportional to the displacement, in the velocity across the kick, an explicit 2-dimensional map is obtained with amplitude and phase as variables. We study the dynamics of the approximating map, not of the original pendulum system. A Poincaré section plot shows chaos. Fixed points of the map are studied numerically along with their stability properties. Stable and unstable manifolds of different period-orbits of the unstable type are computed with the help of lately available software [42]. Transverse intersections of the stable and unstable manifolds confirm the presence of chaos in the system.

5.1 Introduction

Kicked rotors and oscillators have been studied for the last 50 years [43, 44, 45]. A simple model of a kicked oscillator is

$$\ddot{x} + \xi \dot{x} + x = P f(x) \sum_{n=1}^{\infty} \delta(t - nT), \tag{5.1}$$

where x is a non-dimensional displacement. Here we model impulsive forcing using δ, the Dirac delta function, which is zero everywhere except at $t = nT$. P is assumed to be constant. $f(x)$ is an arbitrary function of x. This system is non-autonomous. When $f(x) =$ constant, the forcing is external; otherwise, it is parametric. Forcing is periodic with period T, the time between successive kicks.

Rasband [44] discusses Eq. (5.1) with $\xi = 0$. He shows that, for $f(x) = 1$ or x, the resulting system is not chaotic; and for chaos to be present, nonlinearity is essential. He explains the resonance phenomenon for $f(x) = 1$ when $T = 2\pi$, i.e., the time between successive kicks is exactly equal to the natural period of the oscillator. He also discusses the case $f(x) = x^4$, where the system shows chaotic behaviour. The Poincaré section shows chains of several periodic islands (alternate stable and unstable fixed points). Also, he observes around the outer edges of the island chain a small but finite layer of chaotic orbits.

Moon [45] discusses a rotor with rotary inertia J and damping c subjected to a steady torque and a periodic series of pulsed (variable amplitude) torques with period τ. The change in angular momentum is given by

$$J\dot{\omega} + c\,\omega = c\,\omega_0 + T(\theta) \sum_{n=-\infty}^{\infty} \delta(t - n\tau). \tag{5.2}$$

The angular momentum change across the pulse is given by

$$J(\omega_+ - \omega_-) = T(\theta(n\tau)).$$

The Poincaré map is obtained by taking the section just before each pulsed torque, solving the linear differential equation between pulses, and using the jump in angular momentum condition across the pulse.

Pratap *et al.* [46] study a kicked elastoplastic oscillator which they model with direct as well as parametric, periodic, constant amplitude, impulsive forcing. They study bifurcations in the forcing parameter plane (P-T) as well as stability of different types of motion using eigenvalues of the linearized Poincaré map. Pratap and Holmes [47] study the global dynamics of the Poincaré map for the same system, give existence and stability conditions for periodic orbits and prove existence of chaos at specific, but representative, parameter values where the system is within the elastic range. The present work is most closely related to [47], with the distinctions that we study a strongly nonlinear oscillator, that we approximate its dynamics using harmonic balance, and that we numerically (as opposed to analytically) compute stable and unstable manifolds of various periodic orbits.

In this chapter, we study a strongly nonlinear parametrically forced oscillator

$$\ddot{x} + x^3 = P f(x) \sum_{n=1}^{\infty} \delta(t - nT), \tag{5.3}$$

with $f(x) = x$. For construction of the map, we require solution of the differential equation governing the motion between the kicks. We assume, for simplicity, a 1-term harmonic balance approximation for it. Note that elliptic functions could also be used, but we avoid them for simplicity. Our study is numerical, and we find the system to be chaotic for $P = 1$. For small values of P the system is not chaotic.

5.2 Construction of the approximating map

It is emphasized at the outset that we use a harmonic balance approximation in constructing the map. All further discussion will be of this map, and not of the original system. The system may therefore be viewed as merely motivating the study of this map.

Consider a pendulum with a strongly nonlinear torsion spring at the pivot as shown in Fig. 5.1. Force $F(t)$ acts in the y-direction. The motion of the pendulum, choosing mass and length to be unity, is governed by

$$\ddot{\theta} + k\,\theta^3 = F(t)\sin\theta, \tag{5.4}$$

where the stiffness of the torsion spring k is taken as large. Letting $k\,\theta^3 = x^3$ so x can be

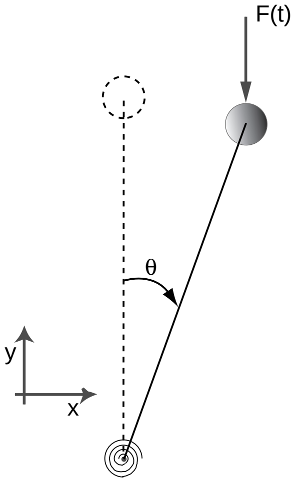

Figure 5.1: Inverted pendulum with strongly nonlinear torsion spring forced vertically.

large even though θ is small, and approximating $\sin\theta \approx \theta$, we get the equation for x as

$$\ddot{x} + x^3 = xF(t), \tag{5.5}$$

where a scaling constant has been absorbed into F.

Our study in this chapter is concerned with Eq. (5.5) instead of Eq. (5.4). Since the effect of forcing depends upon the instantaneous position $x(t)$, the forcing is parametric. We consider an impulsive forcing $F(t) = P\sum_{n=1}^{\infty}\delta(t - nT)$, with a constant amplitude P and period T. The position of the pendulum is continuous across the impulse, and there is a finite jump in velocity proportional to the displacement at the instant of the impulse, i.e.,

$$x_+ = x_-, \tag{5.6}$$

$$\dot{x}_+ - \dot{x}_- = Px_-. \tag{5.7}$$

In between two successive kicks, position and velocity are governed by

$$\ddot{x} + x^3 = 0. \tag{5.8}$$

We assume a 1-term harmonic balance solution to Eq. (5.8)

$$x(t) = A_k\,\sin(cA_k(t + \phi_k)) \tag{5.9}$$

for $0 \leq t \leq T$, where $c = \dfrac{\sqrt{3}}{2}$ from a routine calculation. We also take

$$\dot{x}(t) = c\, A_k^2 \, \cos(cA_k(t + \phi_k)). \tag{5.10}$$

At the beginning of the next interval we reset time to 0. Assuming again the 1-term harmonic balance solution, we have

$$x(t) = A_{k+1} \, \sin(cA_{k+1} \, (t + \phi_{k+1})), \tag{5.11}$$

$$\dot{x}(t) = c\, A_{k+1}^2 \, \cos(cA_{k+1} \, (t + \phi_{k+1})). \tag{5.12}$$

with $0 \leq t \leq T$. We substitute $t = T$ in Eqs. (5.9) and (5.10) to get position and velocity just before the impulse, i.e., x_- and $\dot{x}_-$; and we substitute $t = 0$ in Eqs. (5.11) and (5.12) to get position and velocity just after the impulse, i.e., x_+ and $\dot{x}_+$. From Eqs. (5.6) and (5.7), we then obtain the explicit map

$$A_{k+1} = \sqrt{\frac{f_1^2}{2} + \sqrt{\frac{f_1^4}{4} + \frac{f_2^2}{c^2}}} \tag{5.13}$$

$$\phi_{k+1} = \frac{1}{cA_{k+1}} \, \arctan(cA_{k+1} \, \frac{f_1}{f_2}), \tag{5.14}$$

where

$$f_1 = A_k \, \sin(cA_k(T + \phi_k)), \tag{5.15}$$

$$f_2 = cA_k^2 \, \cos(cA_k(T + \phi_k)) + P\, f_1. \tag{5.16}$$

5.3 Study of the map

Figure 5.2 shows the underlying displacement and velocity evolution through three evaluations of the map. We start with a random initial condition (A_0, ϕ_0) for the map. $x(t)$ and $\dot{x}(t)$ evolve in the time interval $[0, 1]$ according to Eqs. (5.9) and (5.10) with $k = 0$. At $t = 1$, we get a new state (A_1, ϕ_1) as per Eqs. (5.13) and (5.14). In the interval $[1, 2]$, $x(t)$ and $\dot{x}(t)$ evolve according to Eqs. (5.9) and (5.10) again, but now with $k = 1$. At $t = 2$ we get a new state (A_2, ϕ_2) and the system evolves forward in time in this manner. Numerical values of $\dot{x}(t)$ at the points of discontinuity are indicated in the figure.

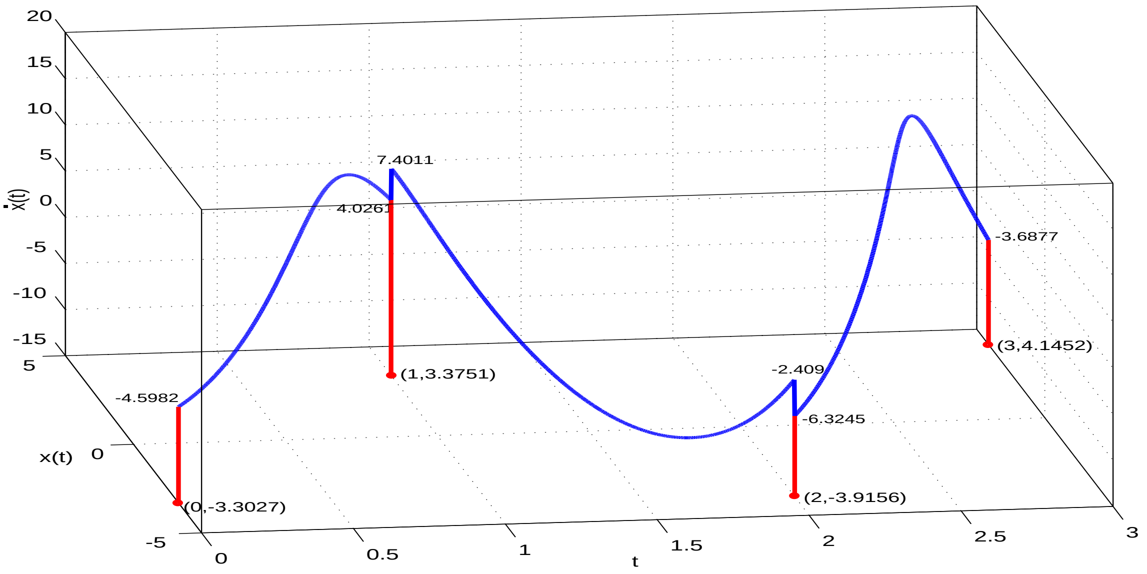

Figure 5.2: Time evolution of $x(t)$ and $\dot{x}(t)$ governed by the map for $T = 1$, $P = 1$. The red lines are drawn for visualization only.

Figure 5.3 shows displacement and velocity evolution for several iterates of the map for another initial condition. We observe that $x(t)$ is continuous and there are finite jumps in $\dot{x}(t)$ at times $t = kT$.

Figure 5.4 shows a numerically generated Poincaré plot (A-ϕ plane) of the map for many trajectories obtained using different initial conditions. We see different-period island chains, as also seen in [44]. In generating these and subsequent numerical results, we have used MATLAB's 'atan2' function in Eq. (5.14). This function has range $[-\pi, \pi]$. As can be seen from the figure, the region of the A-ϕ plane that different states can take is bounded by the curves $\phi = -\pi/cA$ and π/cA with $c = \dfrac{\sqrt{3}}{2}$. These two boundary curves can be thought of as identical.

We now seek the fixed points of the map using the Newton-Raphson method. We evaluate the Jacobian matrices (numerically, for simplicity) for the fixed points and compute their eigenvalues with MATLAB's 'eig' function to determine the stability at the same time. Eigenvalues with magnitude greater than 1 indicate instability. Numerically obtained fixed

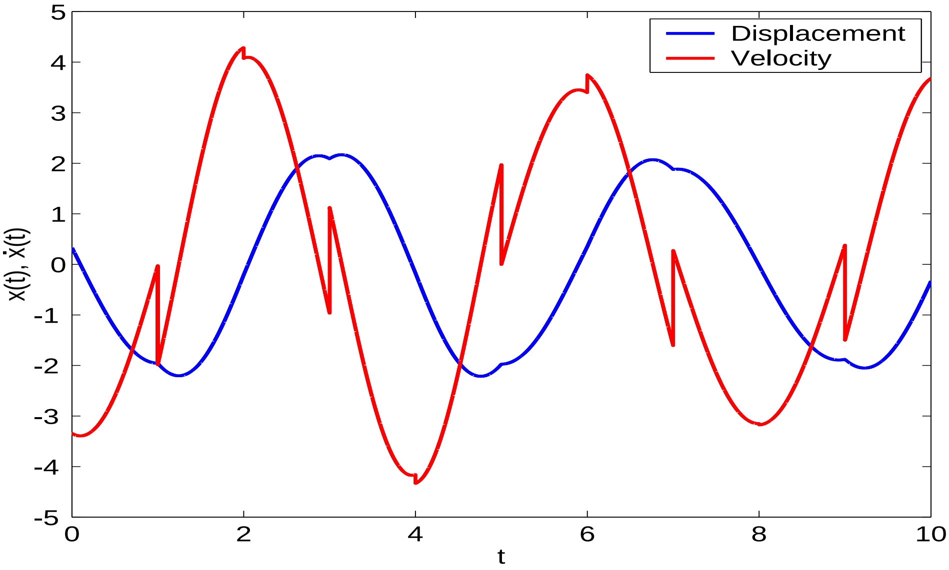

Figure 5.3: Time evolution of $x(t)$ and $\dot{x}(t)$ for several iterates of the map with $T = 1$, $P = 1$.

points of the map are shown in Fig. 5.5 using blue circles.

The analytically obtained fixed points (shown in red stars, and occurring on the curve of discontinuity $\phi = \pm\pi/cA$) are discussed next. For a point (A^*, ϕ^*) to be a fixed point, the following conditions need to be satisfied simultaneously:

$$A^* \sin(cA^*\phi^*) = A^* \sin(cA^*T)\cos(cA^*\phi^*) + A^* \cos(cA^*T)\sin(cA^*\phi^*) \tag{5.17}$$

and

$$c\,A^{*2} \cos(cA^*\phi^*) = c\,A^{*2} \cos(cA^*\,(T+\phi^*)) + P\,A^* \sin(cA^*\,(T+\phi^*)),$$

i.e.

$$cA^* \cos(cA^*\phi^*) = cA^* \cos(cA^*T) \cos(cA^*\phi^*) + \Big\{P - cA^* \sin(cA^*T)\Big\} \sin(cA^*\phi^*). \tag{5.18}$$

We must now consider a special case, with two subcases.

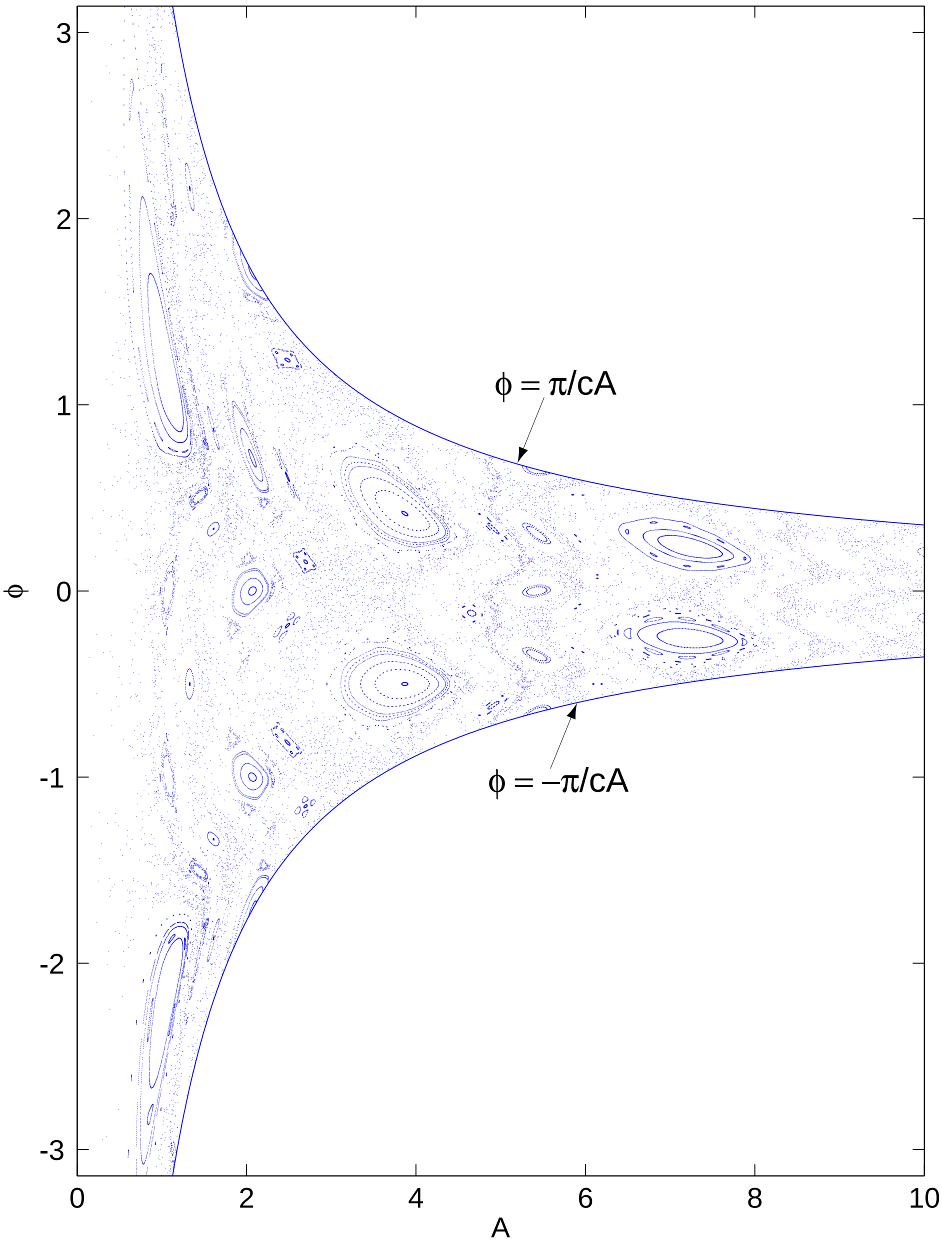

Figure 5.4: Numerically generated Poincaré plot for Eqs. (5.13) and (5.14) for several initial conditions with parameter values $T = 1$, $P = 1$.

5.3.1 The special case when $\sin(cA^*\phi^*) = 0$.

We must check analytically for solutions on the curve of discontinuity, where $\phi = \pm\pi/cA$, because the discontinuity makes numerical work difficult there. Accordingly, we assume

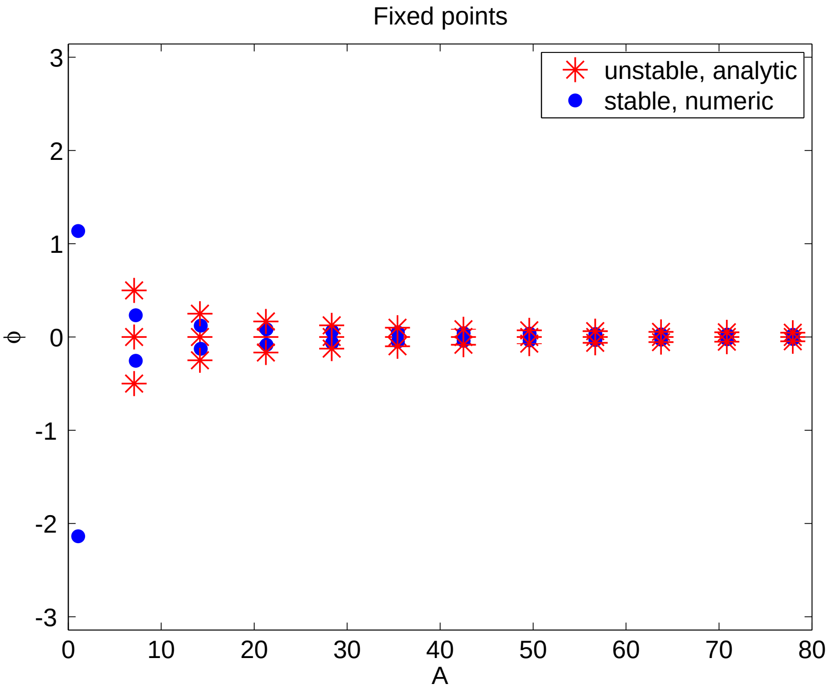

Figure 5.5: Numerically found and analytically determined fixed points of the map with $T = 1$, $P = 1$.

$\sin(cA^*\phi^*) = 0$. Then Eq. (5.18) becomes

$$\cos(cA^*T) = 1.$$

Therefore

$$A^* = \frac{2n\pi}{cT}$$

with $n = 0, 1, 2, 3 \cdots$. Eq. (5.17) becomes

$$A^* \sin(cA^*T)\cos(cA^*\phi^*) = 0.$$

As $\sin(cA^*\phi^*) = 0$, we must have $\cos(cA^*\phi^*) = \pm 1$. With $A^* = \dfrac{2n\pi}{cT}$, we get

$$\frac{2n\pi}{T}\phi^* = \arccos(\pm 1) = m\pi,$$

for $m = 0, 1, 2, 3 \cdots$. All even integers m correspond to $\cos(cA^*\phi^*) = 1$, in which case it turns out that it is sufficient to simply take $m = 0$ because taking $m = 2$ or greater gives a value of ϕ that lies outside its allowed range of $(-\pi/cA,\ \pi/cA)$. All odd integers m correspond to $\cos(cA^*\phi^*) = -1$, in which case it similarly turns out that it is sufficient to simply take $m = 1$. So we consider $m = 0$ and 1 only. Therefore, fixed points for the case $\sin(cA^*\phi^*) = 0$ are

$$A^* = \frac{2n\pi}{cT}, \qquad \text{with } \phi^* = 0 \quad \text{or} \quad \phi^* = \frac{T}{2n}.$$

These fixed points are depicted using red stars in Fig. 5.5. They happen to be unstable, as shown later. Even though in Fig. 5.5 we see fixed points with $\phi^* = T/2n$ and $\phi^* = -T/2n$, with the same A^*, as different pairs of stars, each pair represents just one fixed point.

Fixed points $\left(\dfrac{2n\pi}{cT}, 0\right)$

For fixed points $\left(\dfrac{2n\pi}{cT}, 0\right)$, the Jacobian matrix is

$$J = \begin{bmatrix} 1 + \dfrac{1}{2}PT & \dfrac{n\pi P}{cT} \\ \dfrac{1}{2}\dfrac{cT^2}{n\pi} & 1 \end{bmatrix} \tag{5.19}$$

with eigenvalues $(1 + \frac{PT}{4}) \pm \sqrt{\frac{P^2T^2}{16} + \frac{PT}{2}}$ for all n. For parameter values $T = 1,\ P = 1$, two eigenvalues are $(2,\ 0.5)$ indicating that the fixed points are unstable.

Fixed points $\left(\dfrac{2n\pi}{cT}, \dfrac{T}{2n}\right)$

The Jacobian matrix for fixed points $\left(\dfrac{2n\pi}{cT}, \dfrac{T}{2n}\right)$ is

$$J = \begin{bmatrix} 1 + \left(\dfrac{1}{2} + \dfrac{1}{4n}\right)PT & \dfrac{n\pi P}{cT} \\ \left(\dfrac{1}{2} + \dfrac{1}{4n}\right)\dfrac{cT^2}{n\pi} & 1 \end{bmatrix} \tag{5.20}$$

with eigenvalues $1 + (\frac{1}{2} + \frac{1}{4n})\frac{PT}{2} \pm \sqrt{(\frac{1}{2} + \frac{1}{4n})^2\frac{P^2T^2}{4} + (\frac{1}{2} + \frac{1}{4n})PT}$. For $P > 0$ and any positive finite value of n one eigenvalue is less than 0.5 and the other is greater than 2; in the limit $n \to \infty$, we get 0.5 and 2. So these fixed points also are unstable. Red marks with $\phi \neq 0$ in Fig. 5.5 indicate these points.

Period	2	3
(A_0, ϕ_0)	(24.84613, 0.07025204)	(4.657493, -0.11973756)
(A_1, ϕ_1)	(24.84613, -0.07025204)	(4.916007, -0.6135473)
(A_2, ϕ_2)	(24.84613, 0.07025204)	(4.916007, 0.33407899)
(A_3, ϕ_3)		(4.657493, -0.11973756)

Table 5.1: Orbits with periods 2 and 3. These orbits are stable.

5.3.2 Physical interpretation

We now physically explain the analytically determined fixed points for $\sin(cA^*\phi^*) = 0$ case. We consider the pendulum as shown in Fig. 5.1. The case $\sin(cA^*\phi^*) = 0$ ($f_1 = 0$ in Eq. (5.16)) corresponds to $cA^*\,\phi^* = 0$ or π. For corresponding ϕ^* values, the displacement is zero at the instant of the impulse (i.e., $x_- = x_+ = 0$). The forcing has no effect and velocity is continuous. The pendulum completes an integral multiple of half-cycles in time T. If we consider a nearby initial condition to a fixed point $(A^*, 0)$, say a small non-zero positive phase value with the same amplitude A^*, the impulse will make the pendulum accelerate, thereby increasing its amplitude. Since the nonlinearity considered is a stiffening nonlinearity, this increase in amplitude will result in a decrease in the time period. So after time T, the phase will increase further and will thus continue to increase. This explains the instability of the fixed point.

There exist several higher period orbits of the map, which can be found numerically. Here we will list one example each of orbits with periods 2, 3, 4 and 5 (Tables 5.1 and 5.2).

Figures 5.6 and 5.7 show orbits with periods 1, 3, 4 and 5 of unstable type in the Poincaré plots and their stable and unstable manifolds computed from software gm1D [42]. As seen from the figures, stable and unstable manifolds intersect transversally which confirms the presence of chaos. Although we know unstable period-2 solutions exist (e.g., starting from $A_0 = 3.5421391$, $\phi_0 = 0$, $A_1 = 3.5421391$, $\phi_1 = -1$), for some reason we do not understand, we were unable to obtain similar plots of stable and unstable manifolds of these fixed points using this software.

Period	4	5
(A_0, ϕ_0)	(72.62261, 0.0242668)	(1.2730136, 0.8912417)
(A_1, ϕ_1)	(72.62261, 0.0487746)	(1.1189589, 1.3010092)
(A_2, ϕ_2)	(72.62261, -0.0245078)	(0.8610816, 1.81581637)
(A_3, ϕ_3)	(72.62261, 0)	(0.861081605, 1.297776525)
(A_4, ϕ_4)	(72.62261, 0.0242668)	(1.1189589, 0.86455756)
(A_5, ϕ_5)		(1.2730136, 0.8912417)

Table 5.2: Orbits with periods 4 and 5. These orbits are stable.

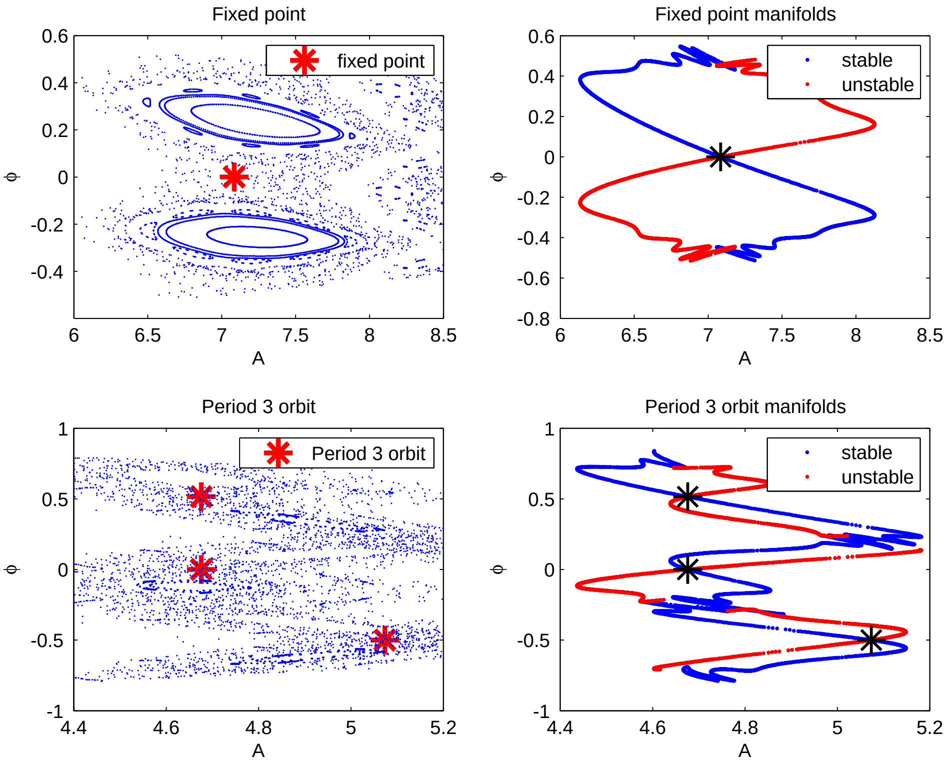

Figure 5.6: Fixed point and period 3 orbit in the Poincaré plot and their invariant manifolds.

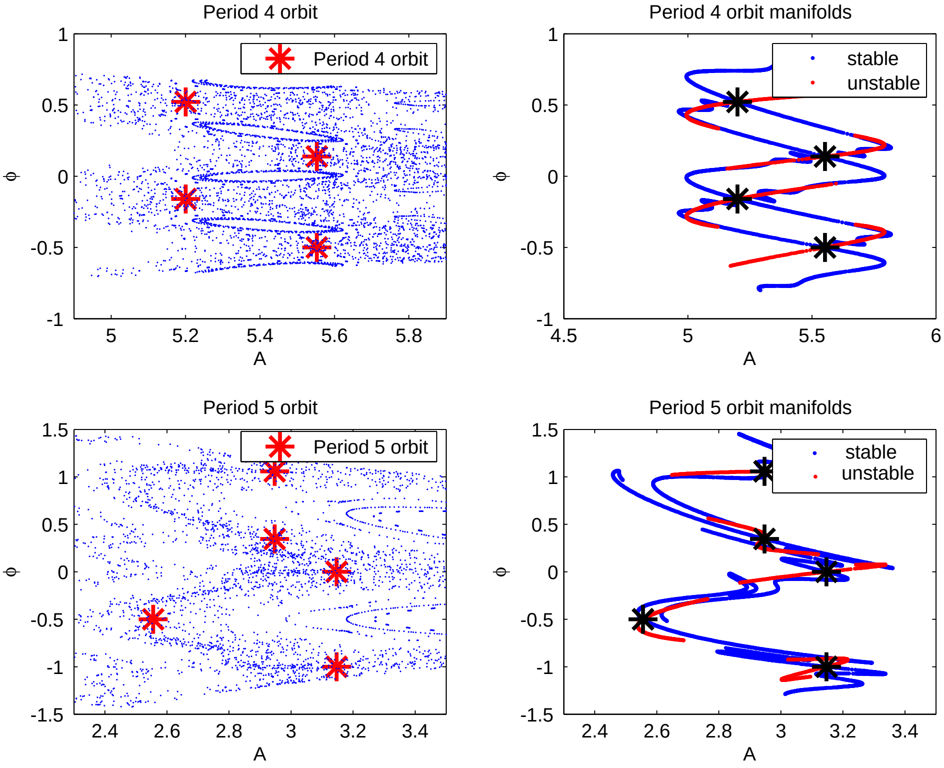

Figure 5.7: Period 4 and period 5 orbits in the Poincaré plot and their invariant manifolds.

We carry out a brief numerical investigation for one more parameter value, $P = 0.1$. Figure 5.8 shows the Poincaré plot. No chaotic trajectories are apparent. The system seems to be non-chaotic for small values of the parameter P.

5.4 Concluding remarks

Using a 1-term harmonic balance approximation for the solution of a strongly nonlinear oscillator, we have constructed an explicit map. We have numerically found fixed points of the map and studied their stability. We have also obtained some fixed points analytically. With the help of a free downloadable software, we have computed invariant manifolds of unstable orbits of the map. The stable and unstable manifolds intersect in a transverse

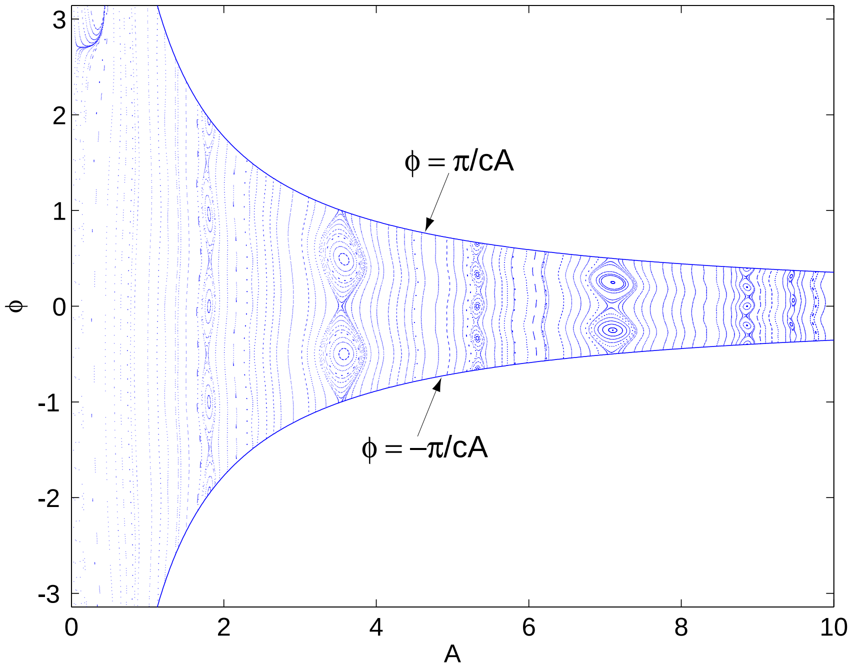

Figure 5.8: Numerically generated Poincaré plot for the map with $T = 1$, $P = 0.1$.

manner indicating the presence of chaos. The system seems to be not chaotic for small values of the parameter P.

Chapter 6

Conclusions

We have studied four nonlinear systems with parametric forcing.

In chapter 2, we numerically and theoretically studied asymmetric Mathieu equations, which are strongly nonlinear, conservative, and have scaleable solutions. We have found that there are infinitely many instabilities for this system that are missing for the usual Mathieu equation. There are periodic solutions on every stability boundary in the parameter space with periods not only 2π or 4π but with periods that are higher multiples of 2π. Theoretical results obtained are also applicable to asymmetric Hill's equation. The work in this chapter has been published in [6].

In chapter 3, we have tried to understand the dynamics associated with early and delayed ejection of ions in practical Paul traps operated in the mass selective ejection mode. The equation of motion of ions in the axial direction of the trap was studied using the method of multiple scales. The ordering scheme used allowed a systematic inclusion of higher order multipoles. Although a fourth order slow flow equation has been computed and reported for potential future use in traps with larger weights of multipole superpositions, in the present study the second order slow flow was used for generating phase portraits. Phase portraits generated by numerical integration of the slow flow have been used to predict the qualitative behavior of ion motion near the stability boundary in the presence of nonlinearities. The work in this chapter was done in collaboration with Rajanbabu, and has been published in [8].

In chapter 4, we studied harmonic wave attenuation in periodic structures with linear and weakly nonlinear damping. The problem was studied using maps which were slightly perturbed versions of simpler maps having a pair of purely imaginary eigenvalues. The maps were analyzed using the method of multiple scales. Good agreement between the MMS approximation and full numerics was observed in the nonlinear case, when the number of periods of the structure was $\mathcal{O}(1/\epsilon)$. For the linear damping case, agreement was good for larger number of periods. The attenuation constant can be estimated analytically in the case of linear damping and was in excellent agreement with that obtained by the MMS. The work in this chapter has been published in [10].

In chapter 5, we have studied a periodically kicked oscillator with a strong nonlinearity. We constructed an explicit map assuming a 1-term harmonic balance approximation for the solution of the strongly nonlinear oscillator in between successive kicks. We obtained fixed points numerically and analytically. With the help of a free downloadable software, we computed invariant manifolds of periodic orbits of the unstable type. Transverse intersections of the stable and unstable manifolds confirmed the presence of chaos for a chosen parameter value.

Appendix A

An arc-length based continuation method

We numerically seek periodic solutions to Eq. (2.1). Consider a solution starting at $t = 0$. If x_0 and $\dot{x}_0$ are the initial conditions and we numerically integrate Eq. (2.1) to $t = T$ for suitable T, then $x(T)$ and $\dot{x}(T)$ should satisfy

$$x(T) - x_0 = 0, \tag{A.1}$$

$$\dot{x}(T) - \dot{x}_0 = 0. \tag{A.2}$$

The routine continuation method described below was also used in [48]. Assume that we are on a branch where we can take $x_0 = 1$ (recall that solutions are scaleable; the corresponding procedure for $x_0 = -1$ or $\dot{x}_0 = \pm 1$ will be obvious below). We define

$$y = \left\{ \begin{array}{c} \dot{x}_0 \\ \epsilon \\ \delta \end{array} \right\}. \tag{A.3}$$

Assume that for some known y, i.e., for some known choice of δ, ϵ as well as $\dot{x}_0$, we have a periodic solution of period T. [Such a y can be found by an initial numerical search that is simpler than the continuation method and is not described here. Note, in particular, that resonance conditions provide the δ values corresponding to $\epsilon = 0$, so only $\dot{x}_0$ need to be found for these points.] Let us refer to this value of y by the name y_{old}. The continuation method is based on defining a function $g(y_{new})$ as follows.

Given any vector y_{new}, we have δ_{new}, ϵ_{new} and $\dot{x}_{0,new}$. Inserting δ_{new} and ϵ_{new} into Eq. (2.1), and using initial conditions $x_0 = 1$ and $\dot{x}_0 = \dot{x}_{0,new}$, we numerically integrate forward to time T to obtain $x(T)$ and $\dot{x}(T)$. We also choose a small positive number s, which represents arc-length. Then we define

$$g(y_{new}) = \left\{ \begin{array}{l} x(T) - 1 \\ \dot{x}(T) - \dot{x}_{0,new} \\ \|y_{old} - y_{new}\| - s \end{array} \right\}. \tag{A.4}$$

We now numerically evaluate the function g as accurately as we like; and use any standard iterative technique (like Newton-Raphson) to find a value y_{new} that satisfies $g(y_{new}) = 0$. Finally, we redefine y_{old} to be the freshly obtained y_{new}, and repeat the above procedure. This completes the arc-length based continuation method.

In numerical implementation, in the Newton-Raphson iterative stage, it is helpful to have a good initial guess. Using the two previously obtained y vectors, say y_1 and y_2, to extrapolate linearly to

$$y_{guess} = 2y_2 - y_1$$

gives a good guess for small s in most cases.

Appendix B

Fourth order MMS slow flow

The slow flow equation after carrying out the fourth order multiple scales analysis will be in the form

$$\begin{aligned}
\ddot{A} \;=\;& \epsilon\,(-12.8564\,\bar{h}\,\bar{d}A^5 - 9.44304\,\bar{d}^2A^7 - 3.88769\,\bar{h}^2A^3 + 0.97124\,\bar{k}\,A^5 \\
&+0.87729\,\Delta\,A + 0.88965\,\bar{f}\,A^3 + 39.31546\,\bar{h}^2\dot{A}^2A - 5.50581\,\bar{f}\,\dot{A}^2A \\
&+657.373\,\bar{d}^2\dot{A}^2A^5 - 20.2091\,\bar{k}\,\dot{A}^2A^3 + 411.774\,\bar{h}\bar{d}\,\dot{A}^2\,A^3) \\
&+\epsilon^2\,(-0.18369\,\Delta^2A - 125.986\,\bar{h}^4A^5 - 1892.91\,\bar{d}^4A^{13} + 290.186\,\bar{h}\,\bar{f}\,\bar{d}A^7 \\
&+493.157\,\bar{h}\,\bar{d}\bar{k}\,A^9 + 389.577\,\bar{d}^2\bar{k}A^{11} - 1176.36\,\bar{h}^3\bar{d}A^7 - 3572.55\,\bar{h}^2\bar{d}^2A^9 \\
&+151.374\,\bar{h}^2\bar{k}A^7 - 7.64328\,\bar{d}\bar{k}\,A^7 + 23.3241\,\Delta\bar{h}^2A^3 + 78.6875\,\bar{h}^2\bar{d}A^5 \\
&+251.73\,\bar{f}\,\bar{d}^2A^9 + 133.2125\,\Delta\,\bar{d}^2A^7 - 1.76775\,\Delta\,\bar{d}A^3 - 4394.78\,\bar{h}\,\bar{d}^3A^{11} \\
&-3.843405\,\Delta\bar{k}\,A^5 + 121.976\,\Delta\,\bar{h}\,\bar{d}A^5 - 2.60912\,\bar{d}^2A^5 - 5.22277\,\bar{k}^2A^9) \qquad \text{(B.1)}
\end{aligned}$$

Appendix C

Choice of time scales in MMS

Time scales chosen in the MMS when applied to Eq. (3.9) are $T_0 = \tau$, $T_1 = \sqrt{\epsilon}\,\tau$, $T_2 = \epsilon\tau$, $\cdots$. Our choice is based on the following.

We consider

$$\frac{d^2x}{d\tau^2} + 2(q_z^* + \epsilon\Delta)\,\cos(2\tau)(x + \epsilon\,x^3) = 0, \tag{C.1}$$

which can be rewritten as

$$\frac{d^2x}{d\tau^2} + 2q_z^*\cos(2\tau)\,x + 2\epsilon\,\cos(2\tau)(q_z^*\,x^3 + \Delta x) + \mathcal{O}(\epsilon^2) = 0. \tag{C.2}$$

We numerically integrate Eq. (C.2), neglecting $\mathcal{O}(\epsilon^2)$ terms, with initial conditions $x(0) = 0.01$ and $\dot{x}(0) = 0$ for a fixed value of $\epsilon = 0.001$. We observe the period of the slowly varying amplitude to be $T = 433.25$ (Fig. 10(a)). With the same initial conditions, we integrate Eq. (C.2) again, but now for $\epsilon = 0.002$. This time period of the solution is observed to be $T = 306.35$. Note that $433.25/306.35 \approx 1.414.. \approx \sqrt{2}$. The solution for $\epsilon = 0.002$ is therefore plotted against $\sqrt{2}\,\tau$ instead of τ and we get approximately the same period i.e. $T \approx 433.25$ (Fig. 10(b)). This observation suggests that the $\sqrt{\epsilon}\,\tau$ time scale is present in the solution. We support our observation further using an analogy. The unperturbed equation in case of Eq. (3.9) is

$$\frac{d^2x}{d\tau^2} + 2\,q_z^*\cos(2\tau)\,x = 0. \tag{C.3}$$

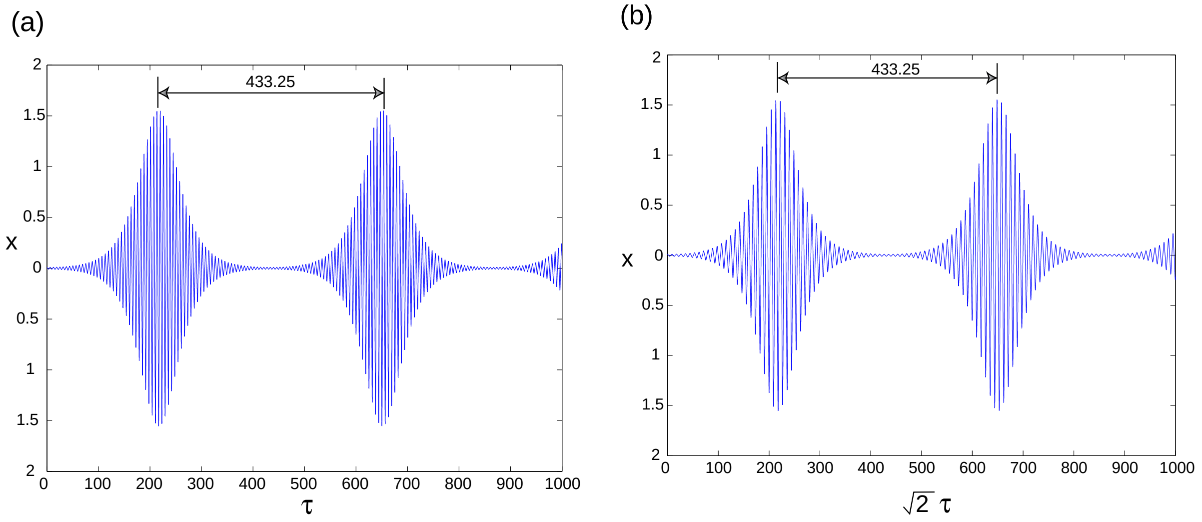

Figure C.1: Time period of the amplitude for (a) $\epsilon = 0.001$ and (b) $\epsilon = 0.002$.

This equation is a linear Mathieu equation with q_z^* value corresponding to q at the stability boundary. Eq. (C.3) has two linearly independent solutions, one periodic with constant amplitude and the other with amplitude growing linearly with time.

Now consider

$$\frac{d^2x}{d\tau^2} = 0. \tag{C.4}$$

It is a second order, linear homogeneous ordinary differential equation. It has two linearly independent solutions, one constant and the other linearly growing with respect to time, similar at an abstract level to the behavior of the amplitude for the linear Mathieu equation. If we perturb Eq. (C.4) as

$$\frac{d^2x}{d\tau^2} + \epsilon x = 0, \tag{C.5}$$

the solution becomes

$$x = A\cos(\sqrt{\epsilon}\,\tau) + B\sin(\sqrt{\epsilon}\,\tau), \tag{C.6}$$

where A and B depend upon the initial conditions. We see that time scale $\sqrt{\epsilon}\,\tau$ is present in the solution.

Equation (3.9) is a perturbation to Eq. (C.3). So we expect time scales τ, $\sqrt{\epsilon}\tau$, $\epsilon\tau$, $\cdots$ to be present in the solution. The final MMS approximation, of course, is amply supported by full numerical checks.

Appendix D

Expressions for X_1 and X_2

The solution for X_1 (not displaying the coefficients which are less than 10^{-5}) is

$$\begin{aligned} X_1 \approx\; & -1.13522\,\frac{\partial A}{\partial T_1}\sin(T_0) - 0.18287\,\frac{\partial A}{\partial T_1}\sin(3\,T_0) - 0.00812\,\frac{\partial A}{\partial T_1}\sin(5\,T_0) \\ & -0.00017\,\frac{\partial A}{\partial T_1}\sin(7\,T_0) - 0.60164\,\bar{h}\,A^2\cos(2\,T_0) - 0.6719\,\bar{d}\,A^4\cos(2\,T_0) \\ & +0.00066\,\bar{h}\,A^2\cos(4\,T_0) + 0.00455\,\bar{d}\,A^4\cos(4\,T_0) + 0.00268\,\bar{h}\,A^2\cos(6\,T_0) \\ & +0.0078\,\bar{d}\,A^4\cos(6\,T_0) + 0.00016,\bar{h}\,A^2\cos(8\,T_0) + 0.00116\,\bar{d}\,A^4\cos(8\,T_0) \\ & +0.00011\,\bar{d}A^4\cos(10\,T_0) - 2.07004\,\bar{d}A^4 - 1.88307\,\bar{h}A^2 \end{aligned} \tag{D.1}$$

The solution for X_2 (not displaying the coefficients which are less than 10^{-5}) is

$$
\begin{aligned}
X_2 \approx\ & 1.1332\,\bar{h}\,A\frac{\partial A}{\partial T_1}\sin(2\,T_0) + 2.46062\,\bar{d}\,A^3\frac{\partial A}{\partial T_1}\sin(2\,T_0) - 0.00693\,\bar{h}\,A\frac{\partial A}{\partial T_1}\sin(4\,T_0) \\
& +0.03699\,\bar{d}\,A^3\frac{\partial A}{\partial T_1}\sin(4\,T_0) - 0.00963\,\bar{h}\,A\frac{\partial A}{\partial T_1}\sin(6\,T_0) - 0.03737\,\bar{d}\,A^3\frac{\partial A}{\partial T_1}\sin(6\,T_0) \\
& -0.00066\,\bar{h}\,A\frac{\partial A}{\partial T_1}\sin(8\,T_0) - 0.00662\,\bar{d}\,A^3\frac{\partial A}{\partial T_1}\sin(8\,T_0) - 0.00002\,\bar{h}\,A\frac{\partial A}{\partial T_1}\sin(10\,T_0) \\
& -0.00073\,\bar{d}\,A^3\frac{\partial A}{\partial T_1}\sin(10T_0) - 0.00006\,\bar{d}\,A^3\frac{\partial A}{\partial T_1}\sin(12\,T_0) \\
& +0.14628\,\Delta\,A\,\cos(3T_0) - 0.02631\,\bar{h}^2\,A^3\,\cos(3T_0) - 0.00325\,\bar{f}\,A^3\,\cos(3T_0) \\
& -0.00009\,\bar{f}\,A^5\,\cos(3T_0) - 0.00195\,\bar{h}\,\bar{d}\,A^5\,\cos(3T_0) + 0.02946\,\bar{d}^2\,A^7\,\cos(3T_0) \\
& +0.00187\,\Delta\,A\,\cos(5T_0) - 0.02469\,\bar{h}^2\,A^3\,\cos(5T_0) + 0.01234\,\bar{f}\,A^3\,\cos(5T_0) \\
& -0.15887\,\bar{h}\,\bar{d}\,A^5\,\cos(5T_0) + 0.01857\,\bar{f}\,A^5\,\cos(5T_0) - 0.1447\,\bar{d}^2\,A^7\,\cos(5T_0) \\
& +0.00007\,\Delta\,A\,\cos(7T_0) - 0.00159\,\bar{h}^2\,A^3\,\cos(7T_0) + 0.00186\,\bar{f}\,A^3\,\cos(7T_0) \\
& -0.02564\,\bar{h}\,\bar{d}\,A^5\,\cos(7T_0) + 0.00456\,\bar{f}\,A^5\,\cos(7T_0) - 0.02621, \bar{d}^2\,A^7\,\cos(7T_0) \\
& -0.00001\,\bar{h}^2\,A^3\,\cos(9T_0) + 0.00015\,\bar{f}\,A^3\,\cos(9T_0) - 0.00231\,\bar{h}\,\bar{d}\,A^5\,\cos(9T_0) \\
& -0.000728\,\bar{f}\,A^5\,\cos(9T_0) - 0.00246\,\bar{d}^2\,A^7\,\cos(9T_0) - 0.00013\,\bar{h}\,\bar{d}\,A^5\,\cos(11T_0) \\
& +0.00009\,\bar{f}\,A^5\,\cos(11T_0) - 0.00011\,\bar{d}^2\,A^7\,\cos(11T_0)
\end{aligned}
\tag{D.2}
$$

X_1 and X_2 are provided here with numerical coefficients of their terms truncated to 5 decimal places. In our calculations using MAPLE, more digits were retained.

Appendix E

Comparison of second order slow flow with beat envelope equation

We reproduce Sudakov's equation of ion motion (Eq. (9) in [21]) below,

$$\frac{d^2u}{d\xi^2} + 2q_0\cos(2\xi)u = 2\,(q_0 - q)\cos(2\xi)\,u - q\cos(2\xi)\,4\,\alpha_4\,u^3, \tag{E.1}$$

where $u = \dfrac{z}{z_0}$, $\xi = \dfrac{\Omega\,t}{2}$ (= τ, in our study), $q_0 = q_z^*$ (in our study), $\alpha_4 = f\,\dfrac{z_0^2}{r_0^2}$ (= $\epsilon\dfrac{\bar{f}}{2}\,\dfrac{z_0^2}{r_0^2}$, in our study). The solution to Eq. (E.1) is assumed to be of the form (Eq. (A1) in Sudakov [21])

$$\begin{aligned} u(\xi) &= \epsilon Z\,u_1(\xi) + \epsilon^2\Bigg(h_1\sin(\xi) + h_3\sin(3\xi) + \cdots\Bigg) + \\ &\quad \epsilon^3\Bigg(g_3\cos(3\xi) + g_5\cos(5\xi) + \cdots\Bigg), \end{aligned} \tag{E.2}$$

where Z is the beat envelope (our "amplitude") and u_1 is the periodic solution of the linear Mathieu equation at the stability boundary and h_k's and g_k's are slowly varying amplitudes of the harmonics.

The beat envelope equation has been found by Sudakov [21] to be

$$\frac{d^2Z}{d\xi^2} + 0.8873\,(q_0 - q)Z - 1.4572\,\alpha_4 Z^3 = 0. \tag{E.3}$$

However, the slow flow equation (Eq. (3.34)) derived by us, when there is only octopole nonlinearity, has the form

$$\ddot{A} = \epsilon\,(0.8773\,\Delta A + 0.8897\,\bar{f} A^3). \tag{E.4}$$

We must now transform our equation, Eq. (E.4), to the form presented by Sudakov [21]. This will require transforming different parameters in our equation to conform to Eq. (E.3). This is described below.

We nondimensionalized the axial position variable z as $x = \dfrac{z}{r_0}$; since $u = \dfrac{z}{z_0}$, we have $x = \dfrac{z_0}{r_0}u$. Since $x = X_0 + \mathcal{O}(\sqrt{\epsilon}) = A\,\xi_1 + \mathcal{O}(\sqrt{\epsilon})$, we write $x \approx A\,\xi_1$ i.e., $\dfrac{z_0}{r_0}u \approx A\,\xi_1$. Sudakov shows in Appendix A of [21] that his h_k's and g_k's are of the first and second orders, respectively. Since ϵ is a book-keeping parameter in that study (the correspondence between Sudakov's ϵ and ours is therefore not direct, and is avoided in this discussion), we can write $u \approx Z\,u_1$, and therefore $A \approx \left(\dfrac{z_0}{r_0}\right)\left(\dfrac{u_1}{\xi_1}\right)Z$. Finally, substituting $\bar{f} = \dfrac{2}{\epsilon}\dfrac{r_0^2}{z_0^2}\alpha_4$, $\Delta = -\dfrac{q_0 - q}{\epsilon}$ and $A \approx \dfrac{z_0}{r_0}\dfrac{u_1}{\xi_1}Z$ into Eq. (E.4), we obtain

$$\frac{d^2 Z}{d\xi^2} + 0.8873\,(q_0 - q)\,Z - 1.7794\left(\frac{u_1}{\xi_1}\right)^2 \alpha_4\,Z^3 = 0. \tag{E.5}$$

From Eq. (10) of Sudakov [21], it can be seen that u_1 is scaled such that all coefficients in the solution add to 1. In our study, we have not imposed this condition on ξ_1 and we have obtained, instead, $u_1/\xi_1 = 0.90495$. Substituting this, Eq. (E.5) then becomes

$$\frac{d^2 Z}{d\xi^2} + 0.8873\,(q_0 - q)\,Z - 1.4572\alpha_4\,Z^3 = 0 \tag{E.6}$$

Comparing Eq. (E.3) and Eq. (E.6) indicates that, for octopole superposition, the beat envelope equation and the slow flow are identical.

We next investigate the two equations (ours, and Sudakov's) for the case of hexapole superposition. Eq. (B7) in Sudakov [21] which represents the beat envelope for hexapole superposition is

$$\frac{d^2 Z}{d\xi^2} + 0.8873\,(q_0 - q)Z + 12.692\,\alpha_3^2 Z^3 = 0. \tag{E.7}$$

Following the procedure adopted for octopole nonlinearity and substituting $\bar{h} = \dfrac{3}{2\sqrt{\epsilon}}\left(\dfrac{r_0}{z_0}\right)$ in the slow flow, Eq. (3.34) with only hexapole superposition can be transformed to

$$\frac{d^2 Z}{d\xi^2} + 0.8873\,(q_0 - q)\,Z + 7.1693\alpha_3^2\,Z^3 = 0. \tag{E.8}$$

It is observed that the coefficient of $\alpha_3^2\, Z^3$ in Eqs. (E.7) and (E.8) differ significantly. We now verify the correctness of the coefficients by comparing the solutions of the two equations with the solution of the original equation (Eq. (B1)) in Sudakov [21] with hexapole superposition, which is

$$\frac{d^2u}{d\xi^2} + 2q\cos(2\xi)u = -q\cos(2\xi)\,3\,\alpha_3\,u^2. \tag{E.9}$$

These equations are integrated using the ODE45 routine of MATLAB with tolerance values of 10^{-10}. The amplitude obtained from the transformed slow flow (Eq. (E.8)), shown as a heavy line in Fig. E.1, follows the solution of Eq. (E.1) very closely, while the amplitude from the beat envelope equation of Sudakov [21], Eq. (E.7), shown as a dash line in Fig. E.1, shows an error in the numerical term reported in Sudakov [21].

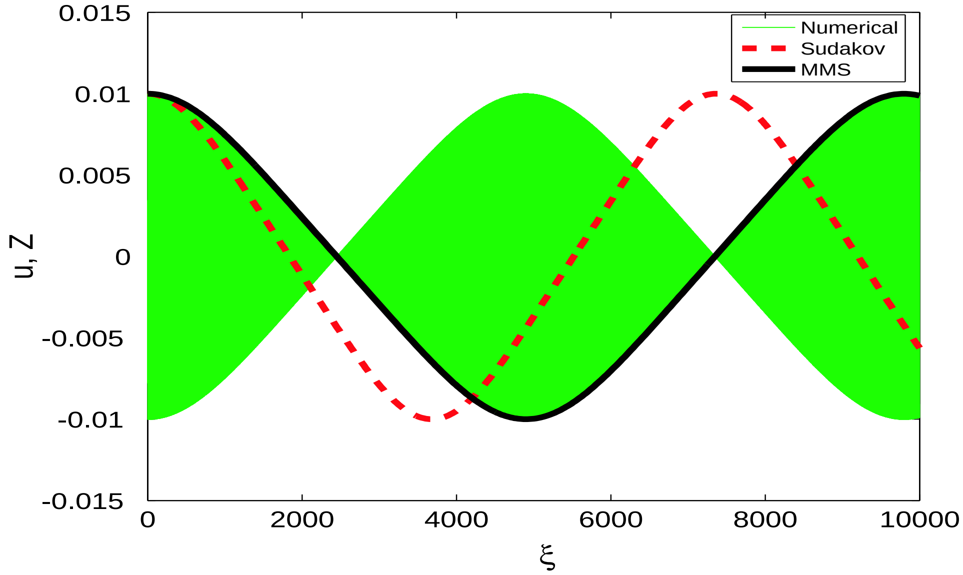

Figure E.1: Comparison between amplitude obtained by (Eq. (E.8)) and Eq. (E.7) for $\alpha_3 = 0.02828$ (4% hexapole), $q = q_0 = 0.908046$, $u(0) = 0.01, \dot{u}(0) = 0, Z(0) = 0.01, \dot{Z}(0) = 0$.

Appendix F

Initial condition calculation

We assume $X(0) = X_0(0)$. Since $X_0 = A(T_1)\,\xi_1(T_0)$, we have

$$X_0(0) = A(T_1)\,\xi_1(0).$$

From the expression for X_0 obtained from MAPLE, we have $\xi_1(0) = 1.105$. Therefore, the initial condition for A is

$$A(0) = \frac{X_0(0)}{1.105} + \mathcal{O}(\sqrt{\epsilon}) = \frac{X(0)}{1.105} + \mathcal{O}(\sqrt{\epsilon}).$$

We also have

$$\begin{aligned} \dot{X}(0) &= \dot{X}_0(0) + \sqrt{\epsilon}\,\dot{X}_1(0) + \mathcal{O}(\epsilon) \\ &= \xi_1(0)\,\dot{A}(0) + \sqrt{\epsilon}\,\frac{\partial X_1}{\partial T_0} + \mathcal{O}(\epsilon). \end{aligned} \tag{F.1}$$

From our solution (MAPLE), we have

$$\frac{\partial X_1}{\partial T_0} = -1.7244 \frac{\partial A}{\partial T_1}.$$

Substituting the above in Eq. (3.34), we get

$$\dot{A}(0) = \frac{\dot{X}(0)}{-0.6193} + \mathcal{O}(\epsilon).$$

Note that some small errors remain for nonzero ϵ, in light of which some small adjustments in initial conditions are allowed to obtain better fits.

References

[1] Hill, G. W., 1886, “On the part of the motion of the lunar perigee is a function of the mean motions of the Sun and the Moon”, *Acta Mathematica*, **8**, pp. 1-36.

[2] Ince, E. L., 1926, “The real zeros of solutions of a linear differential equation with periodic coefficients”, *Proceedings of the London Mathematical Society*, **2 25**, pp. 53-58.

[3] McLachen, N. W., 1947, *Theory and application of Mathieu functions*, Clarendon Press, Oxford.

[4] Stoker, J. J., 1950 *Nonlinear Vibrations in Mechanical and Electrical Systems*, John Wiley & sons, New York.

[5] Winkler, S., and Magnus, W., 1966, *Hill’s Equation*, Dover Publications, New York.

[6] Marathe, A., and Chatterjee, A., 2006 “Asymmetric Mathieu equations”, *Proceedings of the Royal Society A*, **462**, pp. 1643-1659.

[7] Rajanbabu, N., 2006, *Nonlinear dynamics of resonances in, and ejection from, Paul traps*, Ph.D. thesis, Department of Instrumentation, Indian Institute of Science, Bangalore, India.

[8] Rajanbabu, N., Marathe, A., Chatterjee, A., and Menon, A.G., 2006 “Multiple scales analysis of early and delayed boundary ejection in Paul traps”, *International Journal of Mass Spectrometry*, **261**, pp. 170-182.

[9] Chakraborty, G., and Mallik, A. K., 2001, “Dynamics of a weakly non-linear periodic chain”, *International Journal of Non-Linear Mechanics*, **36**, 375-389.

[10] Marathe, A., and Chatterjee A., 2006, "Wave attenuation in nonlinear periodic structures using harmonic balance and multiple scales", *Journal of Sound and Vibration*, **289**, pp. 871-888.

[11] Rand, R. H., 2003, *Lecture notes on nonlinear vibrations* version 45. Available online at http://www.tam.cornell.edu/randdocs/.

[12] Theodossiades, S., and Natsiavas, S., 2000, "Nonlinear dynamics of gear pair systems with periodic stiffness and backlash", *Journal of Sound and Vibration*, **229**(2), pp. 287-310.

[13] Rudin, W., 1976, *Principles of Mathematical Analysis*, McGraw-Hill, Singapore.

[14] Dawson, P.H., 1976, *Quadrupole Mass Spectrometry and its Application*, Elsevier, Amsterdam.

[15] March, R.E., and Hughes, R.J., 1989, *Quadrupole Storage Mass Spectrometry*, Wiley-Interscience Publications, New York.

[16] Stafford, G.C., Kelley, P.E., Syka, J.E.P., Reynolds, W.E., and Todd, J.F.J., 1984, "Recent improvements in and analytical applications of advanced ion trap technology", *International Journal of Mass Spectrometry and Ion Processes*, **60**, pp. 85-98.

[17] Wang, Y., and Franzen, J., 1994 "The non-linear ion trap: Part 3. Multipole components in three types of practical ion traps", *International Journal of Mass Spectrometry and Ion Processes*, **132**, pp. 155-172.

[18] Franzen, J., 1993, "The non-linear ion trap. Part 4. Mass selective instability scan with multipole superposition", *International Journal of Mass Spectrometry and Ion Processes*, **125**, pp. 165-170.

[19] Wang, Y., Franzen, J., and Wanczek, K. P., 1993, "The non-linear resonance ion trap: Part 2. A general theoretical analysis", *International Journal of Mass Spectrometry and Ion Processes*, **124**, pp. 125-144.

[20] Franzen, J., 1994, "The non-linear ion trap: Part 5. Nature of non-linear resonances and resonant ion ejection", *International Journal of Mass Spectrometry and Ion Processes*, **130**, pp. 15-40.

[21] Sudakov, M., 2001, "Effective potential and the ion axial beat motion near the boundary of the first stable region in a non-linear ion trap", *International Journal of Mass Spectrometry*, **206**, pp. 27-43.

[22] Abraham, G. T., and Chatterjee, A., 2003, "Approximate asymptotics for a nonlinear Mathieu equation using harmonic balance based averaging", *Nonlinear Dynamics*, **31**, pp. 347-365.

[23] Beaty, E. C., 1986, "Calculated electrostatic properties of ion traps", *Physical Review A*, **33**, pp. 3645-3656.

[24] Sevugarajan, S., and Menon, A. G., 2002, "Transition curves and iso-β_u lines in nonlinear Paul traps", *International Journal of Mass Spectrometry*, **218**, pp. 181-196.

[25] Abraham, G. T., Chatterjee, A., and Menon, A. G., 2004, "Escape velocity and resonant ion dynamics in Paul trap mass spectrometers", *International Journal of Mass Spectrometry*, **231**, pp. 1-16.

[26] March, R. E., and Londry, F. A., 1995, "Introduction to practical aspects of ion trap mass spectrometry", *Practical Aspects of Ion Trap Mass Spectrometry*, Chapter 2, Volume 1, CRC Press, New York.

[27] Nayfeh, A. H., 1973, *Perturbation Methods*, Wiley Interscience, New York.

[28] Holmes, M.H., 1991, *Introduction to Perturbation Methods*, Springer Verlag, New York.

[29] Hinch, E. J., 1991, *Perturbation Methods*, Cambridge University Press, UK.

[30] Kevorkian, J., and Cole, J. D., 1996, *Multiple Scale and Singular Perturbation Methods*, Applied Mathematical Sciences 114, Springer-Verlag, New York.

[31] Chatterjee, A., and Chatterjee, D., 2006, "Analytical investigation of hydrodynamic cavitation control by ultrasonics", *Nonlinear Dynamics*, **46**, pp. 179-194.

[32] Das, S. L., and Chatterjee, A., 2003, "Multiple scales via Galerkin projections: Approximate asymptotics for strongly nonlinear oscillations", *Nonlinear Dynamics*, **32**, pp. 161-186.

[33] Nandakumar, K., and Chatterjee, A., 2005 b "Higher-order pseudoaveraging via harmonic balance for strongly nonlinear oscillations", Transactions ASME *Journal of Vibration and Acoustics*, **127**, pp. 416-419.

[34] Mead, D. J., 1996, "Wave propagation in continuous periodic structures: Research contributions from Southampton, 1964-1995", *Journal of Sound and Vibration*, **190**(3), pp. 495-524.

[35] Yong, Y., and Lin, Y. K., 1989, "Propagation of decaying waves in periodic and piecewise periodic structures of finite length", *Journal of Sound and Vibration*, **129**(2), pp. 99-118.

[36] Langley, R. S., 1997, "The response of two-dimensional periodic structures to impulsive point loading", *Journal of Sound and Vibration*, **201**(2), pp. 235-253.

[37] Rebillard, E., Loyau, T., and Guyader, J. L., 1997 "Experimental study of periodic lattice of plates", *Journal of Sound and Vibration*, **204**(2), pp. 377-380.

[38] Benaroya, H., 1997, "Waves in periodic structures with imperfections", *Composites Part B* **28**, pp. 143-152.

[39] Wang, D., Zhou, C., and Rong, J., 2003, "Free and forced vibration of repetitive structures", *International Journal of Solids and Structures*, **40**, pp. 5477-5494.

[40] Hoppensteadt, F. C., and Miranker, W. L., 1977, "Multitime methods for systems of difference equations", *Studies In Applied Mathematics*, **56**, pp. 273-289.

[41] Subramanian, R., and Krishnan, A., 1979, "Nonlinear discrete time systems analysis by multiple time perturbation techniques", *Journal of Sound and Vibration*, **63**(3), pp. 325-335.

[42] Osinga, H., *Global Manifolds 1D* version 2. Available online at http://www.enm.bris.ac.uk/staff/hinke/dss/map/GM1D/index.html.

[43] Litchenberg, A. J., and Libermann, M. A., 1983, *Regular and Stochastic Motion*, Springer, Berlin.

[44] Rasband, S. N., 1990, *Chaotic Dynamics of Nonlinear Systems*, John Wiley & Sons.

[45] Moon, F. C., 1987, *Chaotic Vibrations: An Introduction for Applied Scientists and Engineers*, John Wiley & Sons, Canada.

[46] Pratap. R., Mukherjee, S., and Moon, F. C., 1994, “Dynamic behaviour of a bilinear hystertic elastoplastic oscillator, Part II: Oscillations under periodic impulse forcing”, *Journal of Sound and Vibration*, **172**(3), pp. 339-358.

[47] Pratap. R., Holmes P., 1995, “Chaos in a mapping describing elastoplastic oscillations”, *Nonlinear Dynamics*, **8**, pp. 111-139.

[48] Nandakumar, K., and Chatterjee, A., 2005, “Resonance, parameter estimation, and modal interactions in a strongly nonlinear benchtop oscillator.”, *Nonlinear Dynamics*, **40**, pp. 149-167.